#WaterMonographs

WATER MONOGRAPHS

Practical Flooding Risk Assessment for Development Projects

Alastair Barnett
James Ball
Fumihiko Imamura
Kwanchai Pakoksung
Anawat Suppasri

Supported by
HYDRA SOFTWARE LTD.
Hydraulic Engineering Solutions

IAHR AIRH
International Association for Hydro-Environment Engineering and Research
Hosted by Spain Water and IWHR, China

IAHR.org

Practical Flooding Risk Assessment for Development Projects

Alastair Barnett, James Ball, Fumihiko Imamura, Kwanchai Pakoksung and Anawat Suppasri

Practical Flooding Risk Assessment for Development Projects

Alastair Barnett
James Ball
Fumihiko Imamura
Kwanchai Pakoksung
Anawat Suppasri

IAHR WATER MONOGRAPH SERIES

Series Editor
Damien Violeau
LNHE, EDF R&D, France.
Saint-Venant Hydraulics Laboratory, Ecole des Ponts ParisTech, France.
E-mail: damien.violeau@edf.fr

ISBN (online version): 978-90-834302-2-5

ISBN (printed version): 978-90-834302-3-2

ISSN 2959-7978

doi: 10.3850/IAHR_Watermonograph_004

Published by:
IAHR — International Association for Hydro-Environment Engineering and Research

Madrid Office

Paseo Bajo Virgen del Puerto 3, 28005, Madrid, SPAIN
Tel: +34 913357908; Fax: +34 913357935

Beijing Office

A-1 Fuxing Road, Haidian District, 100038, Beijing, CHINA
Tel: +86 1068781128; Fax: +86 1068781890

The International Association for Hydro-Environment Engineering and Research (IAHR), founded in 1935, is a worldwide independent organisation of engineers and water specialists working in fields related to the hydro-environmental sciences and their practical application. Activities range from river and maritime hydraulics to water resources development and eco-hydraulics, through to ice engineering, hydro-informatics and continuing education and training. IAHR stimulates and promotes both research and it’s application, and by so doing strives to contribute to sustainable development, the optimisation of the world’s water resources management and industrial flow processes. IAHR accomplishes its goals by a wide variety of member activities including: working groups, research agenda, congresses, specialty conferences, workshops and short courses; Journals, Monographs and Proceedings; by involvement in international programmes such as UNESCO, WMO, IDNDR, GWP, ICSU, and by co-operation with other water-related (inter)national organisations.

The monitoring of publishing ethics is a major aspect of editorial and peer-review publications. IAHR is a well-established and long-standing organization whose primary mission is to foster knowledge exchange amongst its community and stakeholder base. Accordingly, IAHR takes its policies on ethics seriously.

The IAHR Water Monograph *Practical Flooding Risk Assessment for Development Projects* has been published under the IAHR Publications Ethics and Malpractice Statement. Additionally, IAHR publications follow the Ethical Guidelines and Codes of Conduct provided by the Committee of Publication Ethics (COPE).

Cover information: Cyclone Gabrielle Batters New Zealand
Credit: Kerry Marshall/ Getty Images News

Typeset by Research Publishing, Singapore. E-mail: enquiries@rpsonline.com.sg

About the IAHR Water Monograph Series

The Open Access Water Monograph Series joins IAHR's portfolio of publications, which includes journals, magazines, conference proceedings, whitepapers, and books. Since its start in 1935, IAHR has been dedicated to supporting the development and dissemination of knowledge that aids hydro-environment engineering and research.

The Water Monographs are mid-sized publications (about 50–150 pages long) that bridge knowledge gaps, summarize existing knowledge, and publicize recent advances in technologies and methods. More narrowly focused than a book, the Water Monographs occupy the publication space between a journal paper and a book. They concisely present information on physical processes, measurement techniques, theoretical material, numerical modeling techniques, engineering applications, and historical and cultural matters in an appealing readable and well-illustrated manner.

IAHR intends that the Water Monograph Series helps people understand specific longstanding, current, or emerging topics in hydro-environment engineering and research.

Damien Violeau
Chair of IAHR Water Monograph Series

Preface

In July 2021, extreme floods occurred all over the world within a single week. This coincidence covered both hemispheres, with catastrophic flooding in Germany and Belgium followed within just two days by torrential rainfall in Henan province in China, with the city of Zhengzhou receiving in *one day* close to its historical *annual* precipitation. Between these two events, unprecedented flood flow peaks were recorded in both the Buller and Wairau, two of the largest rivers in New Zealand.

Since only a global climate crisis can account for this remarkable simultaneous behaviour of weather systems which would previously have been regarded as unrelated, the IAHR immediately issued to the worldwide media a statement "Global floods 2021 – IAHR experts call for science-informed action!". The IAHR also added a special in-depth section "Extreme Flooding Events" to the next issue (2021 No.4) of their Hydrolink magazine, for which I was invited to serve as Guest Editor. Our Editorial there stated "According to the United Nations Office for Disaster Risk Reduction, the number of major floods in the period 2000–2019 has more than doubled compared to the previous twenty years (1980–1999)." Referring to the paper presented on the Belgian flooding, our Editorial further noted "This event made it clear that the present flood hazard maps are inadequate, and they must be revised".

This monograph was written in response to that call for "science-informed action!". It is therefore directed to the practising hydraulic engineer, who bridges the interface between writing reports and active management of post-disaster reconstruction. In particular it is aimed at *codifiers*, experienced supervising engineers in the often-overlooked role of revising legal Codes of Practice to guide practising engineers, when it becomes apparent (as now) that existing Codes are obsolescent and should be treated as such until updates have been issued.

Mapping Problems

In the monograph Chapter 2, current confusion between 1D, 2D and 3D model dimensionality is discussed with reference to conservation of volume. This principle was first introduced over 500 years ago by an eminent Italian hydraulic engineer. His definition has been translated by hydraulic historians (Rouse and Ince (1963)) as "A river in each part of its length in an equal time gives passage to an equal quantity of water, whatever the width, the depth, the slope, the roughness, the tortuosity." That engineer was Leonardo da Vinci, and his volume conservation principle is obviously 3D, as length, width and depth are all explicitly stated variables in the definition.

Chapters 2, 5, and 8 continue to trace back the identified issues with flood hazard mapping to misuse of numerical modelling techniques originally developed for other purposes. Mapping is a heavily mathematical procedure, involving the projection of three-dimensional data on a two-dimensional medium such as a GIS plot. In Leonardo's time this would have been a painting on canvas. In our time mathematical analysis is further complicated by the involvement of computational hydraulic models with all the problems associated with numerical analysis.

We here offer codifiers some background on the necessary analysis, with the expectation that many practitioners will prefer some of this material to be filtered out of engineering Codes in favour of pragmatic physical benchmark testing. "Validation" can be defined as the process of comparing model predictions with data from the real system to ensure that the model is suitable for generalisation.

Two real system benchmarks are presented in Chapter 8. For constructed channels the benchmark is a full-sized prototype flume element of a stormwater drainage system. For natural channels the benchmark is an urban reach of a natural river.

In both cases the possibility of experimental mistakes in the measurement of physical dimensions has been eliminated by mutual validation with a computational model reproducing Leonardo's principle with the *same* dimensions.

If validation failures cannot be traced to a case of poor experimental measurements, the problem must be substandard 3D hydraulic analysis. For this, responsibility for correction should be transferred from engineering practitioners to specialist model developers.

Allowance for Climate Change

IPCC predictions are of little help to engineers because they do not offer projections through the 21st century of either of the two fundamental flow parameters: peak flows and peak water levels. These are shown by Chapter 5 to be required for hydraulic design. Instead of discharge projections for our river and stormwater networks, we are offered projected rainfall intensities, and instead of peak level projections in local coastal waters we are offered global projections of mean sea level.

Future projection of the required design information has been the accepted task of engineers, based on application to historical records of Holocene climate stationarity until recent practice introduced by Chapters 3 and 6.

Few Codes of Practice have so far reacted to the need for specific guidance on accounting for Climate Change. Warnings that we are moving away from the previous assumption of climate stationarity serve no practical purpose unless accompanied by specific recommended replacement procedures.

Examples of suitable approaches are proposed in Chapter 4 for channel flow statistics where these rely on recordings of river gauging or controlled flow through structures such as lock gates or hydro power plants. Conversion of IPCC projected rainfall intensities into discharge figures at a local reference recording site is discussed using the hypothesis that "an unchanged catchment will again respond to rainfall of the same intensity by producing the same discharge." Discussion is awaited with interest, as this is more difficult to *disprove* than early discounted attempts (such as the "Rational Method") to suppose that peak discharge is linearly related to rainfall intensity.

For analysis of coastal water level statistics incorporating tsunami data, Chapter 7 proposes a suitable methodology. Again this depends on the identification of a local reference recording site, in this example at a deep harbour entrance where IPCC projections of sea level changes can be expected to provide a reliable base for direct adjustment of the recorded peak levels for climate change projections.

Acknowledgments

I was fortunate to study under two of the inspirational figures of hydraulics: Frank Henderson and Mike Abbott. It was Frank who later introduced me to James Ball, whose wide understanding of Australian practice has contributed much to this text. I am grateful to two former IAHR presidents, Joseph Lee and Nobuyuki Tamai, for providing my introduction to the team from Tohoku University. Fumihiko Imamura, Kwanchai Pakoksung and Anawat Suppasri have done a fine job of adding practical tsunami design experience developed under the pressure of living and working on the exposed Tohoku coast.

The completion of this monograph owes much to the perseverance of the review team led by Rob Ettema and Estibaliz Serrano. The patience of Ioan Nistor and Bryan Karney in picking through a rather tangled skein of ideas has (I hope) resulted in a more readable development of the important conclusions.

Finally, this project could not have been achieved without constant support and contributions from my wife Jane.

Alastair Barnett
HYDRA Software Ltd
Hamilton, New Zealand

Table of Contents

CHAPTER 1

Codes of practice for twenty-first century flood risk management

Alastair Barnett

HYDRA Software Ltd, New Zealand. E-mail: *barncon@xtra.co.nz*

1.1 | Introduction

This monograph demonstrates that the greatest challenge to practical flooding risk assessment in many countries is the failure of engineering Codes of Practice to respond to projections of devastating inland and/or coastal floods throughout the 21st century. Codes often do not adequately address several problems, including lack of instructions detailed enough for effective modelling of flood flows. This weakness places design engineers in an impossible position if they know the Code is flawed or obsolete. Legally, engineers must comply with the Code, but ethically they have a moral responsibility to risk prosecution by developing a possibly improved but non-compliant solution. Also, this dilemma demands focus on the role of the *codifiers* (people preparing codes), who are responsible for future frequent updates on best practice regarding flood risk management.

In this context, the Concise Oxford Dictionary succinctly defines a “code” as a body of laws “so arranged as to avoid inconsistency and overlapping”. English-language Codes of Practice (and those current in several countries using other languages accessible to the authors) have much in common, but display technical problems associated with “inconsistency and overlapping”, as discussed in the following chapters.

1.2 | Climate Change

There is a fundamental and significant inconsistency between traditional analysis based on stationarity and recent analysis based on projected climate change scenarios. The boundary between “traditional” and “recent” is somewhat arbitrary, but the IPCC use of 1990 as the boundary year is now widely adopted and is followed here.

Therefore stationary analysis continues to be recommended, but only until 1990. Practical adjustments onwards from 1990 for discharge boundaries are presented in Chapter 4, and for level boundaries (especially tsunami) in Chapter 7.

1.3 | Jurisdiction

The responsibilities of the design engineer vary from jurisdiction to jurisdiction, so design practice codification cannot fully rely on model design technical procedures from any single jurisdiction. For this reason, case studies are here provided from a range of jurisdictions familiar to the authors.

For example, unusually for codifiers, the Hong Kong Government Drainage Services Department has long been authorised to merge the analysis of sea level observations at several tide gauges around the harbour perimeter with the analysis of many rain gauges within the territory. This procedure enables them (see Ng (1994)) to develop a holistic analysis of the relevant data. Based on consideration of the design life L years of the proposed project, and the return period T years of the design event, two Cases are computed:

Case I: A T-year sea level in conjunction with an X-year rainfall
Case II: A T-year rainfall in conjunction with an X-year sea level
X is T/5 when T is up to fifty years, and X is ten when T is above fifty years (a “pragmatic rule”). The code-compliant design T-year flood level is then simply the higher of the two flood level Cases.

While this procedure pragmatically removes inconsistency as required, a more rigorous approach is now proposed here. As shown in Chapter 2, a potential project development site is selected, and linked to all conceivable sources of flooding by channels, which may already exist or require design as part of the development. Locations of the “sources of flooding” are defined by existence *there* of records of either water levels or channel discharges, as such data is required to define model-boundary conditions. For Hong Kong, an example of the available data relevant to the design engineer is presented as Table 7.1 in Chapter 7.

An unsteady 3D flow model is then run by the design engineer between the boundaries (typically the gauge sites nearest the project site on either side along the relevant low tide channels) for the duration of the records to synthesize a record of flooding *at the site* for the same period. The resulting synthesized project site data for sea levels can then be analysed by the recognised Hong Kong authority in the same way as for Table 7.1, but this time the tabulation applies to the *project site* instead of the tide gauge sites. This local tabulation should be returned to the design engineer for project risk assessment.

Design practice under Australian jurisdiction is discussed in Chapters 3 and 4. As shown in Chapter 4, the design engineer should devise a local site peak discharge tabulation similar to the event return period data in Table 4.1. Current practice assumes this is based on stationarity, so the necessary adjustments for climate change are proposed in Section 4.1.3 of Chapter 4.

Under Japanese jurisdiction, the duties of the design engineer are different. As discussed in Chapter 6, the 2011 Great East Japan Tsunami was unprecedented for at least 1000 years, leading to major changes in design practice overseen directly by the Cabinet Office of Japan. Computation of tsunami recurrence at specific coastal locations is a function overseen by authorities recognised by that Office. Design engineers for construction on a specific site are required to *download* rather than *devise* the required boundary data on tsunami recurrence at adjacent coastal locations.

Chapter 7 provides an example of the procedure now recommended for climate change adjustments under Japanese jurisdiction. A specific location designated “Point A” in a reference paper (Fukitani et al. (2021)) is suitably placed to provide a model boundary condition for tsunami wave height recurrence at the entrance to Tokyo Harbour. A plot in the reference paper has been downloaded and digitised to produce Table 7.6, the equivalent for tsunami wave height of Table 4.1 produced for peak discharges under Australian practice. Again the necessary adjustments for climate change follow in the text.

With all level readings, design engineers should remember that the numerical value represents a height above datum, meaningless if the datum level is not specified. The English speaking world traps the unwary by using “stage height” interchangeably with “flood level” to refer to a reading on a local flood gauge with no datum in common with other gauges along the river, and engineers need to avoid the same trap by careless use of “tsunami height” in translation from Japanese to English. In this case, as explained in Chapter 7, Section 7.2.2, all tsunami heights could be related to the undisturbed water level at Point A by a simple subtraction of 10 m from the downloaded levels.

1.4 | Overlapping Jurisdictions

At sites along shorelines and in harbours, much design effort relies on sea level observations by marine authorities, and on using IPCC projections of sea level rise with little consideration of rainfall depth-duration-frequency curves. Yet at adjacent sites, rain gauge observations by territorial authorities and projections of increasing precipitation intensities are the drainage design focus, rather than the probability distribution of extreme surge levels caused by marine upheavals.

Lateral inflows to channels may be neglected if the flows through the upstream and downstream boundaries are of comparable scale, but if residual differences are reliably detectable, those differences can be compared with continuously recorded rainfall data for verification by rainfall-runoff modelling. See Appendix A.

On sea coasts the downstream water boundary would be near the mouth of the harbour or river discharging the flood water, where the records of water level would automatically include peaks arising from tsunami, storm surge, and river floods. If the project is a power station, then the boundary condition time series is likely to be the tailrace discharge from a hydro turbine.

However the same methods also may be applied for developments inland, where the “downstream” water boundary would be the discharge point to a lake or major river which extends well beyond the territorial boundaries of a local municipal authority. There the key information required for transfer from the major river authority to the local authority would be all available records of relevant water levels over the previous several decades, together with known reports on the probabilities of all recorded flood peaks. Using this information, the local authorities would be able to optimise their choice between allowing backflow into their local tributary from the major river, making storage provision for outflow ponding when the local river level is below the major river level, or installing pumps to overcome any flood level deficits between their local river and the main stream of the major river. Discharge boundary conditions are dealt with in Chapters 3 and 4, whereas level boundary conditions (especially tsunami) are covered in Chapters 6 and 7.

Since shorelines and harbours and “adjacent sites” near the coast will overlap this century in many populated areas because of projected sea level trends, it would be wise in both zones to seek holistic practice which would consider all flood threats in parallel, whether they originate from the sky or the sea. If this practice cannot be achieved, every construction site in this combined littoral zone will be subject to one code-compliant design level for flooding under a territorial authority and another code for flooding under a marine authority.

There is no reason to expect comparable results, leaving the design engineer in the impossible position of choosing to comply with one code or the other (or neither). As the sea level is observed to rise, the marine-based threat may overtake the rainfall-based threat, but at different times at different sites. A further complicating factor is the likely coincidence of extreme storm rainfall with extreme storm surge, although not necessarily with the same probability (return period) for both contributors to a single event.

This dilemma of overlapping jurisdictions can be addressed under four categories of analysis:

A. Mathematical analysis. Many practising engineers typically become uncomfortable when confronted with “the alarming presence of partial derivative signs”, to quote Henderson (1966). Integral signs are also unwelcome. Fortunately, integral analysis of gradually varied steady flow profiles results in a simple, algebraic difference in energy levels measured at cross sections at the upstream and downstream ends of a channel reach. As shown in Chapter 2, this level difference must equate to the “head loss”, a weighted average of the “energy slope” as calculated at the reference upstream and downstream cross-sections.

Codes of Practice over the last seventy years have made use of this “calculus to algebra” device as demonstrated by Chow (1959), who presented the alternative Standard Step and Direct Step methods of hand computation. Even in Chow’s time these two methods were known to give different answers, so to meet basic code consistency requirements Chow recommended the Standard Step method as preferable for “natural channels” (3D channels in the terminology of this text).

Chapter 2 shows that these two methods differ only in the upstream and downstream weightings applied, and the chapter offers analysis harmonizing the two methods into a single algebraic procedure. This approach avoids previous code inconsistency, enabling discontinuous profiles such as the pond-channel transition benchmark (Chapter 2, Figure 2.3) to be computed and validated as shown in Chapter 8. Therefore, the harmonized-profile method is recommended for adoption in future editions of practice codes, especially for flood risk management involving three-dimensional (3D) channels, as are common for rivers.

B. Integral or differential analysis? The above-mentioned approach illustrates the relative ease with which integral analysis sometimes produces accurate algebraic expressions. This ease is why Chapter 2 introduces a generic formulation of conservation laws as “inflow – outflow = change in storage”. The momentum characteristics of a hydraulic jump is another longstanding case of analysis, published by Bresse in 1860 (e.g., Rouse and Ince, 1963). Although the derivation the analysis entails is usually presented directly in algebraic form in calculus terminology, this analysis strictly relies on profile integration through the jump represented by inserting a simple mathematical step function!

For computational solutions, differential analysis normally uses finite-differences to provide the “calculus to algebra” transformation of continuous profiles into a form suitable for numerical analysis. Unfortunately, this longstanding approach supposes that the curve can be represented by a polynomial with a limited number of terms to reduce the computational labour. Even with only *two* terms (a second-order polynomial), a finite-difference solution has a serious disadvantage, in accuracy and computation time, compared with a fitted-integral solution with only one parameter, such as the exponential and inverse-parabola (square-root) functions derived for flow profiles in Chapter 2.

Discontinuous functions, such as a step hydraulic jump or a gradient step at the pond-channel benchmark transition, are beyond the reach of finite-difference analysis, so integral analysis is superior in greater algebraic accuracy, computing speed, and tolerance of discontinuities. For all these reasons, this integral approach is used throughout this monograph to support algebraic solutions for presentation in practice codes used for flood risk management.

C. Adopted conservation principles. Abbott (1979) gives prime position to physical conservation principles and consequent equations involving *mass*, *momentum*, and *energy*. He shows that the mass, (linear) momentum, and energy equations may be expressed in terms of only two dependent variables, meaning that only *two* simultaneous equations are required for solution. Because of its simplicity, the mass equation is chosen first, leaving the practical choice of equations for computation as the mass-momentum couple or the mass-energy couple.

In Chapter 2, these principles are formally introduced and the need for a Code of Practice to distinguish between alternative equation couples is illustrated for a simple 3D model of a contraction from a pond to a channel in a laboratory flume. In Chapter 5 the discussion continues to good practice on the choice between mass-momentum and mass-energy couples specifically for treatment of hydraulic jumps. Chapter 8 then focuses on the pond-channel flume problem to demonstrate the practicalities of physically validating the choice of the mass-energy couple to generate accurate solutions over a robust range of model resolution.

D. Dimensionality. In his discussion, Abbott (1979) uses the one-dimensional conservation principles, in which vectors have only one component, the scalar magnitude. Vectors such as linear momentum can then be treated the same as 1D scalars such as length. In 3D, momentum is still a vector, so *must* be resolved into three components. Consequently, the mass-momentum “couple” has *four* dependent variables, with the corresponding need for *four* simultaneous equations in 3D. In contrast the mass-energy couple still requires only *two* simultaneous equations, because energy is still a scalar, but a 3D scalar related to volume. This is explained in Chapter 2. Chapter 5 illustrates the computational advantage of working with 3D scalars, as solution speeds are two orders of magnitude *faster* than working with 3D vectors, allowing models to run throughout decades within practical run times of minutes to hours on standard office laptop technology. Analytically, 2D vector solutions are recommended in Chapter 2 *only* to investigate flood-flow phenomena “which in their full three-dimensional form have so far proved intractable.” (Milne-Thomson, 1968). Computationally, they are still *one* order of magnitude *slower* than 3D scalar solutions, so they are not an attractive technology except in special cases where the mass-momentum couple is preferable, such as those discussed in Section 5.4.5 of Chapter 5.

1.5 | Compliance Assessment

Code compliance has traditionally been assessed by reference to clauses in the printed code, read one by one. With the advent of computational modelling, inconsistencies under Categories A to D above will theoretically be detectable *only* by examination of the computer programs making up a modelling package, and of their interaction with each other. A more practical way for a model user to assess such technology is now by model validation against a benchmark problem.

Chapter 8 offers a suitable benchmark in the pond-channel transition problem already discussed above. As well as offering great simplicity of full 3D channel definition (using only three cross-sections at three points each), this benchmark exercises the following features in a test model:

Mathematical analysis. The test model should be able to produce a longitudinal water level profile which is a drawdown curve through the pond-channel transition, then a straight line indicating uniform flow through the prismatic channel section. There should be a sharp gradient discontinuity connecting the two parts of the profile. Application of the specified levels at the upstream boundary should result in a steady discharge matching the tabulated laboratory results. For unsteady flow solutions a steady flow solution can be assessed by drawing down the downstream boundary level from a simple (but exact) hydrostatic solution to a constant level near the invert of the downstream cross-section.

Integral or differential analysis. Differential analysis will not be able to reproduce the drawdown curve, nor the sharp discontinuity in gradient at the connecting point at the two parts of the profile. As a result, the measured steady discharge is unlikely to be matched.

Adopted conservation principles. The energy solution should be robust, offering an excellent match to the tabulated laboratory results with all step lengths between 0.1 m and 2 m. The linear momentum solution should overestimate channel flow capacity at step lengths of 2 m, slowly converging to the correct solution at step lengths below 0.1 m (see Chapter 2).

Dimensionality. 1D models will correctly match flows in the prismatic section and fail in the transition section. Because the cross-sections are not rectangular, 2D models will fail in both sections. However, 3D energy models will correctly match flows in both sections, but linear momentum models will work only at high resolution.

In validity testing, the laboratory benchmark model is also exercised for accuracy of construction. The success of the 3D energy model validates the supervision of construction of the warped surfaces making up the transition, and of the prismatic channel. Uniform resistance of the installed laboratory channel surfaces was validated by successful calibration using a single value of the Manning *n*.

In addition to the pond-channel benchmark, validation of a test model is demonstrated using a large body of scale-field data from the Opanuku Stream in Auckland, New Zealand. This natural stream can carry floods up to the order of 100 cumecs, as is demonstrated in Chapter 8 by reference to the IAHR Resources Library. The details are given in Appendix A.

1.6 | Methodology

1.6.1 | General Principles

Proposed methodology elements are listed in the following sections. Many factors may contribute to the peak level of an extreme flooding event. Each element requires separate analysis before the results are merged into the final design level. However some general principles are proposed to apply.

Evidence-based analysis: First, analysis should rely mainly on local observed/collected data. Analysis based on remote data should be seen as of lower standard, being resorted to only if local data are not available or found to fail quality-assurance checks. For example, reliance on a single tide gauge (on the assumption that surge peak heights are representative of uniform behaviour in a whole region) fails in harbours such as Hong Kong, where careful analysis shows variations of a metre or more in design peak sea levels at different city coastal suburbs.

Future projections: Second, projection beyond the present (where observed evidence obviously ends) is necessary where there is good reason to believe that mean sea level, for example, is not stationary. However, such projections must be seen as provisional, and regularly adjusted in accordance with future evidence as that comes available.

1.6.2 | Elements of a building code

a) ***Design Lifetime:*** The design lifetime affects the need for future projections. If this is ten years or less, analysis should be based on existing evidence and no future projection is required. For minor projects with a more typical design lifetime of fifty years or more, consideration should be given to projecting only to half the design lifetime to avoid design levels being applicable only as the building becomes non-functional. In no case should projections extend beyond the design lifetime.

b) ***Tectonics:*** Tectonic effects in the design levels should be considered.
   - **Creeping movements:** There may be slow changes in the ground level through crustal deformation. Although generally barely detectable, they may be of the same order as projected sea level rise, increasing or decreasing the observed rate of rise, or even creating an apparent sea level fall.
   - **Earthquakes:** Many earthquakes have been observed to have significant vertical motion/ acceleration, sometimes raising or lowering the land by metres in a few seconds. Previous earthquake records from the same fault could indicate whether to expect further rises or falls.
   - **Tsunamis:** Certain earthquakes occurring under or in the nearshore vicinity of coastal areas can generate tsunamis initially mirroring the profile of the vertical crustal movement. Immediate waves caused by sudden horizontal displacement of vertical surfaces such as harbour breastworks can also reach high enough magnitudes to raise large ships on top of adjacent wharfs. However such wave effects are local, dissipating rapidly with distance from the generating structure. The shoreline response to tsunamis depends on local bathymetry variations, especially in harbours and nearshore coastal areas.

c) ***Subsidence:*** Ground levels may be lowered by subsidence. This may be caused by continual drainage pumping, as in New Orleans before Hurricane Katrina, or by liquefaction during a sudden earthquake shock.

d) ***Tidal range:*** High tide is the common benchmark for urban drainage, as it occurs once or twice per day, and is therefore reasonably likely to occur during a flood peak lasting a few hours. Projected mean sea level rises during this century barely reach high tide at many tide gauges, and fall well short of high tide at harbour sites with more extreme ranges.

e) ***Harbour resonance:*** Many harbours are relatively deep, allowing waves to resonate with little frictional damping. A disturbance at the entrance, such as a tsunami or storm surge, can carry periodic waves at harbour resonant frequencies, exciting the corresponding wave forms within the harbour. In such waves antinodes form at the ends of closed bays, reaching double the entrance wave height or more.

f) ***Wind-generated waves:*** During a storm, large swells may arrive at an open coast. Wind-generated waves will also appear within a harbour, depending on the wind speed and wave fetch. The amplitude of such waves must be added to the surface levels predicted from tide gauge records, which are usually damped to suppress such short period waves.

g) ***River floods:*** Many harbours are located at the estuary mouths of rivers large enough to raise the harbour levels significantly when in flood.

h) ***Local flooding:*** The local drainage system must be considered whether this relies on natural channels or constructed drainage networks. Extreme storm conditions will raise water levels throughout this system, and care must be taken that these do not exceed the chosen design storm level.

i) ***Direct Precipitation:*** The construction site itself will be subject to heavy local precipitation during extreme storms. Arrangements to dispose of this water through natural ground depressions or constructed drains will require some provision for a design water level above that applying to surrounding properties.

j) ***Damage limiting design:*** Once the design level at the construction site has been settled, urban flooding risks can still be reduced even when the undeveloped ground area is too low.

   - The building platform can be raised using excavated and compacted fill material.
   - The habitable floor level can be raised on piles or onto a flood-insensitive basement.
   - Heavy masonry construction can be used to deflect minor waves or floodwater away from sensitive areas.

k) ***Pumped drainage:*** Where gravity drainage is not practical for major flood events, the use of polders and floodwater pumping removes the direct link between internal design levels and exterior inundation levels. This is a common solution for buildings with deep basements. Any commitment to this approach must be considered as a solution requiring regular significant upgrades as sea levels and storm intensities continue to rise.

1.7 | Conclusions and Future Work

A practical approach to upgrading Codes of Practice is presented in the following chapters. This approach is recommended for adoption or adaptation by modelling and design specialists who have formed the opinion that their current code is obsolete. Consultation and discussion through the IAHR Flood Risk Management Technical Committee is welcome.

CHAPTER 2

Hydraulic principles

Alastair Barnett
HYDRA Software Ltd, New Zealand. E-mail: *barncon@xtra.co.nz*

Preamble: The need for hydraulics

Readers coming to flooding risk analysis from fields other than engineering may question the need for a chapter on hydraulic principles. The first edition of the Hong Kong Government Stormwater Drainage Manual (see Ng, 1994) gave the following explanation: “A hydraulic analysis for drainage planning or design is based on the runoff results of the various subcatchments loaded upon the geometry of the drainage system to give flood levels throughout the system. In the tidal reaches of the system, flood levels are also affected by the downstream boundary condition at the drainage outfall as defined by a sea level analysis.”

2.1 | Reproducible flow modelling

Reference to hydraulic principles depends on a shared set of fundamental concepts. A *reproducible* flow model is defined here as one which can reproduce results observed in a 3D physical laboratory space or in the field. The differences between reproducible and non-reproducible models are suitably illustrated by the historic laboratory investigations by Poiseuille throughout the 1830s: see Rouse and Ince (1963). The original laboratory work studied laminar flow in cylindrical tubes, and the resulting model is now named “Poiseuille motion”. The equation fitted empirically by Poiseuille to his many results was of the form

$$Q = f(T)\frac{hD^4}{L} \tag{2.1}$$

where Q was the discharge, T was the water temperature, and h was the static head difference between the ends of the tube, which was of diameter D and length L. In modern terms the function of T has been replaced by a function of viscosity, which links to temperature by a direct relationship based on consensus after many recent experiments. Yet this description of flow nearly 200 years ago still predicts discharges within one-half percent of modern laboratory results. Therefore Eq. (2.1) meets the criterion for the description of “reproducible”.

2.1.1 | Reproducible model dimensionality

Conventional terminology may confusingly refer to the *same* model as "1D", "2D" or "3D", depending on the context. For example, Poiseuille motion might be called "1D", on the basis that the equation predicts discharge, a scalar with no directional basis. Equally Eq. (2.1) might be called "2D" because this result for discharge supports a parabolic distribution across a cylindrical pipe for the axial velocity (Batchelor (1966)). This "2D" distribution turns out to be reproducible in the laboratory.

Finally, the model features a 3D scalar (discharge) and was first developed in a physical 3D space (the laboratory), supporting classification of the model as "3D". Vector algebra measures volume in 3D using a "triple scalar product" involving all three axes, then shows the outcome is the *same* for all choices of axes. Conventional descriptions of model dimensionality do not consider these realities of a model defined in physical 3D space. It follows that models defined in a strictly 1D or 2D space must be purely hypothetical if they are unable to transfer to a laboratory the full set of three spatial dimensions required to compute (for example) wetted perimeters of sections directly measurable in the laboratory. At best such limited models can apply only to subsections of the problem space within which some 3D approximation of 1D or 2D flow can be set up.

A 2D Cartesian model, for example, cannot generate reproducible 3D Poiseuille motion. Eq (2.1) can.

2.1.2 | Reproducible model scale

The reproducible model of Eq. (2.1) matches the experiments conducted by Poiseuille, but these were all carried out at small scale. Many investigations have since shown that Eq. (2.1) is no longer reproducible in the laboratory above a certain value of Q, expressed in relation to D by the Reynolds Number. According to Goldstein (1938) "The Reynolds number is defined for flow in a pipe or channel of any section as $4mu_m/\nu$, where m is the hydraulic mean depth (defined as the area of the cross-section divided by its perimeter), u_m is the average velocity over a section, and ν is the kinematic viscosity." By rewriting m as A/P and u_m as Q/A, the area A of the cross-section cancels and is no longer relevant, leaving the (wetted) perimeter P defining the scale of the tube. Then Goldstein's definition becomes

$$Re = \frac{4Q}{P\nu} \tag{2.2}$$

The integer 4 in the equation is necessary *only* because the hydraulic radius A/P of a circle is *exactly* $D/4$. This is an important reminder that the Reynolds Number scale is based on scalar 3D discharge and the *scalar* peripheral length around the channel section boundary, and *not* on some transverse vector dimension such as flow depth or pipe diameter D. If a vector treatment of wetted perimeter is attempted for full flow in a circular pipe, vector components from beginning to end of a polygon closely approximating a circle will sum to zero!

Many other dimensionless numbers have since been discovered to define the range of scales at which models are reproducible, leading to *dimensional analysis* developing as a specialist branch of hydraulics. This is well described in the textbook by Henderson (1966).

2.1.3 | Reproducible scalar flow modelling

Equation (2.1) is an example of scalar flow modelling which is reproducible even though there is no reference to 3D vectors.

The conceptual framework behind reproducible scalar flow modelling of surface flooding problems is illustrated in Figure 2.1, which shows a schematic view of the flow through a segment of channel at an initial time t_1 (left), then at a final time t_2 (right) a time interval later. This finite time interval (possibly decades) is called the *lifetime* of the model. The channel segment is isolated by external *boundaries* at Section 1 (upstream) and Section *n* (downstream), through which the *only* information representing outside influences on the flow is *either* the discharge *Q* *or* the free surface height *h* above datum level. Examples shown at time t_1 are Q_1, Q_L and h_n, superseded at time t_2 by Q_1', Q_L' and h_n' respectively.

A single graphic image cannot recognize all possible responses to initial conditions when modified by boundary conditions. However, the schematic represents a range of elements which can be treated

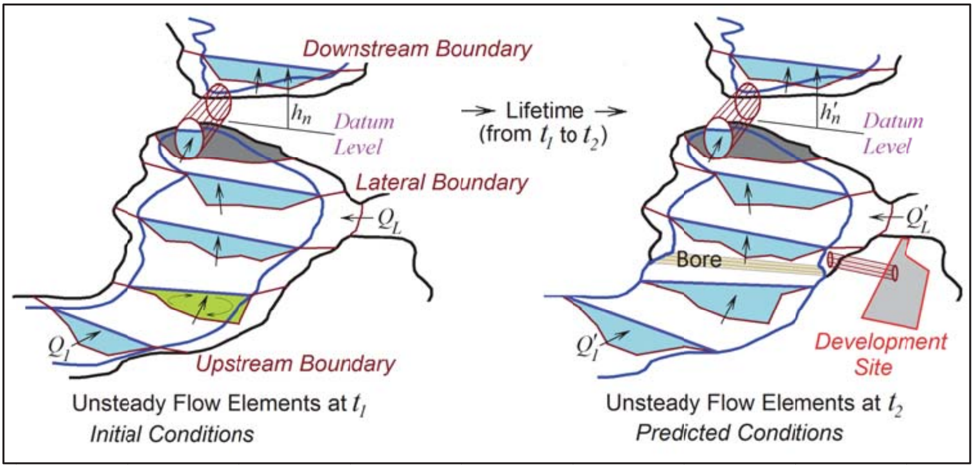

Figure 2.1 | A schematic of a 3D scalar flow model.

by reproducible scalar methods. These include an irregular fixed bed channel of varying depths and widths, a junction with a lateral channel through which whole flow networks can be connected, and pipes which are a component of hydraulic structures of all kinds, for example the many possible underground conduits of a stormwater drainage system, or the penstocks and draft tubes of a hydropower station. Inclusion of a “bore” represents conditions such as tidal surges (most famously at Hangzhou in China) or tsunami overland inundation, as well as other discontinuous conditions ranging from dam break waves below storage reservoirs to water hammer in domestic plumbing.

The circulation indicated in the green coloured cross-section recognizes that secondary currents can be expected within the plane of the section. As they do not directly contribute to the discharge, they are not of interest to the primary flow solution (Nezu (1994)). Yet if investigation of transverse effects is required, 3D vector modelling (sometimes called Computational Fluid Dynamics) cannot proceed until the primary scalar solution for discharge and free surface level has been made available. This is because such solutions develop from an upstream boundary specifying the Reynolds number (Cater and Williams (2008)).

In the context of surface flooding problems, The Reynolds Number *Re* is important only to check that an assumption of fully turbulent flow is valid. This is generally true for flood analysis at full scale, but must be considered before laboratory scale model results can be trusted. Overland turbulent flow models must also be treated with caution at low depths.

Flood flows arrive through channels in response to inflow increases or surge waves. Natural channels are irregular (see Figure 2.1), so must be defined in a model by 3D description of the channel bed. Such 3D boundaries may be physical (as in a scale model in a laboratory), or computational, but in both cases water boundaries at the open ends of a channel reach and the (possibly moving) free surface of the water complete the surface around a *control element* used as the conceptual basis of the model. Within each element, a balance equation will express a conservation law if

$$\textbf{inflow} - \textbf{outflow} = \textbf{change in storage}.$$

2.1.4 | Relation between conservation laws

This balance equation can be illustrated by deriving the conservation law for the simplest physical property: mass. Barnett (2014a) referred to the primary mass property of inertia to summarize the mass balance by the single integral expression $I = 0$, where I is defined as change in mass storage − mass inflow + mass outflow. Similarly (see Barnett 2014b) energy inflows, outflows and storage can be combined in a single expression $E = 0$, where E is defined as change in energy storage − energy inflow + energy outflow, and the momentum balance can be summarized by the single expression

$\boldsymbol{M} = \mathbf{0}$, where $\boldsymbol{M}$ is defined as change in momentum storage − momentum inflow + momentum outflow.

Note that E and I are both scalars, while $\boldsymbol{M}$ is a vector, so that "the single expression $\boldsymbol{M} = \mathbf{0}$" actually represents `three` scalar expressions, corresponding with the three scalar components of each 3D vector. Further, the energy, momentum and mass conservation laws may all be combined in the single scalar equation

$$E + \boldsymbol{U}.\boldsymbol{M} + {}^{1}\!/_{2}\,\boldsymbol{U}.\boldsymbol{U}\boldsymbol{I} = 0 \qquad 2.3$$

Here $\boldsymbol{U}$ is the velocity which may be added to *all* flow velocities by changing the motion of an observer measuring the flows. This principle of relativity of observed velocities dates back to Galileo (Abbott, 1979). Although $\boldsymbol{U}$ may have arbitrary magnitude (speed) and direction, these must both be *constant* during the lifetime of the model so the observer operates from an *inertial frame*, where a mass which is stationary (such as a lead weight hanging from a string) will remain stationary unless responding to unbalanced forces. For example, if the observer is in a train travelling along a straight smooth track, a weight carefully suspended motionless inside a carriage will not begin to move unless the train changes speed or direction.

Vector algebra defines the properties of scalar products (such as $\boldsymbol{U}.\ \boldsymbol{M}$), showing for an arbitrary value of the vector $\boldsymbol{U}$ that if $E = 0$, then *both* $\boldsymbol{M} = \mathbf{0}$ *and* $I = 0$ must also be true. These (energy, momentum and mass) are the three primary conservation principles used in hydraulics, so the corresponding set (2.3) of three equations (two scalar, one vector) may be called the *Full Hydraulic equations*.

Classical hydraulics has always used both energy and momentum principles based on convenience of solution in different situations. Historical engineering practice has often favoured Bernoulli analysis, which derives from the energy principle. Standard textbooks such as Henderson (1966) placed great emphasis on teaching the distinction between energy and momentum for association with the mass conservation equation in successful steady flow analysis. Although unsteady equation systems are commonly regarded as a generalization of steady equation systems, they are invalid and cannot be used for steady hydraulic analysis unless they reduce to the classical distinct energy, momentum and mass equations in the steady limit, that is, when change in storage tends to zero.

2.2 | The mass conservation equation

The general conservation balance expression **inflow** − **outflow** = **change in storage** can be adapted for mass as $I = 0$, giving the mathematical equivalent for the schematic in Figure 2.1 as the scalar integral equation:

$$\left[\int_R \rho dR\right]_{t_1}^{t_2} + \int_{t_1}^{t_2} \int_A \boldsymbol{n}.\boldsymbol{v}\rho dADt = 0 \qquad 2.4$$

where the physical parameters follow common terminology, except that in hydraulics V is not available for volume as it is commonly reserved for mean velocity, for example, in the Chézy formula – see Chow (1959). Instead dR is used for a volume element of the spatial *region* R inside the control surface, ρ is the mass density, t_1 and t_2 are as introduced in Figure 2.1, and dA is an element of the area A of the control surface through which inflows and outflows occur, in practice only the cross-sections at the channel ends. $\boldsymbol{n}$ is the normal to the surface (positive outwards), $\boldsymbol{v}$ is the water velocity in an inertial frame fixed to the channel bed, and Dt is a time increment, written with a capital D as it follows the (possible) free surface normal movement between t_1 and t_2. The scalar (dot) product of the vectors $\boldsymbol{n}$ and $\boldsymbol{v}$ then simply expresses the normal component (outflow positive, inflow negative) of the local fluid velocity.

Those more accustomed to finite difference analysis might note that computationally the first (change of mass storage) term and the second (inflow − outflow) term here are *exact* first differences of integrals, unlike the *approximations* to the first differences offered by Taylor series analysis.

2.2.1 | The "equation of continuity"

Finite difference analysis also requires expression of mass conservation in terms of the partial differential equation

$$\frac{\partial \rho}{\partial t} + \boldsymbol{\nabla}.(\rho \boldsymbol{v}) = 0 \qquad 2.5$$

Derivation of this equation may be found in many textbooks, and it has been described as a differential equivalent of the integral Eq. (2.4). However it is *less* fundamental than (2.4) because it rests on an assumption that the differential coefficients exist. Unfortunately, in hyperbolic problems which are the basis of wave mechanics, neither an assumption that the variable ρ is continuous in time nor that the product ($\rho\boldsymbol{v}$) is continuous in space are in general true, as the free surface may produce moving discontinuities in both. Also it is well known (Cunge et al, 1980) that disturbances propagate along characteristic lines, and these typically involve gradient discontinuities. In more severe cases, shocks develop which introduce discontinuities in the basic fluid properties, so that within the shock zones these differential coefficients no longer exist.

In case anyone believes that such shock zones can ultimately be resolved by adopting a sufficiently high resolution for analysis, Landau and Lifshitz (1959) estimate that the thickness of a strong shock is of the same order as the mean free path of the fluid molecules. In macroscopic fluid dynamics, the fluid is treated as a continuous medium, so they conclude “the mean free path must be taken as zero”.

Finite Volume methods were introduced in an attempt to correct this problem, but made the fundamental mistake of assuming timewise discontinuities would somehow disappear if provision was made for spacewise discontinuities. In most cases, spacewise discontinuities imply timewise discontinuities, as wave disturbance characteristics propagate in both space and time. Therefore in general there is no good reason to provide for spacewise discontinuities without also recognizing timewise discontinuities.

The differential form (2.5) of the mass conservation equation has been called “the equation of continuity” for many years, often without explanation. It appears to be an acknowledgement that differential analysis requires some kind of continuum hypothesis. Such a hypothesis cannot be sustained if it requires application down to length scales where the particle structure of the fluid dominates physical processes. Use of the integral form (2.4) of the mass conservation equation does not require the assumption of a dubious “equation of continuity”, so such terminology should be seen as obsolete,

2.2.2 | Reproducibility of the mass conservation equation

In hydraulics, experiments find water is virtually incompressible, except in well-defined special cases. Equation (2.5) then loses ability to account for change in storage, because the implied Eulerian control surface is fixed. Such Eulerian (fixed) elements are therefore not suitable for analysis of unsteady incompressible flows. Equation (2.4) allows the control surface to move to respond to differences between inflow and outflow by adjusting the storage as required. Introducing the assumption $\rho =$ constant to Eq. (2.4) then allows ρ to be cancelled out, leaving

$$\left[\int_R dR\right]_{t_1}^{t_2} + \int_{t_1}^{t_2} \int_A \boldsymbol{n}.\boldsymbol{v} dA\, Dt = 0 \qquad 2.6$$

This treats the fluid as having a constant specific density now defined to be 1 m^3/m^3. “Conservation of volume” is understood to refer *only* to such a fluid, so units of discharge such as “cubic metres per second” take a conventional meaning of referring to nearly incompressible material fluids, especially water. For the first term in Eq. (2.6), changes in volume are easily measurable using level gauges, so provided that the lateral boundaries can be assumed to be impermeable, the second term emphasizes that the computation of inflows and outflows requires information *only* at the upstream and downstream boundaries.

Therefore the distribution of velocity at any point between these boundaries has no effect on the computation of the mass balance. In tidal channels, it is common for periods of changes between flood and ebb tides for both inflows and outflows to occur simultaneously through the same opening. This may create some difficulty in assessing net discharges under experimental conditions, but these transitional discharge fluctuations are likely to be small compared with peak flood and ebb conditions, so resulting errors in the mass balance are tolerable.

Reference to a channel was made in Section 2.1.3, but the requirement for reproducibility of scalars within a channel is now seen to allow generalization of the definition of a “channel” to “An arbitrary shaped body of water connecting a flow entrance to a flow exit throughout a finite time interval.” A scalar mass balance channel model may then be reproducible for all times when lateral inflows and outflows are measurable or negligible, and unidirectional flow conditions are observed to be dominant at the entrance and also at the exit.

An important result for hydraulics is the concept of *steady flow*, in which absence of change in the levels of a reservoir signals an equalization of inflows and outflows. Such periods of negligible level change occur widely in nature, providing many opportunities for direct observation and model validation. In reaches with no significant lateral flow, the second term of Eq. (2.6) becomes $Q =$ constant. This applies to all steady reproducible modelling, so if the boundary conditions in (for example) CFD analysis do not satisfy this scalar criterion, then the results of that analysis will not be reproducible. The term “volume” relates only to 3D space, but if 2D and 1D versions of space are to be used to simplify suitable scalar problems, this fundamental simplification of steady flow is too valuable to be lost.

2.3 | 2D and 1D scalar analysis

2.3.1 | The 2D approximation to 3D

2D scalar analysis is a common simplification for ocean waves such as tsunami which change little along a crest, making analysis attractive with two orthogonal axes only: one (x) normal to the crest and one (z) vertical.

Such analysis is introduced as “2D” in classic texts such as Ippen (1966) and Milne-Thomson (1968). Milne-Thomson notes “Two-dimensional motion, as will be seen in the sequel, presents opportunities for special mathematical treatment and enables us to investigate the nature of many phenomena which in their full three-dimensional form have so far proved intractable.”

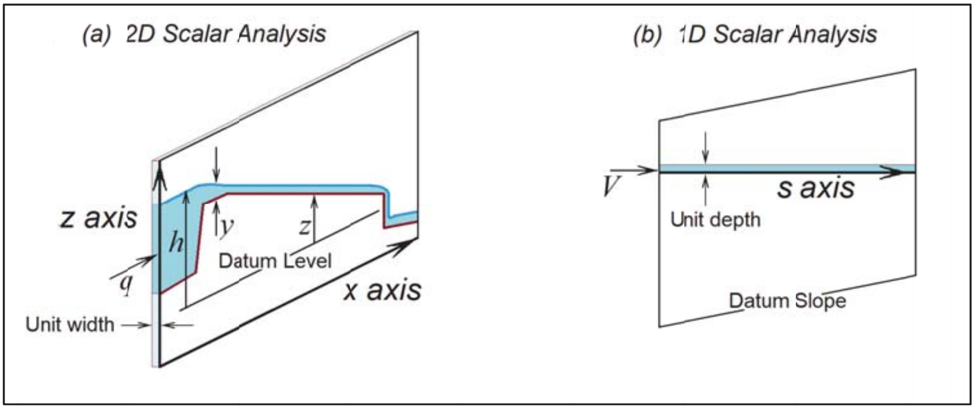

Figure 2.2 | 2D and 1D approximations to 3D physical space.

In wide rectangular channels, there is also little reason to expect lateral variation across the width, so again two axes only are required, this time with x along the channel and z again vertical. In general, some zones of insignificant lateral flow variation exist in physical 3D space, and in such cases shear between such zones can be expected to approximate vertical frictionless walls through which no significant lateral gradients can apply.

The conceptual model is then as shown in Figure 2.2(a), in which the units of the discharge q passing through unit width are m^3s^{-1} *per unit width*. The validity of this 2D analysis depends *entirely* on the assumption of lateral uniformity. *If* this flow is laterally uniform, and the total width is say B, then $q = Q/B$.

This allows any vertical slice to be representative of the whole cross-section, provided B remains constant throughout. Then q can take the place of the constant Q as simply a parameter in the derivation of important concepts such as the Froude number (see Henderson (1966)). Similarly, the 3D Reynolds Number defined by Eq. (2.2) can be converted to 2D by substituting $Q = Bq$ and $P = B$ to give $Re = 4q/\nu$.

Alternatively, flow and storage per unit width can simply be taken as a lateral mean, such that $q = Q/B$ again. Any expectation of linking the actual local value of q with this mean value must now be abandoned, but at least the 3D reference value of Q is preserved. If however B now varies along the channel, then q (the discharge through the slice of unit width) *must* vary longitudinally. Then it can no longer be treated as a parameter which is constant along the channel, and the 2D analogy with the 3D Q fails.

In short, if both Q and q are to be invariant, then the surface width B must also be invariant. If a reproducible scalar model was intended, B should have been allowed to vary irregularly without disturbing the steady invariance of Q.

2.3.2 | The 1D approximation to 3D

Going from 2D to 1D requires a similar conceptual argument, but this time as a search for zones of little *vertical* variation in 2D space. This is more difficult, because the effects of gravity create flow over fixed bed surfaces with a boundary layer within which the velocity is clearly non-uniform. However, in flows with a free surface, major parts of the flow profile outside the boundary layer may be sufficiently uniform for an assumption of minimal vertical variation to be treated as a first approximation.

There is also a new problem in dealing with the alignment of the z axis with gravity, while the x and y axes are usually both horizontal in Cartesian coordinates. How is it possible to define a single axis which combines the attributes of both x and z? The answer is a *datum slope*, as illustrated in Figure 2.2(b). A streamwise s axis is defined along which a 2D flow can be found to be *uniform* – in which the units of the discharge V passing through unit depth are m^3s^{-1} per unit width *per unit depth*. The validity of this 1D analysis depends *entirely* on the assumption of vertical uniformity. *If* this flow is vertically uniform, and the total depth is say y, then $V = q/y$. This allows any horizontal slice to be representative of the whole cross-section, provided y is constant throughout. Then V can take the place of the constant q as simply a parameter in the derivation of important concepts such as the Froude Number. Similarly, the 2D Reynolds Number defined above can be converted to 1D by substituting $q = Vy$ to give $Re = 4Vy/\nu$.

Alternatively, flow and storage per unit depth can also simply be taken as a vertical mean, such that again $V = q/y$. Any expectation of linking the actual local value of velocity with this mean value must now be abandoned, but at least the 2D reference value of q is preserved. If however y now varies along the channel, then V (the discharge through the prism of unit depth and unit width) *must* vary longitudinally. Then it can no longer be treated as a parameter which is constant along the channel, and the 1D analogy with the 2D q fails.

In short, if both q and V are to be invariant, then the depth y must also be invariant. If a true 2D scalar model was intended, y should have been allowed to vary irregularly without disturbing the steady invariance of q.

2.3.3 | Direct derivation of 1D from 3D

A direct transition is also possible from the 3D scalar space illustrated in Figure 2.1 to the 1D scalar space in Figure 2.2(b).

There is no need to introduce unit width and unit depth if a small area of arbitrary 2D shape can be scaled to have unit area and substituted for the square 1 unit x 1 unit area previously used. This unit area can then be allocated a corresponding share of the area-based mean velocity $V = Q/A$ passing through the whole cross-section. The 1D version of the Reynolds number then derives directly from Eq. (2.2) by replacing A/P with y, so that again $Re = 4Vy/\nu$. In a circular pipe flowing full, $y = D/4$, recovering the traditional form $Re = VD/\nu$. At least the 3D reference value of Q is preserved, but if A now varies along the channel, then V (the discharge through the arbitrary prism of unit area) *must* vary longitudinally. Then the 1D analogy with the 3D Q fails.

Summarising, the remarkable 3D steady flow property of a constant discharge throughout a reach can be reproduced only with a fixed flow width in 2D space (approximated by an idealized smooth-walled flume of rectangular section), and in 1D space only in flows of fixed cross-section area and slope (uniform flow).

2.4 | Solid boundary effects

2.4.1 | Conveyance

There are two primary dependent variables in the 3D scalar volume conservation Eq. (2.6): discharge Q and surface level h. They have a symmetry defined by steady flow, in which Q is constant with respect to scalar distance s along the (possibly curvilinear) channel axis, while h is constant with respect to time t. If a solution for h is found, and provided the solid boundaries are fixed, all cross-section variables such as area and wetted perimeter can be obtained. Similarly, if a solution for Q is found, and the solid boundaries are impermeable, then variables such as the mean velocity can be derived.

Therefore to allow solution, a second simultaneous equation needs to be added. This need for further information is most simply demonstrated by the observed requirement for steady uniform flow to be associated with a water surface slope.

The only simpler analysis applies to hydrostatics, where the discharge Q is zero and the water surface is horizontal ($h =$ constant). Therefore the requirement for a slope must be linked to the movement of water relative to the channel bed, with the resulting frictional and turbulence effects originating from the fixed channel boundary.

These effects can be viewed in terms of resistance to flow by the channel, or in terms of the responsiveness of flow through a channel to a difference between levels measured at each end. These two inverse concepts will be referred to as "resistance" and "conveyance" respectively.

Following Chézy in 1768 (see Henderson (1966)), the resistance, varying as the square of the mean velocity, is to be balanced against the propulsive force varying directly as the slope. This has a strong resemblance to the Poisseuille formula Eq. (2.1) featured earlier, except that for laminar flow, the head loss was found to be related directly to the discharge Q itself.

One of the hypotheses behind the celebrated later derivation of the de St Venant (1871) equations was translated by Cunge et al. (1980) as "The effects of boundary friction and turbulence can be accounted for through resistance laws analogous to those used for steady state flow." This means the equation for steady flow can be written as

$$Q\,|Q| = K^2 \frac{H_f}{L} \tag{2.7}$$

where K is the "conveyance" widely used in hydraulics, and H_f is the difference in head between one end and the other in a channel reach of length L, the scalar distance integrated between s_1 at the beginning and s_2 at the end of the (possibly curvilinear) reach. In uniform flow H_f equals h_f, the difference in surface level.

The conveyance, K, is often defined directly (rather than as K^2) using the square root of Eq. (2.7). However Q may vary between positive and negative, as in a tidal estuary, and this introduces computational problems in dealing with the choice of the + or – sign for the square root on each side of the equation. Also the repetitive evaluation of a square root in numerical models is time consuming compared with evaluating the simple first difference represented by H_f. Here, with K^2 positive, H_f/L simply takes the same sign as Q.

2.4.2 | Energy conservation or momentum conservation?

There are two options for calculating the "propulsive force" responded to by the "head loss" H_f. These are based on energy conservation and momentum conservation. Evaluation of Q through the required volume conservation Eq. [2.6] must be completed by evaluation of H_f, but only *one* of the two conservation other principles may be selected for use in any single problem.

Through relativity analysis, the two principles have been shown to be closely linked in Eq. (2.3). The analysis in Barnett (2014a) then used the "hydraulic" assumption of hydrostatic pressure distribution over the wetted part of the plane of each cross-section to simplify both balance equations. The balance equation $E = 0$ for energy conservation becomes:

$$\int_{s_1}^{s_2} \int_{t_1}^{t_2} \left[\frac{\partial}{\partial t} \left(\frac{Q}{A} \right) + \frac{\partial}{\partial s} \left(\frac{Q^2}{2A^2} + gh \right) + gS_e \right] dt\,ds = 0 \qquad 2.8$$

This integral scalar energy equation applies along a sloping s axis, which may be curvilinear as for the scalar mass equation. Here S_e is the "energy slope" which integrates to the head loss between s_1 and s_2. In steady flow the first term drops out, so according to the de St Venant hypothesis, the "head loss" is understood to be equal and opposite to the reduction in "energy head" as expressed in the second term of the equation (divided by g). The corresponding balance equation $\boldsymbol{M} = \mathbf{0}$ for momentum conservation has the x component:

$$\int_{x_1}^{x_2} \int_{t_1}^{t_2} \left[\frac{\partial Q}{\partial t} + \frac{\partial}{\partial x} \left(\frac{Q^2}{A} \right) + gA\frac{\partial h}{\partial x} + gAS_f \right] dt\,dx = 0 \qquad 2.9$$

Here S_f is the "friction slope" which also integrates to the head loss, this time between x_1 and x_2.

As the x scalar component of an integral momentum equation, Eq. (2.9) applies along a horizontal rectilinear x axis. It is described by Cunge et al. (1980) as "the 'momentum' equation generally used in engineering practice" (note: their usage of h is based on a datum of slope S_0).

The first two terms are both able to be integrated into *exact* first differences of integrals.

The third term is *not* able to be integrated so simply. The $A\partial h/\partial x$ term recognizes normal forces from the boundary walls and bed, which may apply at any intermediate point between successive cross-sections, for example in the model triangular flume contraction as shown in Figure 2.3. This presents a view horizontally downstream.

The foreground pond section (left half of diagram, green) is providing a downstream force through pressure from upstream, while the background channel (right of centreline, blue) is providing an upstream force through pressure from the channel. *In addition*, there is an upstream force from the x component of the reaction of the walls to the water pressure, which varies with the water level h applying at each wall surface element (right of diagram, blue). Figure 2.3 illustrates the choice of 0.5 m for the section grid spacing along a 2 m reach.

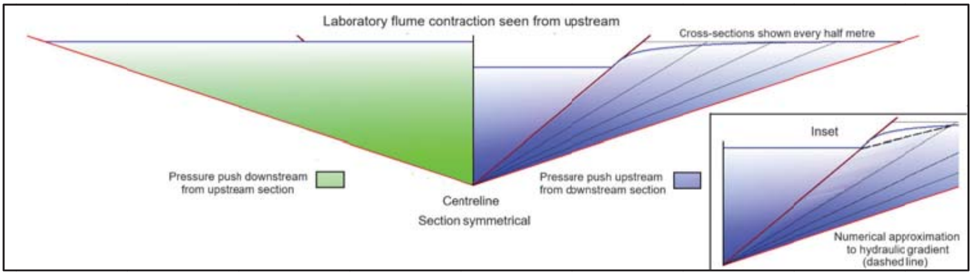

Figure 2.3 | Horizontal view through a test flume contraction carrying flow from a pond to a channel.

By breaking the channel reach into such length elements, a scalar computational solution of Eq. (2.9) can be produced for the longitudinal profile of the water level *h*. This can be trusted only after successive grid refinements produce solutions which converge on the same answers. The solution shown in Figure 2.3 reached convergence at a grid spacing of 0.1m, and the need to refine the original 0.5 m grid is shown by the pronounced remaining curvature of the convergent solution through each of the illustrated elements, in particular the downstream 0.5m element. See Figure 2.3 Inset. Here the drawdown slope approaches infinity, as in an overfall, because the downstream channel boundary for the solution was set to near-critical flow, where high water surface slopes are predictable (Henderson (1966)).

This means that computing the upstream wall force by taking an average value of *h* (see inset, dashed line) to find the hydrostatic pressure on the illustrated *x* projection of the sectors is a strategy that will work acceptably for the upstream three sectors, but that the downstream sector requires further refinement for acceptable estimates of the total wall force.

All this still assumes the wall varies smoothly through the transition, and indeed a continuous warped flume wall surface is physically reproducible (see Figure 8.1, Chapter 8) using straight-line generators. These are easy to use to interpolate the sections as assumed between the foreground and background in the Figure.

However the upstream wall force may be completely different if other interpolations are used, for example, the stepped square structure usually associated with Cartesian 2D model grids. Grid sizes used for representing changes of channel width are rarely below 1 m, an order of magnitude greater than the 0.1 m grid which is required here for convergence to a reliable solution of pool/channel transition at scales commonly associated with urban drainage.

Further, the solution shown in Figure 2.3 applies only to converging flow, which can be expected to behave in the manner illustrated. If the problem is inverted so that the flow width is *expanding* significantly, flow separation can be expected to occur, and this must be considered in evaluation of the wall pressures.

The second term in Eq. (2.9) (divided by g) can be rewritten using the known $Q =$ constant in steady flow:

$$\frac{d}{dx}\left(\frac{Q^2}{gA}\right) = -\frac{Q^2}{gA^2}\frac{dA}{dx} = A\frac{d}{dx}\left(\frac{Q^2}{2gA^2}\right) \tag{2.10}$$

This allows the integrand to be simplified as

$$\int_{x_1}^{x_2} gA\left[\frac{d}{dx}\left(\frac{Q^2}{2gA^2} + h\right) + S_f\right] dx = 0 \tag{2.11}$$

And so, since gA is never zero

$$\frac{d}{dx}\left(\frac{Q^2}{2gA^2} + h\right) + S_f = 0$$

Comparison with Eq. (2.8) (divided by g) shows that the definition for S_e and S_f is the same, except when the value of L in Eq. (2.7) is affected by the cosine of the slope of the s axis differing significantly from unity. This is uncommon, so both will now be denoted S_f, terminology more closely linked with the familiar H_f and h_f. This also shows that in steady flow, “head loss” refers to the *energy* head, whether the energy or momentum balance is used.

2.4.3 | Practical applications of energy conservation alone

Treatment of forces from fixed boundaries using the energy Eq. (2.8) is much simpler. The reduction in energy head integrates to a simple first difference between the foreground section and the background section in Figure 2.3, regardless of any intermediate variations in area. This is because an energy balance is concerned only with the scalar mechanical *work* done by the reaction of the walls to the water pressure. If the walls are fixed, no work is done, so effects of forces normal to walls are eliminated. Such effects are not a concern in 2D scalar problems, where the forces normal to the walls have no x component, although accounting for forces normal to the bed must still be provided, especially where bed steps occur.

Also, gradients of energy head are not strongly affected by near-critical flow, where extreme gradients of h can be computationally troublesome because of rapid transitions between potential and kinetic energy. The energy gradient can still become virtually infinite at waterfalls, but then no resistance or conveyance computation is necessary, as an energy model can simply be stopped at the head of the waterfall, and reset and restarted at the foot of the waterfall vertically below.

The same applies to hydropower flow discontinuities, where a dynamo can convert large quantities of mechanical energy to electrical energy or an electric pump can reverse this process, creating extremely steep gradients of mechanical energy in the flow without causing computational problems. This simplicity would certainly not translate to the momentum equation!

Forces parallel with the fixed walls and bed result in energy "losses" in the boundary layer (Landau and Lifshitz (1959)). Such boundary effects around the wetted perimeter are considered to be part of the resistance of the channel in parallel and converging flows, and can be seen as represented in the conveyance of the cross-section. In expanding flows, energy losses are conventionally treated by calibration through extensive physical studies at full scale and in the laboratory (see the discussion of "Channel Transitions" in Henderson (1966) and of "Nonprismatic channels" in Chow (1959)). According to Chow, "where there is no intervention of external forces or where these forces are either negligible or given, the momentum principle can be applied to its best advantage to problems, such as the hydraulic jump, that deal with high internal-energy losses that cannot be evaluated if the energy principle alone is used."

Further discussion on the practicalities of choice between momentum and energy analysis through hydraulic jumps will be deferred to Chapter 5.

2.5 | Non-uniform flow computations

2.5.1 | Numerical integration

In non-uniform flow K and S_f will no longer be constant throughout as assumed in Eq. (2.7), which now has to be replaced by conditions within a cross-section at some point along the channel, as in Eq. (2.12):

$$Q\,|Q| = K^2 S_f \tag{2.12}$$

At that point, S_f can be evaluated using the Manning formula for conveyance. This is (Barnett and Shamseldin (2008)):

$$K = \frac{MA^{5/3}}{nP^{2/3}} \tag{2.13}$$

Here M is a dimensioned constant ($= 1.00\,\mathrm{m}^{1/3}\,\mathrm{s}^{-1}$) and n is the "Manning *n*" roughness of the wetted perimeter.

To find H_f by integrating S_f between the ends of the reach of length L, numerical integration must be used. This is based on a number of control elements (see Figure 2.1) between sites at which cross-section surveys are available. For each of these elements, the increment in H_f is

$$\int_{s_u}^{s_d} S_f ds = (W_u S_{fu} + W_d S_{fd})(s_d - s_u) \tag{2.14}$$

where s is measured increasing downstream, so $s_d - s_u$ is positive. W_u and W_d are the upstream and downstream weights, respectively applied to the S_f values computed at the upstream and downstream sections. For example, the trapezoidal quadrature rule would simply set $W_u = 1/2$ and $W_d = = 1/2$.

In the case of non-uniform flow profiles, specialized weighting has been developed based on analytical methods using 2D scalar models. Though strictly these had been validated only on rectangular cross-sections until the pond-channel flume experiments introduced in Figure 2.3, benchmark test data is sparse for reproducible scalar models, and many model studies have since used them without problems.

2.5.2 | Backwater profiles

The backwater profile is called an M1 curve (see Henderson (1966)). It is characterized by $|S_{fu}| > |S_{fd}|$. The solution analysis is based on an exponential function and derived in Barnett and MacMurray (1998) as follows:

$$W_u = \frac{1}{2}(1 + 2L_b N), \quad W_d = \frac{1}{2}(1 - 2L_b) \tag{2.15}$$

where

$$L_b = \frac{1+I}{2} + \frac{1-I}{\ln I}, \quad N = \frac{S_0}{S_{fu}}, \quad I = \frac{S_0 - S_{fu}}{S_0 - S_{fd}}$$

Here S_0 is the datum slope, usually taken from a connection between the inverts of the sections upstream and downstream of each control element in turn. This connecting line is known as the *thalweg* – see Figure 5.2, Chapter 5. While this slope is not necessarily positive and may not be typical of the section as a whole in normal flows, it is essential that the datum slope remains relevant under low flow (and therefore low depth) conditions.

2.5.3 | Drawdown profiles

The drawdown profile is called an M2 curve (see Henderson (1966)). It is characterized by $|S_{fu}| < |S_{fd}|$. The solution is based on a Whitham front analysis for surge fronts propagating over dry land

(Whitham (1955)). It interpolates with an inverse parabola function and was adapted by Barnett (2012) as follows:

$$W_u = \frac{1}{1+I}, \quad W_d = \frac{I}{1+I} \tag{2.16}$$

Here I is as defined for Eq. (2.15).

CHAPTER 3

Magnitude ranking of river floods

James Ball
School of Civil and Environmental Engineering, University of Technology, Sydney.
E-mail: *James.Ball@uts.edu.au*

3.1 | Introduction

As outlined earlier, analysis of floods is premised on the desired flood analysis being either analysis of an actual flood event, or analysis for a design statistic. While these analyses are similar, there are differences which influence the outcomes. Nonetheless, the focus herein is the design analysis which can be stated as the estimation of a quantile for a flood characteristic; an example of a quantile for a design flood characteristic is the 1 in 100-year AEP (Annual Exceedance Probability) magnitude flow. Furthermore, there are many alternative forms of design flood problems. Hence there are many alternative flood characteristics requiring estimation of a design flood quantile.

While the flood characteristics important for management of a drainage system will vary between problems, Ball (2014) suggests that, typically, the flood characteristic of concern will be one of the following:

- Flood flow rate – the peak flow rate of the flood hydrograph is a common design flood hydrograph characteristic used, for example, to size drainage system components;
- Flood level – similar to the flood flow rate the peak flood level during a flood hydrograph is a common design flood hydrograph characteristic used, for example, in setting minimum habitable floor levels;
- Flood rate of rise – this design flood characteristic is a concern when evacuation planning is undertaken;
- Flood volume – this design flood characteristic becomes a concern when the design flood volume is a major factor in the design problem. This situation occurs when storage of a significant portion of a flood hydrograph is used as part of a flood management system. The design of storage structures to mitigate impacts of urbanization on the flood hydrograph is one example where flood volume is a concern; or

- System failure – the usual design flood problem is located at a single point. There are numerous design problems, however, where the critical concern is the prediction of design characteristics at multiple points within a system. Typical examples of these problems include urban drainage systems where the individual components of the system are not statistically independent which is a common assumption, and transportation routes with multiple cross drainage structures of one or more river systems.

The design flood problem is the estimation of a quantile for the desired flood characteristic. While there are alternative approaches to estimation of the design flood quantile, the selection of the design quantile typically is based on a risk management approach. For this approach, it is necessary to estimate both the magnitude of the hazard and the likelihood of the hazard. In other words, there is a need to consider the relationship between the magnitude and the exceedance probability of a design flood characteristic; an example of this relationship is shown in Figure 3.1.

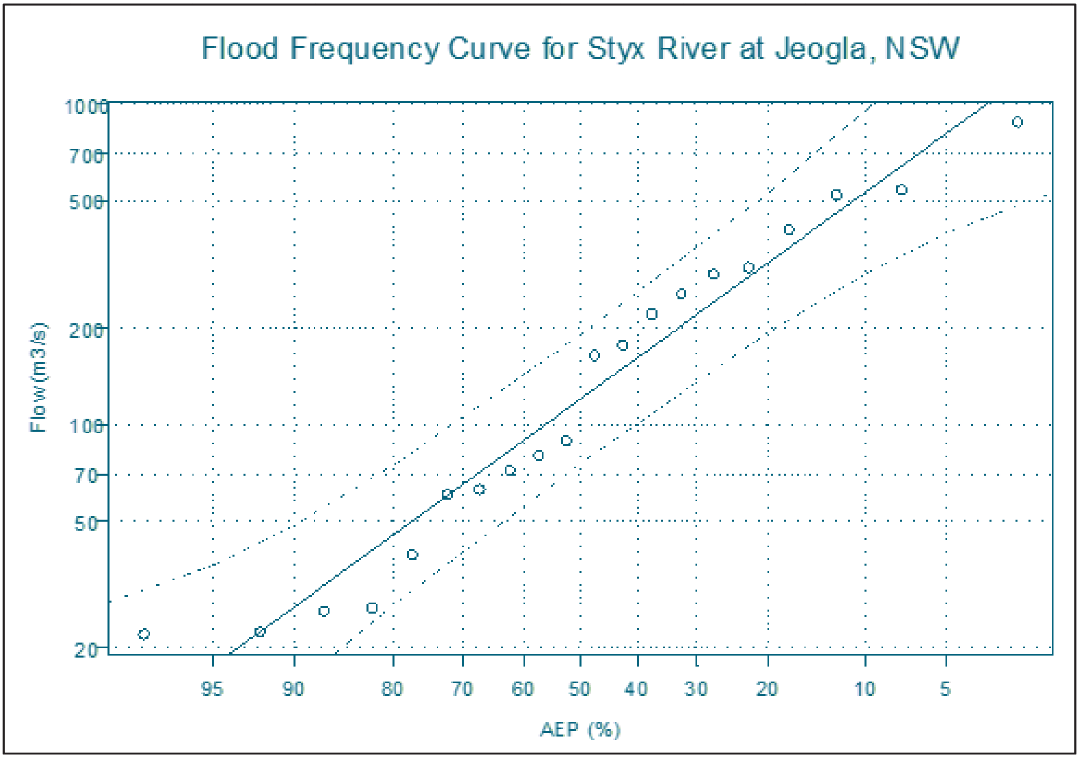

Figure 3.1 | Flood risk showing relationship between likelihood and magnitude.

Table 3.1 | Peak discharge Q vs return period T at the local gauging station.

DESIGN QUANTILE (AEP)	EXPECTATION OVER 70 YEARS Occurs At Least Once	 Occurs At Least Twice
1 in 10	99.9%	99.3%
1 in 20	97.0%	86.4%
1 in 50	75.3%	40.8%
1 in 100	50.3%	15.6%

When a standards based approach forms the basis of the design flood estimation, the primary focus is the estimation of flood characteristics for a defined quantile, or likelihood, rather than estimating flood characteristics over a range of likelihoods. For these circumstances, the design problem becomes one of estimating a single point on the risk profile.

When selecting a design standard, the performance of the system over time should be considered. While the design standard defines the probability during a single year, the expectation of the event occurring over multiple years needs to be considered. If a 70-year period of time is considered, then the expectation for at least one and at least two occurrences of an event in that period are shown in Table 3.1. As shown in this table, there is a 1 in 2 chance of a person experiencing one 1 in 100-year AEP magnitude flood during a 70 year life and approx. a 1 in 6 chance of experiencing two 1 in 100-year AEP magnitude floods during the same period.

3.2 | Basic flood statistics

Probability concepts are fundamental to design flood estimation. The use of appropriate terminology that embeds the statistical nature of design flood estimation is important for effective communication of design flood estimates. Terms commonly used in the past have included “recurrence interval”, “return period”, and various terms involving “probability”. It is common for these terms to be used in a loose manner, and sometimes quite incorrectly. This has resulted in misinterpretation by the profession, the general community impacted by floods, and other stakeholders.

Use of the terms “*recurrence interval*” and “*return period*” has been criticised as leading to confusion in the minds of some decision-makers and members of the public. Although the terms are simple superficially, they are misinterpreted regularly as implying that the associated event magnitude is only exceeded at regular intervals, and that they are referring to the expected elapsed time till the next exceedance. This misinterpretation of the terms used for expressing probabilities of flood magnitudes can be misleading and result in poor decisions.

It is believed that irrespective of the terms used, it is critical that all stakeholders have a common interpretation of the terms. Furthermore, it is important that stakeholders understand that the terms refer to long term averages. This means, for a given climatic environment, that the probability of an event of a given magnitude being equaled or exceeded in a given period of time (for example, one year) is unchanged throughout the life of the structure; in other words, the system is stationary. Many regions of the world experience wet and dry phases with these phases likely to be clustered in time. The occurrence of these wet and dry climatic phases highlights the misleading and inappropriate interpretation that flood events occur at regular intervals as implied by "*recurrence interval*" and "*return period*".

Use of the terms "*recurrence interval*" and "*return period*" and similar terms intended to express expectations of periods between events are premised on climate stationarity over sufficiently long periods of time for multiple occurrences to occur. Climate change has resulted in changing climatic environments. Hence, terminology that relates the probability to short periods of time, typically one-year, where the assumption of climatic stationarity is reasonable would be preferable to alternatives.

For frequency analysis of flood characteristics, it is common to assume that that the flood characteristics are independent random variables. In other words, it is assumed that each realisation of a flood characteristic is statistically independent of other realisations – see for example, Stedinger et al. (1993). In its most general form, the flood probability model can be described by its Probability Density Function. Hence, Flood Frequency Analysis is the fitting of a statistical model (i.e., a probability density function) to the available observed data. One of the great advantages of fitting a probability flood model to observed data is that the approach avoids the problem of considering the complex joint probabilities involved in flood generation processes.

However, there is no universally accepted flood probability model that is applicable to all catchments. As a result, many types of probability distributions have been applied to Flood Frequency Analysis. Unfortunately, it is not possible to determine the true probability distribution, and there is no rigorous analytical proof that any probability distribution for flood characteristics is the correct theoretical distribution. The appropriateness of alternative distributions can be tested by examining the fit of each distribution to the observed flood data. Various empirical tests of different distributions have been carried out with recorded data from many catchments, however, conclusive evidence is not possible largely because gauged records are of insufficient length to eliminate the confounding effect of sampling variability.

The choice of flood probability model is further exacerbated by recent evidence that the flood record is not homogeneous due to long-term climate variability; in other words, the observed data does not adhere approximately to the stationarity assumption.

3.3 | Choice of data series

The most common flood characteristic considered using a frequency analysis is the peak flow during a flood event. The flood stage typically is not used in Flood Frequency Analysis as the flood stage is very dependent on the geometric properties of the cross-section; given the significant changes in cross section geometry when the flow transitions from in-bank to out-of-bank flows, there are likely to be discontinuities in the statistical model. As a result, the probability models typically used in flood frequency analysis may not fit the peak stage data adequately.

For a valid frequency analysis, the data used should constitute a random sample of independent values, ideally from a homogeneous population. While there are many approaches to the collection of streamflow data (see World Meteorological Organization, 2010), the continuous records are the most useful for frequency analysis. Discrete values, or events, are extracted from these continuous records, and it is these discrete values that are analysed during the frequency analysis. The problem of assessing independence of events, and of selecting all independent events, is illustrated by a streamflow record shown in Figure 3.2. Peaks A and B are not independent of each other but are serially correlated, while peak D is independent of A and B. However, the independence of peak C with respect to A and B is open to interpretation. Are the independent peaks in the record B and D, or B, C and D?

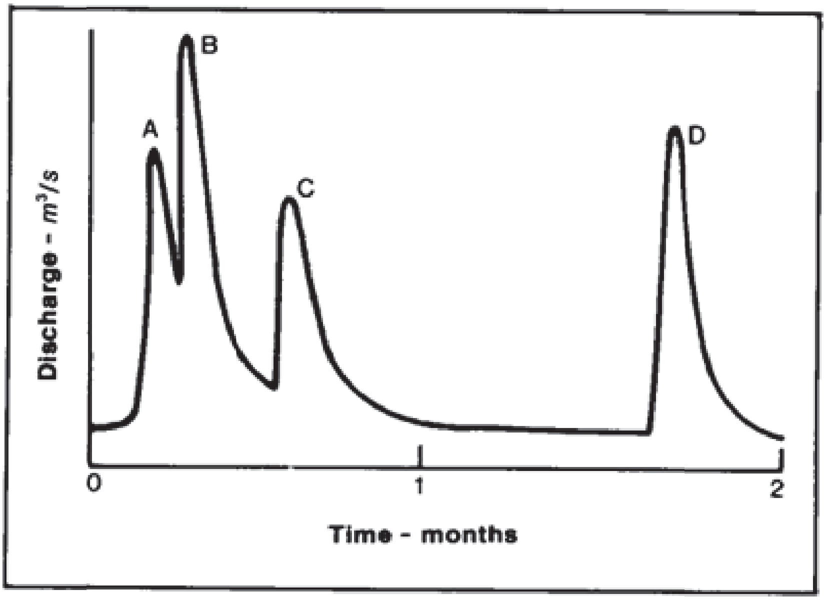

Figure 3.2 | Flood hydrograph showing difficulty in selecting independent events.

Lack of homogeneity in the sample of flood events is another practical problem. Typical causes of the lack of homogeneity are changes in the collection of data, or in the nature of the catchment. Examples of these changes include:

- Construction of large storages, levees and channel improvements
- Changes in land use such as clearing, different farming practices (inclusive of farm dam storages), soil conservation works, re-forestation, and urbanization.
- Change of gauging station site, or site conditions

The record should be carefully examined for these and other causes resulting in a lack of homogeneity.

Two types of flood data can be extracted from such a record; these are:

- Annual Maxima Series (AMS)
- Peak Over Threshold Series (POTS)

The AMS is formed by extracting maximum discharge in each year. This yields the series $\{q_1, \ldots, q_n\}$ where q_i is the maximum discharge in the i^{th} year of the n-year record. The data in the AMS can be used to estimate the probability that maximum flood discharge in a year exceeds a particular magnitude q. In Australia, this probability is referred to as the Annual Exceedance Probability AEP(q).

The POTS is formed by extracting every statistically independent peak discharge (that exceeds a threshold discharge), from the record. This yields the series $\{q_1, \ldots, q_m\}$ where q_i is the peak discharge associated with the i^{th} statistically independent flood event in the record of m events extracted over n years. As discussed by Laurenson (1987), a requirement for statistical independence is independence of the physical causative factors resulting in floods (primarily, rainfall and antecedent wetness). This type of independence is necessary if the POTS is used to estimate the distribution of annual floods. Typically, the threshold discharge is selected so that m is about 2 to 3 times greater than n. An advantage of the POTS is that, when the selected base value is sufficiently high, small events that are not really floods are excluded. With the AMS, non-floods in drought dominated years may have an undue influence on shape of the fitted probability distribution.

Langbein (1949) presented a relationship for the conversion of probabilities between AMS and POTS. This relationship is shown in Figure 3.3.

3.4 | Typical distributions

As previously noted, there is no universally accepted flood probability model. Hence, it is usually inappropriate to be prescriptive regarding choice of flood probability model. As a general rule, however,

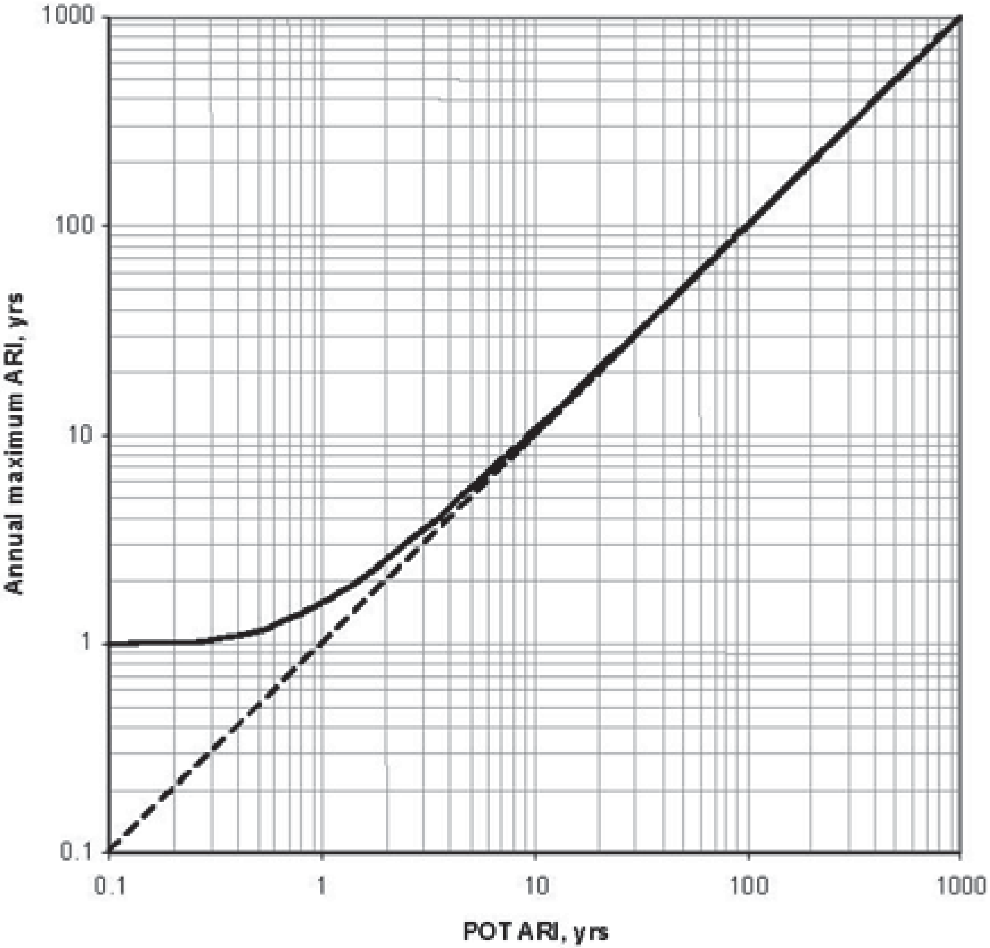

Figure 3.3 | Langbein (1949) Relationship between AEP and ARI (after Ball et al., 2019).

the selected probability distribution family should be consistent with available data. It is recognized also that more than one probability distribution may be consistent with the available data. When extrapolated to rarer events (outside the range of events experienced), however, predictions may vary significantly.

For the AMS, two distribution families commonly used are the Generalized Extreme Value (GEV) and the Log Pearson III (LP III) families. These families fit most AMS flood data adequately. Nonetheless, users are reminded that there is no rigorous justification for these families; this is particularly important when extrapolating.

Both distribution families are three parameter distributions. In POT modelling, the Generalized Pareto (GP) distribution is often found to satisfactorily fit the data. However, LPIII distributions have been used also for POTS.

Kuczera and Franks (2019) present details of these distributions and their moments.

3.5 | Fitting distributions to data

Fitting a flood probability model involves three major components:

1. Calibrating the statistical model to the available data to determine the parameter values consistent with the data.
2. Estimation of flood quantiles and their confidence limits.
3. Evaluation of goodness of fit and consistency of model with data.

Within each of these components, there are steps towards completion of the component. The first of those steps is the development of an empirical probability plot. The purpose of the empirical probability plot is to visually check the adequacy of a fitted distribution. This requires an estimate of the likelihood (or exceedance probability) plotted against the observed discharge.

For an AMS, the production of a probability plot requires:

- Rank the gauged discharges in descending order (that is, from largest to smallest) yielding the series $\{q(1), q(2), \ldots, q(n)\}$ where $q(i)$ is the rank i of the i^{th} largest flood;
- Estimate the likelihood for each $q(i)$ using a suitable plotting position estimator; and
- Using suitable scales plot the estimated likelihood against $q(i)$.

A general formula (Blom, 1958) for estimating the likelihood (P_i) of an observed flood flow is:

$$P_i = \frac{i - \propto}{n + 1 - 2 \propto}$$

where i is the rank of the gauged flood, n is the number of years of gauged floods and α is a constant whose value is selected to preserve desirable statistical properties. In practice, several choices for α exist:

- $\alpha = 0$ yields the Weibull plotting position that produces unbiased estimates of the probability of $q(i)$;
- $\alpha = 0.375$ yields Blom's plotting position that produces unbiased quantile estimates for the normal distribution; and

- $\alpha = 0.4$ yields the Cunnane (1978) plotting position that produces nearly unbiased quantile estimates for a range of probability distributions.

A more complete discussion on plotting positions can be found in Stedinger et al., (1993). Also, it must be stressed that plotting positions should not be used as an estimate of the actual probability of an observed flood discharge. An estimate of this type should be obtained from the fitted probability distribution. Note that estimating the likelihood from a discharge via the fitted probability distribution is not statistically correct as the regression relationship used is for a given x (likelihood) what is the best estimate of y (discharge). However, for most practical problems, the suggested approach will provide reasonable estimates.

Judicious choice of scale for the probability plot can assist the evaluation of goodness of fit for the empirical probability. The basic idea is to select a scale so that the data plot as a straight line if the data is consistent with the assumed probability model.

This concept is best illustrated using an example. If the floods in the extracted series are assumed to follow an exponential probability distribution, plotting $q(i)$ against $log_e P_i$, the data, if it is consistent with the exponential probability distribution, should plot as a straight line.

Similar situations exist for other probability distributions. For example:

- If the data is expected to follow a Gumbel distribution, a straight line should result if $q(i)$ is plotted against $-log\,[-log\,(1 - P_i)]$. Data following a GEV distribution will plot as a curved line.
- For a log normal distribution, a straight line should result for $log\,q(i)$ plots against standard normal deviates with exceedance probabilities P_i. Data following a LPIII probability distribution will plot as a curved line.

The next step is the calibration of the statistical model to the available flood data. No one calibration technique has been shown to be applicable to all situations. Nonetheless, alternative calibration techniques include:

- Bayesian
  Bayesian techniques are very general approaches for calibrating and identifying models. The use of these techniques for calibrating the statistical models necessary for FFA has become feasible only with the advent of computational power and new methods employing that computational

power. Stedinger et al. (1993) observes that “the Bayesian approach... allows the explicit modeling of uncertainty in parameters and provides a theoretically consistent framework for integrating systematic flow records with regional and other hydrologic information”. While general discussions of the Bayesian technique are provided by Lee (1989) and Gelman et al. (1995), Kuczera and Franks (2019) present a discussion of its application in FFA. Included in the discussion of Kuczera and Franks (2019) are example applications; in these example applications are the inclusion of censored data, the inclusion of errors in the extrapolation portion of the rating curve, the inclusion of regional information regarding the parameter values, and low-flow censoring of flows in the AMS.

- L- and LH-Moments
  The L-moments technique was developed by Hosking (1990) to overcome the bias and sensitivity of the method of moments approach to calibration of statistical models. It is claimed that L-moment estimators are unbiased and are less sensitive to outliers than method of moment estimators; the technique is based on linear combinations rather than combinations using powers. When L-moments were applied, it was found that the lower discharges may exert an undue influence on the calibration and give insufficient weight to the higher discharges. Wang (1997) introduced a generalisation of L-moments called LH-moments to mitigate this issue.
- Method of Moments
  The method of moments is a technique for estimating the parameters in a statistical model. In other words, the method of moments is based on estimating the expected values of the moments of $log q(i)$. As the majority of the data in a flood series will be for frequent events (i.e., low flows), there is potential for these lower flows to exert an undue influence on the calibration and give insufficient weight to the higher discharges. For that reason, Kuczera and Franks (2019) do not recommend the use of this approach for FFA in Australia. On the other hand, Bulletin 17C (England et al., 2018) recommends its use in U.S.A.

Irrespective of the calibration technique applied, the result are estimated values of the distribution parameters (and, in some cases, their uncertainties) for the adopted probability distribution. The remaining step is the use of these distribution parameters for estimation of the desired quantile(s). Use of these estimated values for the probability distribution parameters depends on the selected distribution. For example, when the LPIII distribution is used, the quantile q_y (i.e., the discharge with a 1 in Y years AEP) is given by:

$$\log\left(q_y\right) = m + K_y\left(g\right) s$$

where m, s and g are the estimated LPII distribution parameters (i.e., mean, standard deviation and skewness) of the log discharge and K_y is a frequency factor well-approximated by the Wilson-Hilferty transformation. Details of an approximate calculation method for K_y are given by Chow et al. (1988).

On the other hand, if the GEV distribution is assumed, the 1 in Y year AEP quantile is given by:

$$q_y = \begin{cases} \tau + \frac{\alpha}{\kappa}\left[1 - \left(-\log_e\left(1 - \frac{1}{y}\right)\right)^{\kappa}\right], & \kappa \neq 0 \\ \tau - \alpha \log_e\left(-\log_e\left(1 - \frac{1}{y}\right)\right), & \kappa = 0 \end{cases}$$

where τ, α, and κ are the estimated GEV distribution parameters (i.e., the location parameter, the scale parameter, and the shape parameter).

3.6 | Handling non-stationary data

Most FFA are attempted on flood peaks that form a homogeneous data series. A more complicated situation arises when the flood peaks do not form a homogeneous data series. This situation, typically, arises when rainfall and flood mechanisms change over time. Examples of these reasons for these changes include:

- The climate may experience pseudo-periodic shifts that persist over periods lasting from several years to several decades. There is growing evidence, in parts of the world, that flood peaks are not identically distributed from year to year and that flood risk is dependent on long-term climate variability. Within Australia, Erskine and Warner (1988) first introduced the idea of alternating flood and drought dominated regimes that exist on decadal and longer timescales.
- Long-term climate change due to global warming may render the flood record non-homogeneous.
- Long-term land use change and river regulation also may render the flood record non-homogeneous. A common cause of non-homogeneity in flood records is the construction of storages (reservoirs) in the catchment. While these storages usually do not influence the flood generation, the storages change the transmission of the flood through the catchment thereby producing a change in flood characteristics at the site of interest. As the usual need is the current and potential future flood risk, a common approach for management of the data series is to convert pre-dam construction flood data to equivalent post-dam construction flood data using an appropriate catchment model. A similar approach can be used when potential catchment storage is removed through construction of levees (also referred to as dykes and stop-banks).

In addition to changes in the rainfall and flood mechanisms, flood peaks may not form a homogeneous data series due to the manner of data collection. Changes in data collection may result from:

- Change of gauging station site.
- Instability at the gauging station – for example, changing cross sections due to sediment erosion and deposition.

- Changes in the extrapolation portion of the rating curve used to convert the measured stage to a recorded discharge. The extrapolation portion of the rating curve is that portion of the rating curve above the highest concurrent measurement of flow and stage (i.e., gauging). As discussed by Ball et al. (2016), the extrapolation portion of the rating curve can influence the extracted AMS. They reported that over 20% of the gauging stations in NSW, Australia had over 50% of the AMS values in the extrapolation zone, and in-bank gaugings formed the basis of extrapolation for approx. 75% of the gauging stations.

The climate-dependence of flood risk is an important consideration when assessing flood risk. Most flood frequency applications will require assessment of long-term flood risk; that is, flood risk that is independent of a particular current climate state. If a flood record is sufficiently long to sample all climate states affecting flood risk, a traditional analysis assuming homogeneity will yield the long-term flood risk. Unfortunately, many flood records are relatively short and may be dominated by one climate state. Blind use of such data can result in substantial bias in long-term flood risk estimates. For this reason, it may be necessary to investigate the homogeneity of the flood distribution.

The practitioner undertaking an FFA needs to assess the significance of such factors and identify appropriate exogenous variables to condition the flood probability model. However, it is stressed that this is an area of continuing research and, therefore, practitioners are advised to keep abreast of new developments.

3.7 | Joint probabilities

Flood events are the result of many generation and transmission processes. Many of these processes vary spatially and temporally. Hence, the probability of a flood event is influenced by the individual probabilities of these processes; in other words, the probability of a flood event is the result of the joint probability of the influential processes. For many catchments, the dominant processes are associated with the precipitation. However, this is not always the case.

Floods in estuarine environments are an example where rainfall is not the only dominant process. As outlined by Westra et al. (2019), floods in estuarine areas can be caused by runoff generated by an extreme rainfall event, an elevated ocean level generated by a storm surge and/or a high astronomical tide, or a combination of both processes occurring simultaneously or in close succession.

Research internationally and in Australia (Zheng et al., 2013) has shown that extreme rainfall and storm surge processes are statistically dependent, and, therefore, this interaction needs to be considered for areas affected by both processes.

Figure 3.4 shows two hypothetical water levels: the level obtained by assuming that fluvial floods will always coincide with storm tides of the same exceedance probability (upper curve); and the level assuming fluvial processes and ocean processes are completely independent and thus will almost never coincide (lower curve) (after Ball et al., 2019).

This is an illustration of the joint probability associated with flood events in the estuarine zone. There is a region where the riverine flood defines the flood risk, and there is an area where the ocean flood defines the flood risk. In between these two regions, there is a zone where the flood risk is dependent upon the joint probability of the two flood producing mechanisms.

A development of the background to estimation of joint probabilities suitable for consideration of this situation is presented by Westra et al. (2019) and, hence, will not be presented herein.

Alternative approaches have been developed to handle estimation of this joint probability. These approaches include:

- Flood Frequency Analysis - This approach involves fitting a probability distribution to a time series extracted from historical data. While conceptually easy to implement, the need to check data to ensure its suitability is greater in these situations. Furthermore, the approach requires long, high-quality historical flood records at the location of interest and that these records be stationary. The advantage of this approach is that, by directly focusing on the statistical characteristics of historical floods, it may be possible to avoid modelling the complex processes that lead to estuarine floods.

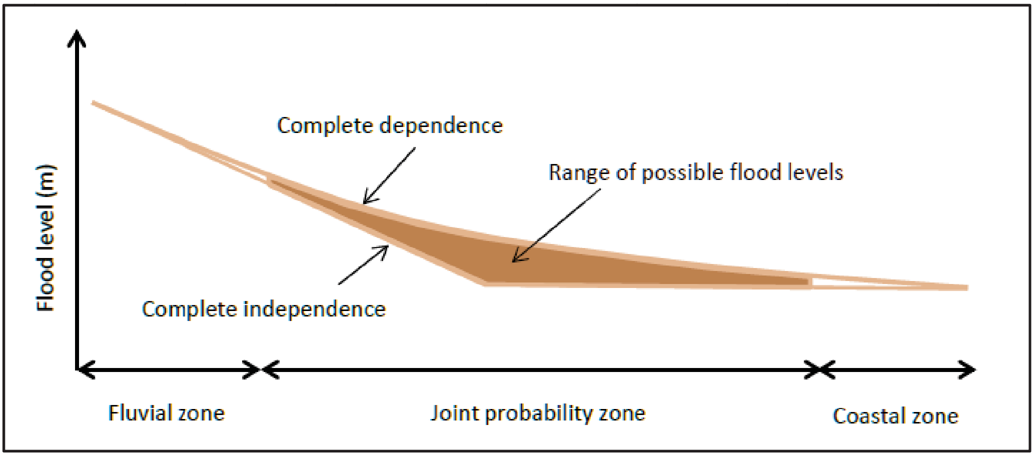

Figure 3.4 | Schematic of a longitudinal section of an estuary.

- Simulation – floods in the joint probability zone can be influenced by many processes operating at a range of timescales, including sub-daily variability in tides, storm surges and the flood hydrograph from the upstream catchment, superimposed on lower-frequency variability at daily, seasonal, annual and inter-annual timescales. In many cases, dynamical features, such as the progression and attenuation of tides up the estuary, can significantly influence flood behaviour. Simulation approaches aim to simulate these complex dynamics over a variety of time scales. Hence, continuous approaches are employed usually. The computational load of continuously running integrated hydrological, hydraulic, and ocean models at the short time steps required over extensive periods of time necessary for estimating flood probabilities is often extremely high.
- Design Variable Approach – As outlined by Westra et al. (2019), the primary assumptions of the approach are:
  - The statistical dependence between extreme rainfall and storm surge can be represented through a bivariate logistic extreme value dependence model.
  - The dependence strength can be interpolated between gauged locations.
  - The Annual Exceedance Probability of the rainfall event is equivalent to the Annual Exceedance Probability of the flood event (AEP Neutral assumption commonly used with catchment models).
  - Ocean water levels are assumed to be ‘static’, as tidal dynamics are not considered explicitly in the method.

The validity of the assumptions necessary for application of the design variable approach need to be considered when applying the approach to a specific flood estimation problem, and weighed against assumptions associated with alternative approaches. For many situations, the design variable method is a pragmatic approach that can be applied across a range of estuarine flood estimation approaches.

CHAPTER 4

Recent directions in practical adjustments for non-stationarity

Alastair Barnett

HYDRA Software Ltd, New Zealand. E-mail: *barncon@xtra.co.nz*

James Ball

School of Civil and Environmental Education, University of Technology, Sydney.
E-mail: *James.Ball@uts.edu.au*

4.1 | Interaction between rainfall intensity changes and peak flood flow probability

4.1.1 | Principles

Chapter 3 discussed estimation of the probability of peak flood flows based on historically observed data under the assumption of climatic stationarity. Discussion of the non-stationary effects of climate change suffers the problem already identified, that gauged flow records from the particular river of interest to the design engineer are unlikely to be of sufficient length to provide reliable guidance on the effects of climate change since 1990 on peak flood flow probability.

However, rainfall intensities are now regularly gauged in many locations, and any resulting records provide a rich guide to climate variability since 1990, both within a catchment and across adjacent catchments. Deterministic catchment models (such as the kinematic wave method) indicate that rainfalls of extreme intensity, for example those with an ARI (Average Recurrence Interval) of at least 50 years, will tend to swamp the soil infiltration and depression storage components of catchment response, leaving direct surface runoff more and more dominant. The storage effect of larger reservoirs will still be significant, but this is amenable to direct observation and modelling by deterministic hydraulic analysis.

A direct relationship between rainfall intensity and catchment outflow can therefore be expected if a high enough intensity prevails for long enough (the “time of concentration”). The very existence of an outflow peak marks the beginning of flood recession, which can then be seen as a delayed response to lessening rainfall intensity as averaged across the catchment. At such peak catchment outflows in such extreme storms, a reasonable hypothesis is then that *an unchanged catchment will again respond to rainfall of the same intensity by producing the same discharge*.

If climate change is causing rainfall intensities of the same AEP (Annual Exceedence Probability) to *increase* above stationary values, this hypothesis requires that the rainfall intensity corresponding with the stationary discharge must become more probable, or in other words, have an *increased* AEP.

4.1.2 | A Typical Problem

The simplest example is a problem involving only essential data. Then the same basic principles can readily be transferred to more complex datasets.

Test Problem: Suppose a large house was designed for a 50 year lifetime in 1990. For background illustration, the house has been constructed on a bank above the highest flood level observed in over 70 years of records. However the Consent Authority has noted concern about the location of the house on the outside of a river curve, where bank erosion has approached the foundations during two previous large floods. Application has then been received by the Authority to approve significant enlargement of the house by adding a second floor, and in response the house owners have been required to apply for a new building consent in 2022. They have then engaged a flood engineer to prepare the necessary redesign. How should that engineer proceed?

The first task is to relate the observed previous erosion damage to the damage expected from the design flood. Most erosion protection design manuals assume the design flood discharge and level have been established before their procedures begin, and this preparatory stage is the subject of this Chapter.

For this example, representative discharge values were extracted from the results of an At-site Flood Frequency Analysis presented by Kuczera and Franks (2019). This plot was developed using recorded discharge measurements in a medium sized river at a local flood gauging station, which for present purposes will be assumed to be near the problem house.

The peak flood discharge Q is tabulated against the return period T in Table 4.1. For return periods of 10 years or more, the return period or ARI (Average Recurrence Interval) can adequately be approximated by the reciprocal of the AEP (Annual Exceedence Probability obtained from Annual Maxima), as shown in Figure 3.3 (Chapter 3).

Using modelling techniques, the original design engineer had concluded that a 50-year flood would cause bank erosion, but that there was a sufficient land margin between the river and the house for

Table 4.1 | Peak discharge Q vs return period T at the local gauging station. Extracted from Figure 3.2.49 of Kuczera and Franks (2019).

Peak flood discharge Q (m^3/s)	401	539	625	688	740	784	825	862	895	922
Return period T (years)	10	20	30	40	50	60	70	80	90	100

such erosion to be repairable without damage to the house. Therefore a design discharge of 740 m^3/s had been approved.

However that engineer had been unable to report confidence that erosion from larger floods would still be safe. The question then becomes "by how much should this historically based design discharge be modified by changes in rainfall intensity predicted by climate change?"

There is increasing confidence among climatologists that successive IPCC climate change projections have been found to be accurate, at least within the limitations of the short time interval since 1990 over which those projections may be tested. The key climate factor for flooding is precipitation intensities, and these may now be compared with historical values at any site where recording rain gauges have been installed. Rain radar and satellite imagery have recently provided data complementary to the "ground truth" of rain gauges.

4.1.3 | Comparison of lifetime probabilities

The *expectation* of the design capacity being exceeded *at least once* over its design life L_d is conventionally represented by P for *probability*, a closely related concept. P is given by the Hong Kong design manual (see Ng (1994, 2018)) as

$$P = 1 - \left(1 - \frac{1}{T_d}\right)^{L_d} \tag{4.1}$$

Eq. (4.1) is the *stationary* case. Note that the design life is treated as an integer, so that the function in parentheses is evaluated only *once* per year for each of L_d years. This enables T_d to be interpreted as the reciprocal of a specified AEP, which also applies to whole calendar years.

In the *non-stationary* case, such as during climate change periods, the return period T is no longer constant. For example, if the return period can be shown to vary as in the exponential Eq. (4.5) below, the resulting effect on design lifetime is illustrated in Figure 4.1.

The black lines (Compliance boundary) show that after the design lifetime of 50 years (2040) the worked example follows Eq. (4.1) for the stationary case (blue line), predicting a probability of flooding of 63.6%. This value turns out to be very close to all other cases where the designed project life is

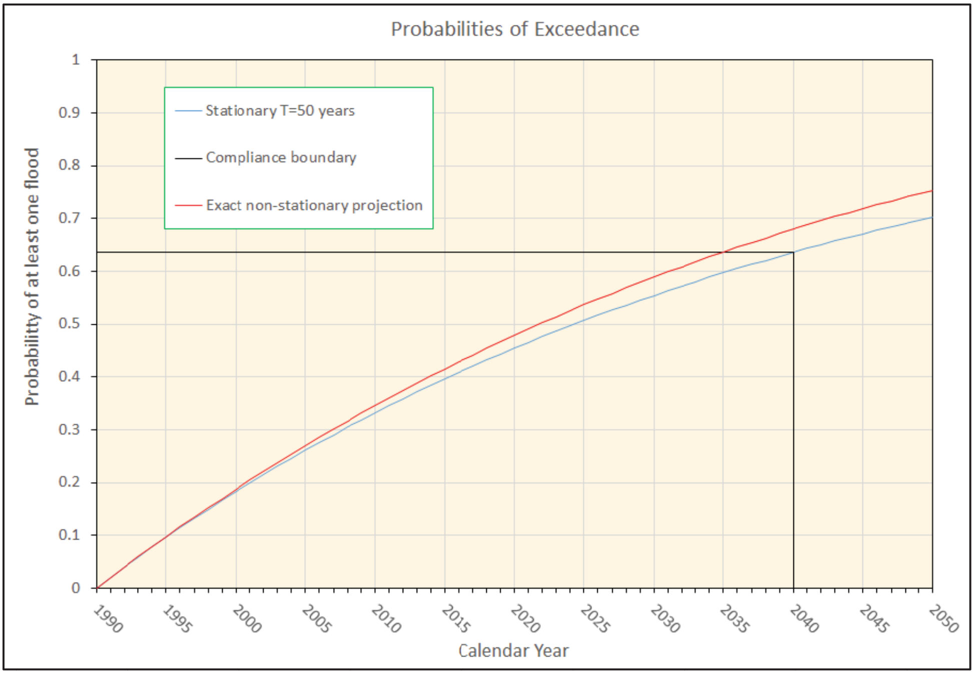

Figure 4.1 | Comparison of design lifetimes for stationary and non-stationary projections.

set equal to the stationary design return period T_d, suggesting that this percentage could be defined as the boundary between acceptable and unacceptable probability of failure. At the threshold where a projected curve crosses this line, the lifetime L of compliance with acceptable probability can then be taken to end.

The red curve (Exact non-stationary projection) is the projection produced by calculating exact successive values of T according to Eq. (4.5) in the example below. The compliance boundary then predicts a reduced project lifetime L ending in 2035 after 45 years, only 90% of the design return period. (Note that the word “exact” here refers to the numerical solution of Eq. (4.1), *not* to the values of T_d derived by statistical analysis, where “exact” does not exist),

4.1.4 | Assumed local rainfall intensity changes

Inspection of projections of local climate change by climatologists reveal features in common, as projections are presented for two future years, fifty years apart. Some use 2050 and 2100, rounded to calendar half-centuries, while Macara et al. (2019) make projections on the basis of “historic” figures, and use 2040 and 2090, reflecting 50 and 100 years from 1990. This suggests an assumption that the historic stationary situation ended at 1990, when there is a consensus that modern climate changes first began to be significant. This does not imply that climate change impacts did not exist before 1990, but they were small enough for measurements to be controversial because of the noise existing in all weather related signals.

Starting from 1990 then, projections are made to an earlier year (2040 or 2050), regarded as reflecting a dominance of greenhouse gas emissions which have already occurred, and which cannot be modified, and to a later year (2090 or 2100), seen as a time when climate change may still be modified by significant human interventions to stabilise the rates of anthropic greenhouse gas emissions.

An illustrative sample is presented in Table 4.2 of data from the study by Macara et al. (2019). The full report tabulated projections for 16 locations in the Otago region for both a 50-year and a 100-year ARI. Also four climate change scenarios from the 2013 IPCC Fifth Assessment Report were covered, from which RCP 4.5 has been selected here as representing a lower (optimistic) stabilization scenario, and RCP 8.5 as representing a higher (pessimistic) "business as usual" scenario. As the largest population centre of the 16 locations, the city of Dunedin was chosen here as representative, on the grounds that it is likely to host the greatest concentration of long term rainfall recording stations in the region.

However, lifetime probability assessments work with annual records, throughout which conditions applying in 2040 or 2090 have no more significance than in any of the intervening years within which a major flood may occur. Accordingly, some means of interpolation between rainfall depth values given specifically for the three years 1990, 2040 and 2090 must be found. The same scenarios from IPCC reports are documented for each of the three reported years, and on inspection the 1990 figures may be seen as the base, while later figures may be compared with the base by differencing to compare the rate of change at 2040 with that at 2090. The lower (optimistic) scenario displays a rate of change to the later date *lower* than that to the earlier date, while the higher (pessimistic) scenario displays

Table 4.2 | Data from Macara et al. for the city of Dunedin with a 50-year ARI under RCP4.5 and RCP8.5.

	Stationary (Historic) Depth	**2040**		**2090**	
	mm	RCP4.5	RCP8.5	RCP4.5	RCP8.5
1 hr/50 yr ARI	27.1	29.8	30.2	31.5	36.5
6 hr/50 yr ARI	65.1	70.5	71.3	74.0	84.0
12 hr/50 yr ARI	89.9	96.5	97.5	101.0	113.0
24 hr/50 yr ARI	121.0	128.0	129.0	133.0	147.0
48 hr/50 yr ARI	156.0	164.0	165.0	170.0	185.0

Table 4.3 | Comparison between the behaviour of illustrative low and high scenarios.

Rainfall depth/1990 depth	1990	2040	2090
Low scenario (RCP4.5)	1.000	1.073	1.122
High scenario (RCP8.5)	1.000	1.084	1.259

a rate of change to the later date *higher* than that to the earlier date. This behaviour is illustrated by representative figures listed in Table 4.3.

Here the change figures have been made dimensionless ratios by division by the 1990 values for rainfall depths. The results of this procedure may be seen to vary slightly between the 1 hour and 48 hour durations tabulated, but the ratios shown are the mean of the results for the five durations. By inspection, these mean ratios are also very close to those for the median (12 hour) duration, so they have been taken to be representative. In the light of the hypothesis introduced in Section 4.1.1, these ratios may be applied to stationary 1990 discharges in Table 4.1 to derive revised return periods applying in 2040 and 2090.

This will be likely to show increasing flood discharges for the same AEP over the years, but it is the inverse problem of *decreasing* return periods (increasing AEP values) for the *same* flood discharge (the design discharge) which is of interest here.

4.2 | Worked solution

4.2.1 | Interpolation of the representative scenarios

By inspection, the scenarios in Table 4.2 are not amenable to interpolation using an exponential growth curve, such as arises from semilog analysis. Since interpolation is required between three points in time, the simplest approach is a quadratic equation, which may be fitted to all three points. This would take the form

$$\frac{i_t}{i_d} = at^2 + bt + c = \frac{Q_d}{Q_t} \qquad 4.2$$

where t is the time in years from 1990, a, b and c are standard coefficients in a quadratic, i_t is the interpolated rainfall depth at year t and i_d is the design rainfall depth as at 1990 (the base value for Table 4.3) corresponding with an AEP of 2% for return period 50 years. As mentioned above, the Q ratio has had to be inverted, because Q_d is fixed at the design discharge (740 m^3/s), while Q_t now means the 1990 Q value *from which* the precipitation intensity increase produces the design discharge. At

1990, $t = 0$, so $c = 1$. This makes it convenient to define the relative change in discharge k by

$$\frac{Q_d - Q_t}{Q_t} = k = at^2 + bt \tag{4.3}$$

Simultaneous equations in a and b can be set up for $t = 50$ and $t = 100$.

The results for the low scenario in Table 4.3 are $a = -0.0000048$ and $b = 0.0017$, while $a = 0.0000182$ and $b = 0.00077$ for the high scenario. These values may then be applied to the evaluation of k for any t.

4.2.2 | Computation procedure

Computation of the projected effects of climate change on the AEP of major floods may be approached by reference to Figure 4.2. There are two charts in this Figure, with the left hand chart representing the data in Table 4.3, while the right hand chart represents the data in Table 4.1.

The working procedure starts from chart "Projected Increases to Discharge" on the left side. This plots the value of k found from Eq. (4.3) against calendar years, which begin from 1990 in this example. The high and low scenarios from Table 4.3 are plotted, together with a weighted average usually chosen by the consenting authority. To demonstrate the procedure in this example, the weights were arbitrarily

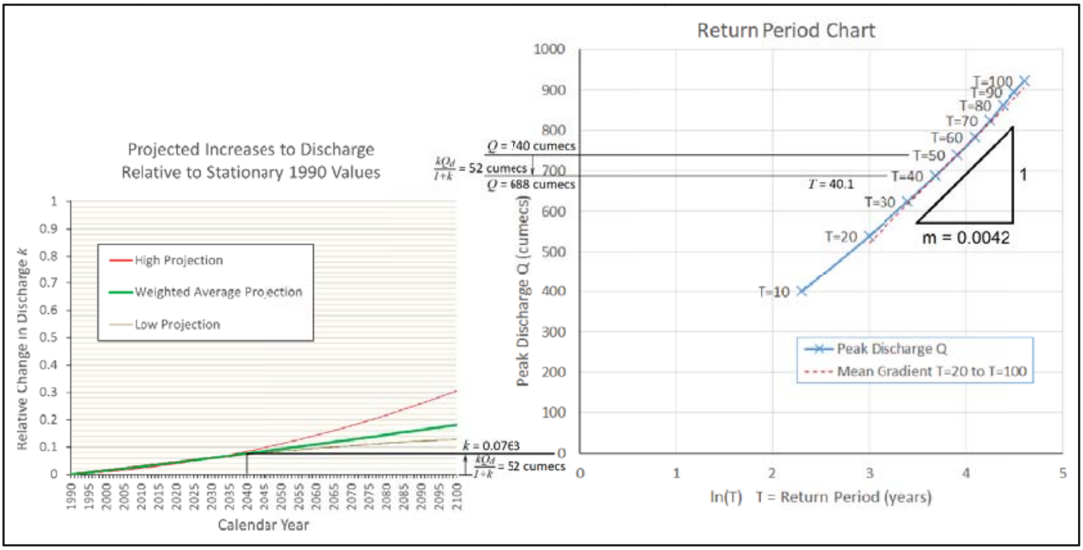

Figure 4.2 | Working charts of climate change adjustment computation procedure.

set at 0.3 for the high scenario and 0.7 for the low scenario. Values were then computed for each year by spreadsheet, and plotted.

All values of k increase year by year, and by inspection, the plotted values happen to converge near the year 2040, the end of the 50 year design life specified for many of the materials used in construction. The weighted average projection of k at 2040 is 0.0763. Referring to Eq. (4.3), the projected increasing intensity of precipitation by 2040 will add another 52 m^3s^{-1} (cumecs) to the flood peak, an effect which can be represented graphically by raising the Return Period Chart by the same amount when discussing the year 2040.

Turning to the right hand chart, subtracting the 52 cumecs from 740 cumecs gives 688 cumecs. This plots at 740 cumecs above the original axis position, but because of the axis shift the return period for the same total peak has reduced to 40.1 years. This has been computed from the semilog fit

$$\ln\left(T_t\right) - \ln\left(T_d\right) = -m\left(Q_d - Q_t\right) = -m\frac{k}{1+k}Q_d \qquad 4.4$$

A more convenient form for spreadsheet tabulation is, writing T for T_t

$$T = T_d e^{-m\frac{k}{1+k}Q_d} \qquad 4.5$$

The gradient m used was 0.0042, the gradient of a line joining the points for $T = 20$ and $T = 100$, and then shifted to pass through the point at $T = 50$. The result is plotted as a dashed red line superimposed on the blue curve connecting the points listed in Table 4.1. By inspection this line is an excellent match to the blue curve between $T = 35$ and $T = 70$.

This is the only zone of interest for this procedure, as shown by the sample adjustment illustrated in Figure 4.2.

4.2.3 | An example beginning from 2022

To return to the problem posed in Section 4.1.2, a design engineer advising a client on application to authorities for a consent for new capital construction work should begin again from the year of the application, in this case taken as 2022. There may be differences between authorities in different countries with the definition of “new capital construction work”, but generally the distinction between maintenance and capital work is based on whether or not guarantees of durability of building components exceed the required building lifetime. Wall and roof claddings exposed to harsh climatic conditions are not usually expected to last without maintenance as long as internal structural elements, which are more protected. In the stated problem, the proposed addition of a second floor to the entire building would go far beyond the normal understanding of “maintenance”.

If the structure has been damaged by a flood event (or other natural hazard), then repairs to all but superficial damage should be treated as new capital construction and a fresh consent obtained before reconstruction begins. Once the necessary application has been completed and approved as compliant with current building codes, the lifetime of the project begins again and the cumulative probability of another such design event occurring as at that moment should then be reset to zero.

The resulting projections of probable lifetimes for construction projects completed and put into service in 2022 are presented in Figure 4.3. This is an extension of Figure 4.1 beyond the end of lifetimes related to 1990 projects.

The Compliance boundaries have been extended to 2072, 50 years after the assumed beginning of the project lifetime in 2022. Compared with the 1990 projects, the 2022 curves begin with a noticeably steeper gradient, because during the intervening 32 years there has been a significant increase in the value of k, as can be seen on the left-hand chart in Figure 4.2. So although the cumulative probability

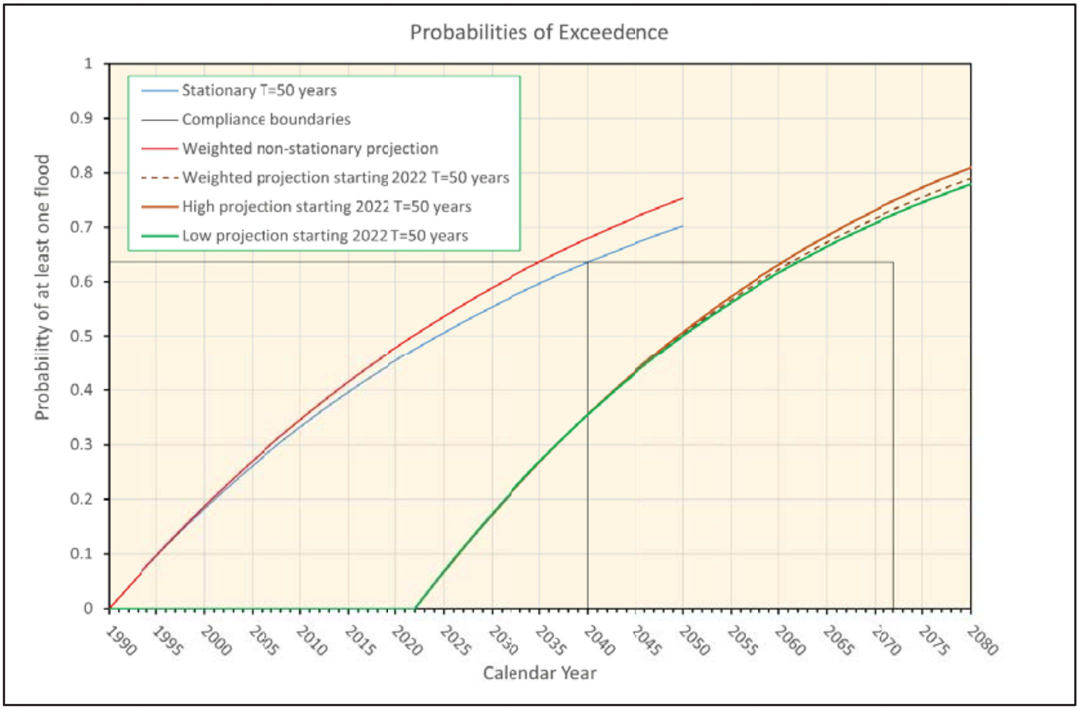

Figure 4.3 | Comparison of design lifetimes for projects put into service in 2022.

of at least one flood has been reset to zero, the *rate* at which flood probability increases begins more strongly as the initial value of *k* increases.

This has the effect of further shortening the project lifetime before the flood probability exceeds the threshold value of 63.6% discussed in Section 4.1.3. Now the High, Weighted and Low projections give 2061, 2062 and 2062 as the threshold years, corresponding with design lifetimes of 39, 40 and 40 years respectively. Instead of the five year reduction in project lifetime found for the weighted non-stationary projection beginning from 1990, the reduction is now 11, 10 and 10 years respectively.

This difference of only one year between 2022 projections establishes that the choice between 1990 and 2022 as a starting date has some five times as much influence on the project lifetime as the choice between more and less optimistic IPCC scenarios. This conclusion follows from the close match between the sample scenarios until 2040 (Figure 4.2, left chart), and should be checked against the application of the IPCC scenarios by a specialist climatologist. This should result in a replacement for the illustrative Table 4.2 entries by precipitation intensity data specific to the project locality.

4.3 | Final comment

The hypothesis in Section 4.1.1 postulates “an unchanged catchment”. Significant changes may be unlikely over short periods, but over longer periods modelling technology is well established (see Section 3.6, Chapter 3) to represent catchment changes under stationary climatic conditions. There is no reason why that developed technology cannot apply equally under non-stationary climatic conditions, so further details need not be discussed here.

4.4 | Acknowledgements

The citation of selected material from the NIWA report (Macara et al. (2019)) was approved by Dr Gavin Palmer, General Manager Operations, Otago Regional Council.

CHAPTER 5

Hydraulic model application

Alastair Barnett

HYDRA Software Ltd, New Zealand. E-mail: *barncon@xtra.co.nz*

5.1 | Computational Solution

5.1.1 | Channel geometry

The analytical models discussed in Chapter 2 become practical only when translated into computational solutions between external boundaries. As shown in Figure 2.1, channel reaches each require a series of n cross-sections to be surveyed, with the origin, orientation and level of each cross-section survey fixed in 3D to a suitable map grid. Usually, the best way to do this is to record the map location and datum level of both ends of each cross-section, trying to keep the survey line between them perpendicular to the segmented channel s axis along which 3D scalar longitudinal distances are measured. If this is not done, there will be no way to construct a reliable overlay of computational model results on gridded lidar surveys and georeferenced aerial photographs, such as that illustrated in Figure 5.1.

Accuracy of the model grid overlay is demonstrated (top right) by the realistic detailing of flood flows crossing the road centreline camber.

Chosen cross-sections must be *representative* so that automatic interpolation will not disguise local features. A reliable interpolation strategy between surveyed sections in an irregular channel is proposed in Figure 5.2. Note that no automatic interpolated link may cross the thalweg (in black) linking the deepest point in each section.

5.1.2 | The Solution Matrix

The core of a computational solution is the *solution matrix*. This is illustrated in Figure 5.3.

At both the upstream and downstream ends, either the discharge Q or the free surface height h must have values (alternatives marked in red) measured and supplied by the model user. The solution at the initial time t_1 is known (indicated in green). The predicted solution at time t_2 is indicated in black.

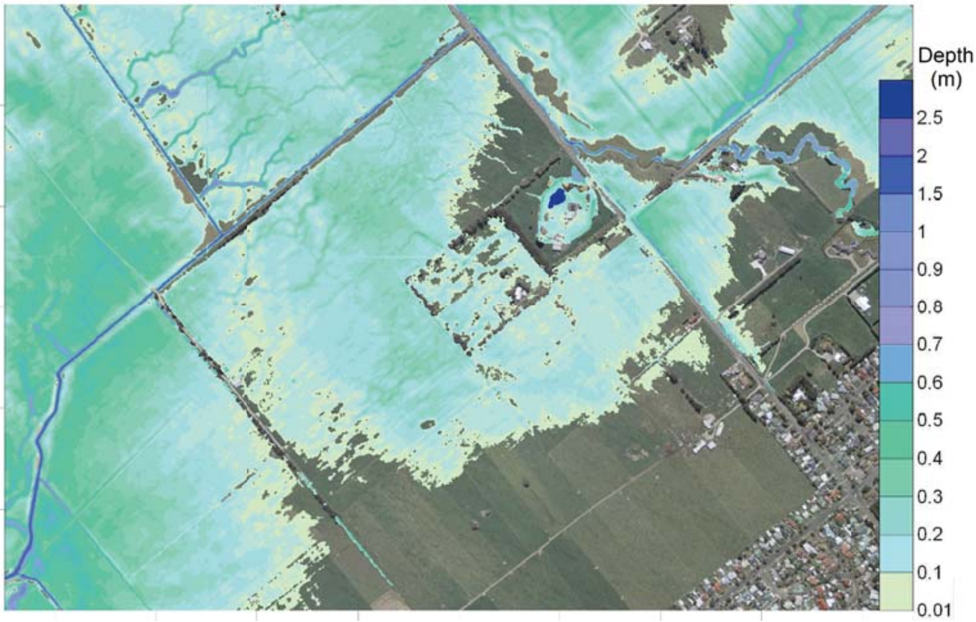

Figure 5.1 | 100 year flood through the floodway past the city of Palmerston North.

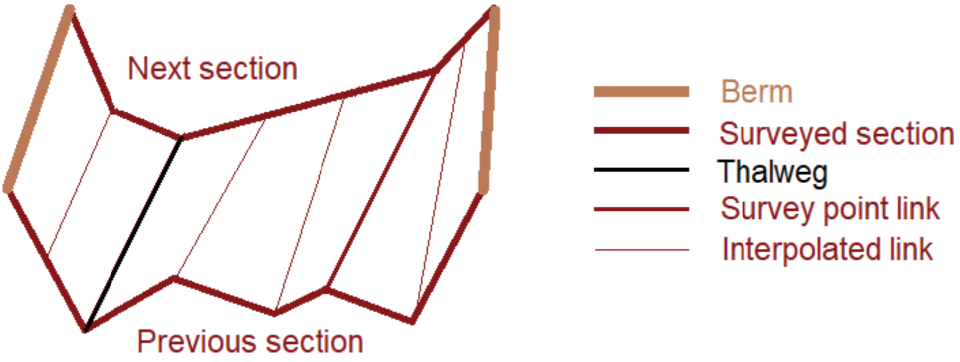

Figure 5.2 | Diagram of warped surface interpolation between irregular polygons.

As shown in Chapter 2, each of the $n-1$ cells between n successive sections can link the predicted variables by providing two equations: the volume conservation equation and the conveyance equation. This total of $2n-2$ equations should support the solution of the $2n-2$ black (predicted) variables. However a strategy is required to produce the black values one at a time from this type of matrix, and this is provided by the *double sweep matrix inversion* algorithm.

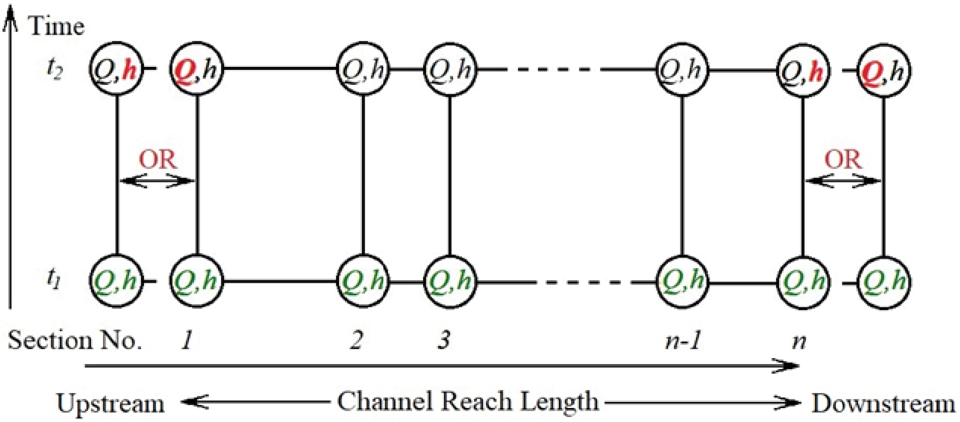

Figure 5.3 | Solution matrix for 3D scalar models.

This is an extremely efficient computational process, taking little more than the time required to update to the green Q and h values the coefficients in the two equations representing local conditions at time t_1 in each cell. As a result, 3D scalar solutions take orders of magnitude less time than vector solutions which deal with multidimensional matrices. Therefore such vector solutions should be reserved for use *only* when transverse effects require investigation, when the class of problems called “secondary flows” are of main interest. As Nezu (1994) put it, “Speaking roughly, the primary flow governs the shear stress and friction laws in rivers. Therefore, the discharge (flood) control and the associated sediment transport are mainly governed by the primary flow. On the other hand, the secondary currents govern various phenomena in the cross section and the spanwise motions.”

5.1.3 | Boundary Conditions

The upstream and downstream boundaries (see Figure 2.1) both require the values of either the discharge Q or the free surface height h to be provided from *outside* the model at all times from t_1 to t_2, the lifetime of the model. However the analytical integrals in Eq. (2.4) are now being replaced by numerical integration, which will fail if the boundary values at t_1 and t_2 do not represent all values at intermediate times. Values of t_1 and t_2 must now be updated in succession such that all significant changes of conditions are recognized. This requires location of the boundaries where some history is known about flow conditions during the model lifetime. A simple level recorder will provide a continuous history of surface levels at that site, which is all that is required if there are no plans to affect levels by changing the channel conveyance near that boundary.

Level gauging at both upstream and downstream ends is very cost effective provided flow gaugings at an intermediate point have been made during steady flows as recorded by both boundary level gauges. This enables head loss through the reach to be measured, allowing Q to be used to calibrate the resistance coefficient of the channel (usually expressed as Manning n).

Without such flow gauging records, no great accuracy of model predictions can be expected, although tables of Manning n values may be adequate for engineering materials such as HDPE pipes or concrete of various finishes if the channel has yet to be constructed, and is therefore not available for gauging. Even so, steady flow gauging is still then recommended to check design assumptions as soon as possible after the project has been implemented. Tables of roughness coefficients are widely used for natural channels, but may give flows in error by 30% or more in vegetation, as it is difficult to allow for the resistance offered by similar species, and variation between winter and spring conditions may be considerable. In such cases there is no substitute for steady flow gauging coupled with head loss measurements over channel reaches between tributary junctions.

The inspection of such reaches should record visually obvious local changes in bed material, and attempt some assessment of the roughness of the material in such locations *relative* to the predominant bed conditions in the reach. Because these estimates are made relative to the background resistance of the reach as a whole, they will still be corrected by the calibration, which is a different matter from plucking *absolute* roughness values out of tables in a manual without calibration. Another valid method of reducing the effort of calibration is to recognize a resemblance between uncalibrated reaches and calibrated reaches in adjacent catchments, where similar vegetation and bed material may be expected to offer similar resistance.

If the gauging site is near one of the boundary level recorders, then a discharge boundary should be considered, especially at the upstream end of the model (see Figures 5.4 and 5.5). There it is essential to ensure that the numerical boundary inflow repeats the physical inflow, as if the inflow is wrong, *every detail* of the whole model will be wrong.

In contrast, downstream boundaries have a more limited influence, because the model itself may include *controls* at which the influence of a downstream water level boundary goes no further upstream. Examples include weirs or overfalls, where the discharge is set *only* by upstream conditions.

Another example is a uniform channel, which gradually imposes a uniform flow relationship between Q and h based on the conveyance. This relationship requires a non-uniform flow transition, so will

Figure 5.4 | Flow gauging using dye dilution sampling at the upstream end of hydropower canal.

apply only in hydraulically “long” uniform channels (Henderson (1966)). Flow in steep channels is also governed *only* by the upstream boundary and the channel conveyance.

In all these cases, the downstream boundary is still required by the double sweep algorithm, but has no influence beyond the nearest control upstream, unless of course the downstream boundary level is set high enough to drown such features. A useful strategy to deal with a lack of available boundary data downstream of the model area of interest is therefore to introduce at the last available cross-section a fictitious channel control such as an overfall, dropping into a pool. A constant boundary surface level is then specified for that pool. This level may be arbitrary, as long as it is clearly below the waterfall crest. A drawdown profile will then be generated between the last two “real” cross-sections above the overfall. Upstream of those, a reliable downstream boundary condition will then exist for the remainder of the model.

Laboratory models also require boundary conditions to isolate them from the laboratory infrastructure, which has no parallel existence in the full scale prototype channels which are being simulated. As seen in Figure 5.5, a calibrated discharge from a large pump commonly forms the upstream boundary condition, with dissipative mats intended to create 2D distribution of uniform discharge across

Figure 5.5 | Calibrated pump outflow into upstream end of laboratory model.

the flume width. Downstream, an overfall into a calibrated pit performs the same function as the recommended fictitious overfall in the computational model, with laboratory sluice gates or adjustable weirs being used to raise the downstream water level if that is required for similarity with prototype downstream levels.

Discharge boundaries concurrently at *both* ends of the model should be avoided, because calibration errors will create mismatches in steady flows in and out of the channel, even though surface level recorders concurrently indicate no changes in level. This is particularly embarrassing if the whole solution suddenly ceases to exist, because a flow excess at the specified downstream boundary has drained the water in the model down *below* the level where the upstream inflow can be sustained as far as the downstream end. For the same reason, calibrated pumping directly from the downstream end of laboratory flume models is rarely attempted, because this may involve removing water at a faster rate than the intervening channel conveyance can deliver it. Some years ago, the rapid drawdown from this mistake in a hydropower scheme caused collapse of the intake channel walls, taking a large power station out of commission for several years!

As mentioned above, using level boundaries at both ends of the model is very cost effective once the Manning resistance has been calibrated, as the values of the discharge then follow immediately from the conveyance Eq. (2.13), and are provided automatically by the application of the double sweep algorithm. This approach weakens if the Manning resistance is found to vary significantly with Q, as hope for calibrating a single value of the Manning n for all water levels rests on lack of development of waves in bed sediments which may be mobilised at sufficiently high flood velocities.

5.1.4 | Initial Conditions

Initial conditions are most easily found for steady flow, as such flows are commonly observed, and there is no need to follow exactly the same series of boundary values at preceding times in order to recreate the exact values of discharge at all points. A single fixed boundary condition should be applied at each end of the model and maintained by recycling for as long as it takes for levels to settle to fixed values at each intervening part of the channel. However this procedure itself requires a physically valid solution as a primary initial condition, and the most accurate option is a hydrostatic solution, where *all* values of Q are zero and *all* values of h are a single constant. This primary surface level must be high enough to wet *all* sections in the channel (or network, if there are multiple channels in the model).

The boundary conditions (flow or level) will supply an initial value for each end of a single channel, or each unconnected end of a network, and initial levels will then have to be drawn down to equal these values, and then held while the drawdown proceeds to lower level values at other boundaries. Meanwhile the flow boundary values for the whole solution will have to be adjusted by transition at the relevant open ends. Slow transitions will always work, but in many cases the drawdown can safely be speeded up significantly by adopting a typical initial boundary flow as the primary flow for the whole network.

Finally, the solution must be left to run until steady state is reached in all channels.

5.2 | Reliability, robustness and convergence

Computational model applications are typically commissioned on the basis that results are to be produced in a limited time, making the best of inadequate available field data observations. In selecting the method of analysis, an applied model user therefore attaches high value to the *reliability* of the solution, so that the chosen method should not fail through instability or excessive run times, even though field data limitations often impose the concentration of validation data in a few areas. This leaves minimal data in large intervening regions, so ideally the preferred method should offer robust performance throughout a range of widely flexible grid spacing, both timewise and spacewise.

In practice, the first generation of solution methods suffered from problems with instability and inconsistency – see Abbott (1979) – so solution reliability demanded a considerable background in numerical analysis from the model user, with corresponding constraints, particularly the Courant limitation on the explicit time step used. These constraints were eased by the introduction of implicit solution methods which were first thought to be unconditionally stable. However, Barnett (1974) showed that the claimed unconditional stability was valid only for pure initial value problems, as the addition of boundary conditions produced stability limitations related to the Froude Number, applying particularly with Courant Numbers less than unity. Further, in practice, implicit schemes were then found to be unreliable through susceptibility to phase errors (Cunge et al. 1980).

According to finite difference analysis, second order schemes are theoretically superior to first order schemes but if shocks developed in the solution, oscillations in the vicinity then appeared with such higher order schemes, tending to corrupt the solution. Subsequent methods of dealing with such oscillations were discussed by Garcia-Navarro & Burguete (2006), but unfortunately, shock capturing approaches such as the Lax-Wendroff scheme return to an explicit formulation, which reintroduces the unwanted Courant limitation on the time step used. Upwinding schemes were also introduced to the discussion, but generally, attempts to make these implicit seem to have been seen as too difficult for general application. In the discussion, several schemes were compared with an exact analytical solution of a dambreak problem, and the 'excessive numerical diffusion introduced by the first order central scheme and the lack of robustness of the second order scheme are shown'. The writers then comment 'Roe's scheme, being only first order, is very well suited' for this kind of problem.

In short, the authors make clear that second order schemes do not necessarily produce more reliable solutions than first order schemes, contrary to the conclusion suggested by finite difference analysis. Further, use of these more advanced schemes seems in practice to require the sacrifice of relative freedom from time step size restrictions enjoyed by implicit schemes. As noted above, this becomes a major disadvantage in many practical applications of computational solutions.

Reliability is a rather subjective term, but an objective measure of reliability can be developed by introducing solution *robustness*, defined as the assessable property of continuing to provide a fair approximation to a solution even if grid spacing and Courant Numbers are allowed to vary by orders of magnitude. Barnett (2012) linked solution robustness to the rate of convergence of a scheme, which was shown to vary greatly between alternative widely used schemes. Admittedly a 'fair approximation' still has a subjective element based on the judgement of the analyst, but at least it absolutely excludes solutions which fail to run to completion through termination by instability. If a solution is obtained, then assessment of a 'fair approximation' should also take into account model uncertainty, of which a good overview is provided by Samuels (2006). This is of great importance, as the validity of computational solution techniques is often demonstrated under ideal academic conditions: fine grid discretisation at equally spaced steps.

In physically based applied models the reality is different, as applied users attach high value to reduction of solution time, and flexibility in grid spacing. Under these conditions, some solutions are robust, performing with minimal loss of accuracy compared with ideal conditions, while others will collapse and report solution failure.

Convergence is the ability of a solution to reach and maintain a final value under successive grid refinements, and widely accepted theory states that all schemes have this property subject to requirements of stability and consistency. This implies that all convergent schemes should ultimately produce the same solution. However, robust schemes will approach this ultimate solution at grid spacings much coarser than those of other schemes.

5.3 | Channel roughness

5.3.1 | Conveyance

The parameter "Manning *n*" was introduced in Eq. (2.13) in Chapter 2. Taking this together with Eq. (2.12), the definition of the "friction slope" S_f can be written

$$S_f = \frac{Q\,|Q|\,n^2 P^{4/3}}{M^2 A^{10/3}} \qquad 5.1$$

Here M is a (dimensioned) constant, while the area A and wetted perimeter P are a matter of geometry, obtained for a given h directly from surveyed sections, or from Figure 5.2 if interpolation is necessary. On the other hand, n must be obtained by *calibration* at the section, preferably from situations of steady flow where both Q and h have been measured directly in the field (see Section 5.1.3). Once n has been defined by gauging over a range of steady discharges, it may be used in Eq. (5.1) either to determine the value of Q if S_f is known (h boundary supplied) or the value of S_f if Q is known (Q boundary supplied).

For example, an excellent example of careful calibration was reported by Wormleaton and Merrett (1990). This used results measured in a large flume at the SERC-FCF at Wallingford, U.K. to assess the performance of several standard discharge calculation methods. One series of tests involved a simple trapezoidal channel. The results for discharge vs depth in that series are plotted in Figure 5.6.

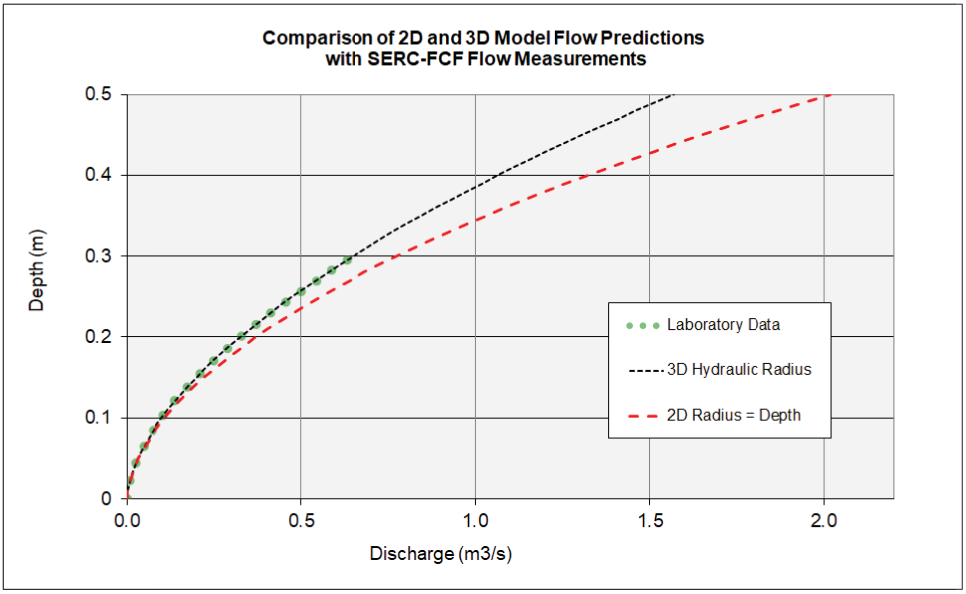

Figure 5.6 | Discrepancy between channel resistance formulations in 2D vector and 3D scalar models.

As discussed by Barnett (2015), the black fine dashed line for “3D Hydraulic Radius” with a constant Manning *n* of 0.010 almost exactly overlays the green dotted line for “Laboratory Data”. In contrast, no wetted perimeter measurement is available in 2D vector models, so the usual 2D simplification is to approximate the hydraulic radius *R* with depth. This may seem reasonable in the SERC-FCF channel, which has a base width of 1.5 m and maximum depth of 0.3 m with 1:1 side slopes, but only at depths below 0.1 m are the errors not significant.

In contrast, at a depth of 0.5 m, the result of applying the simplified hydraulic radius (red dashed line) is a 2D model discharge estimate almost 30% above the reported experimental discharge curve as extrapolated to 0.5 m.

This discrepancy can be explained by reference to Figure 5.7. Here the SERC test trapezoidal section has been plotted to scale, and the added area for every 0.1 m of depth compared with the added perimeter, using wetted perimeter = area/depth in accordance with the stated 2D vector model simplification. Between depths of 0.4 m and 0.5 m, there is a considerable area expansion (identified by the pale yellow fill) but at a depth of 0.5 m the simplified perimeter estimate (marked by bright yellow) does not even reach the true perimeter corresponding with a depth of 0.2 m (marked by the top of the pale blue fill).

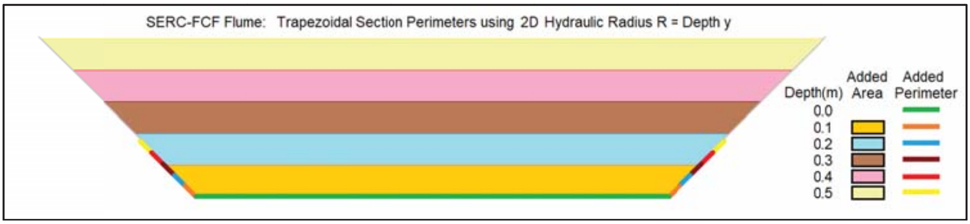

Figure 5.7 | Increasing discrepancy between section depth and wetted perimeter as depth increases.

As shown in Figure 5.6, the 2D simplification computes the channel has a flow capacity 20% above that measured at a depth of 0.3 m, and this flow capacity overestimate increases to almost 30% at a depth of 0.5 m. As demonstrated in Barnett (2015), typical relationships between conveyance overestimation and design storm return periods suggest a channel designed for capacity at a 100 year return period would then actually fail to convey floods of a 30 year return period at a depth of 0.3 m, while at a design depth of 0.5 m, overflow failure would occur at a return period of under 20 years, or during about five floods every 100 years!

5.3.2 | Conveyance in channels of composite roughness

A difficulty arises when flow resistance in some parts of a section appears markedly different from that in other parts. Adoption of at least two kinds of roughness characteristics is indicated, but how can those be weighted for proper conveyance representation across the section, and what calibration procedure should be followed for each of the roughness values? An example is presented in Figure 5.8.

Here the berms on each side are dominated by land vegetation, which can withstand occasional flood inundation, while the central low flow channel will be dominated by sediment roughness, sometimes supporting aquatic weed growth. Henderson (1966) recommended that the conveyance of channel sections laterally divided into subsections should be treated on the basis that the energy slope S_f would be equal through each subsection, assuming any energy surpluses or deficits would be rebalanced by a redistribution of the total discharge through any subsections of sections defined further downstream. According to Eq. (2.12), this would mean the conveyances of each subsection would sum to the total section conveyance K.

According to Chow (1959) the Lotter formula followed this idea, with the following result:

$$n = \frac{PR^{5/3}}{\sum_1^N \left(\frac{P_N R_N^{5/3}}{n_N} \right)} \qquad 5.2$$

Figure 5.8 | Example of a channel with zones of significantly different roughness.

Here *n* represents the whole section, so that it can be calibrated directly against steady flow field data. P is the wetted perimeter as before, $R = A/P$ where A is the area as before, and the subscript N refers to the Nth subsection. This formula is frequently quoted, but unfortunately it cannot be recommended, because Lotter's derivation assumes that

$$A\frac{A^{2/3}}{P^{2/3}} = PR^{5/3} = \sum_{i=1}^{N}\left(P_i R_i^{5/3}\right) = \sum_{i=1}^{N}\left(A_i \frac{A_i^{2/3}}{P_i^{2/3}}\right) \qquad 5.3$$

While A is known to equal ΣA_i and P equals ΣP_i it is easy to demonstrate by trial that in general, this equation is true *only* when $N = 1$. Worse, if the *n* value for any of the subsections is increased with the intention of decreasing the conveyance of the whole section, the result is often an *increase* in section conveyance, as demonstrated by Barnett (2002).

If this method is applied, calibration will be very difficult, as whether an adjustment intended to increase resistance actually does so rather than having no effect or actually *decreasing* resistance becomes a matter of trial and error, leading to tedious iterations which may not converge. Calibrating more than one Manning *n*, as proposed by Lotter, in a section past which only *one* value of friction slope is measurable causes further problems.

A commonly used approach is to consult published tables of Manning n values, but this method is notoriously unreliable for all but controlled manufactured surfaces such as HDPE in pipes, while values in crops or in natural growth such as scrub cover may err by 20% or more, depending on factors such as the growth season.

The 2002 paper recommended an approach which is both more certain and faster, introducing r values defining each roughness with a value *relative* to a single local standard value n_s of the Manning n (see Section 5.1.3). In these circumstances the whole section Manning $n = rn_s$ which may still be calibrated with high accuracy if measured friction slope data is available, even where the roughness of (say) grassland relative to forest may be considerably in error. Once a fair calibration has been achieved, the significance of such relative errors may be investigated by sensitivity analysis if an improved calibration fit is seen as important. The proposed correction for the Lotter formula Eq. (5.2) was (see Barnett (2002)):

$$r = \frac{\sum_{i=1}^{N}\left(A_i R_i^{2/3}\right)}{\sum_{i=1}^{N}\left(A_i R_i^{2/3}/r_i\right)} \tag{5.4}$$

Here for the whole section, $r = n/n_s$ and for the ith subsection $r_i = n_i/n_s$. By inspection, an increase in *any* of the r_i values can *only* increase the value of r for the whole section. Similarly a decrease in *any* of the r_i values can *only* decrease the value of r for the whole section, allowing calibration corrections to be made with confidence in the outcome. This deficiency in the Lotter formula has therefore been removed.

Care must still be taken to distinguish between section subdivision for resistance calibration and section subdivision by survey, as the polygons in Figure 5.2 are purely based on survey decisions aimed at accurate representation of cross-section geometry. Based on the principle that simple subdivision of a channel of uniform Manning n (that is, all $r_i = r$) should not affect the value obtained by Eq. (5.4), the same principle should apply to subdivision of a *subsection* of uniform Manning n. In other words, if the ith subsection has uniform boundary roughness but is subdivided into J parts by survey geometry, then

$$A_i R_i^{2/3} = \frac{\left(\sum_{j=1}^{J} A_j\right)^{5/3}}{\left(\sum_{j=1}^{J} P_j\right)^{2/3}} \tag{5.5}$$

While there is now a value for r available for each cross-section, a practical computational issue remains that a different value of r will have to be found from Eq. (5.4) for every water surface level in a solution supporting composite roughness of this kind. Fortunately, the same problem applies to the evaluation of P, and this is done most efficiently by a tabular look-up function prepared in advance of the actual model run. As the wetted perimeter in a segmented polygon is a linear function of depth, the exact value can be computed each time by linear interpolation between table entries. The 2002 paper shows how the wetted perimeter can be rescaled by reference to Eq. (5.1) to give

$$n^2 P^{4/3} = n_s^2 r^2 P^{4/3} = \left(n_s r P^{2/3}\right)^2$$

And so

$$P' = r^{3/2} P \tag{5.6}$$

Here P' is the rescaled wetted perimeter, which can be set up at the beginning of run time to incorporate the value of r without extra table storage. This also offers the pleasing physical interpretation of the wetted perimeter as corrugated, with the height of the corrugations increasing to provide the increase in P' corresponding with an increase in roughness.

5.4 | Hydraulic jumps

5.4.1 | Jump conditions

As mentioned in Chapter 2, shock waves may appear under certain conditions where differential analysis using Taylor series expansion is no longer justifiable by an assumption of continuity. In such cases the integral form of the conservation laws should be applied. As shown previously (Chapter 2, Section 2.4.3), if it is not practical to model in detail the normal stresses associated with fixed irregularities in the channel wall and bed, energy (scalar) modelling has a strong accuracy advantage over momentum (vector) modelling because such stresses do no work and therefore play no part in energy balances.

However in pure hydraulic jump analysis, the normal stresses are not complicated by irregular bed features, so a momentum balance through the jump should be accurate, at least to a first approximation. At the same time, as pointed out by Abbott (1979), the discontinuity causes flow to pass into a less ordered state in which internal energy and turbulent energy may be expected to increase at the expense of the initial highly ordered mechanical energy. Figure 5.9 illustrates this transfer from order (foreground) to disorder (background) through a hydraulic jump almost 1m high passing along a canal. This jump was generated by a trial dambreak event created by sudden full opening of upstream control gates (right background) within a few seconds.

Figure 5.9 | Controlled dambreak hydraulic jump passing along a power canal.

5.4.2 | Bresse analysis

With manual computation still normal practice when defined by Chow (1959) and Henderson (1966), the assumption of hydrostatic conditions favoured energy balances for general use. The treatment of the piezometric head, which is constant over a cross-section, was simpler than computing the pressure, which increases linearly with depth. However as computational hydraulics entered the scene, computation of unsteady flow became more practical, and two prominent new textbooks recommended momentum analysis for general use.

Abbott (1979) based his argument on the second law of thermodynamics, in which "as a discontinuity appears, so momentum and energy are no longer equivalent concepts…and their equations produce different answers." Cunge, Holly and Verwey (1980) stated "Since the mass-momentum couple of conservation laws is applicable to both discontinuous and continuous situations while the mass-energy couple is not, as described by Abbott, we shall base our derivations on mass-momentum conservation."

These discussions drew on the pioneering work of Bresse (1860), who produced a widely quoted analysis which predicts energy "loss" through a hydraulic jump in terms of flow dimensions upstream and downstream of the jump. Henderson (1966) presents this classical analysis in a discussion comparing the application in steady flow of both energy and momentum principles. The result for the shock loss in a wide rectangular (2D) channel is

$$\frac{E_1 - E_2}{y_1} = \frac{(a-1)^3}{4a}$$

where the subscripts 1 and 2 refer to cross-sections, respectively upstream and downstream of a hydraulic jump in a channel. Note that unlike in Figure 5.9, the jump of the Bresse analysis is stationary, with upstream level *below* downstream level. E is the energy above the channel bed, y is the height of the water surface above the channel bed, and a is the ratio y_2/y_1.

This 2D scalar formula was generalized to 3D scalar form by Barnett (2022) as follows:

$$\frac{B}{A_1}(H_1 - H_2) = \frac{(a-1)^3}{4a} \tag{5.7}$$

where a is now the *area* ratio A_2/A_1, and A is cross-sectional area as before. B is the free surface width at the jump discontinuity, and E has been replaced by H, the energy head above datum. According to Henderson (1966)

$$H = h + \frac{Q^2}{2gA^2} \tag{5.8}$$

Eq. (5.8) is not strictly accurate with respect to kinetic energy, so attempts may be made to correct the total kinetic energy flux passing through the section by introducing the Coriolis coefficient α. However, when it is recalled that H normally appears in an energy flux *difference* (as in Eq. (5.7), insignificant gain in accuracy (Barnett (2017)) can usually be expected to reward efforts to evaluate this rather inaccessible coefficient.

Across a section, h is often taken as a constant height of a level water surface above datum. However, if the hydrostatic pressure distribution is applied below a water surface e above datum, with e varying across the channel, there are advantages to defining a mean h by

$$h = \frac{\int_0^B e\, db}{B} \tag{5.9}$$

where b is a transverse distance measured from some point at one side of the cross-section.

This has the benefit of extending models to cases of channel curvature where superelevation is required to carry parallel flow around a change in direction. If available gauging equipment is not capable of measuring the actual variation of e, then recourse can be had to superelevation models such as those discussed by Chow and Henderson.

The energy loss equation through the jump was then derived as

$$H_1 - H_2 = (h_1 - h_2)\left\{1 - \frac{(a+1)^2}{4a}\right\} \tag{5.10}$$

For $a > 1$ (depth at Section 2 $>$ depth at Section 1), the value in braces is always negative, and the water level h will be less at Section 1 than at Section 2. There will then be a loss of mechanical energy head H between Section 1 and Section 2, known as a *shock loss*.

5.4.3 | Friction effects

Chow (1959) discusses the analysis of such a jump in a horizontal channel, claiming that the external forces of friction are negligible, because “the jump takes place in a relatively short distance”.

However, it turns out that friction can account for a significant part of the loss, and possibly all of it if the bed is sufficiently rough. In this case the jump should disappear, and indeed support for this hypothesis is provided by other sections of Chow’s book, where he comments “the hydraulic jump can be eliminated if the energy loss can be dissipated gradually and smoothly. This can be done by introducing proper roughness in the transition, for instance, by bolting cross timbers to the bottom of the transition.” Elsewhere in reference to “an objectionable hydraulic jump” inside a tunnel, he notes “the hydraulic jump was finally eliminated by bolting cross timbers to the channel bottom, thus increasing the friction”,

Chow reports laboratory investigations of finite lengths of hydraulic jumps, by many hydraulicians in institutes in Berlin, Zurich, Russia, New York, California, and particularly in the USBR (US Bureau of Reclamation). A consensus developed that the jump length was a linear function of the downstream depth, which translates to A_2/B in the 3D scalar energy loss equation (5.11). This relationship can be written as

$$L = m\frac{A_2}{B}$$

where L is the finite distance between the beginning and end of the jump length, and m is the coefficient of proportionality. The reported consensus found m generally had a value of about 6, falling below 4 only with weak jump values of a below 2.

Laboratory reports also indicated that near the bed, the velocities at Section 1 persisted in a jet reaching as far as Section 2, suggesting that bed resistance effects would be comparable throughout L. Resistance losses can therefore be approximated by

$$H_1 - H_2 = S_{f1}L = S_{f1}m\frac{A_2}{B} \qquad 5.11$$

where S_{f1} is the “friction slope” at Section 1. The friction slope is usually evaluated by empirical methods based on the Chézy and Manning formulae, see Chapter 2.

5.4.4 | Validity ratio

Which is greater, the shock losses of Equation (5.10) or the resistance losses calculated using Eq. (5.11)? This has strong bearing on the occurrence of flow discontinuities, as if resistance losses can connect the water levels at Sections 1 and 2 smoothly without a jump, there will be no mechanism to convert ordered flow to disordered flow.

As Abbott (1979) points out, without such a mechanism, there will be no shock loss, flow transitions will follow normal rules of resistance losses, and standard energy modelling will continue to be valid.

Therefore a validity ratio can be introduced (Barnett, 2022) as

$$N_V = \frac{\textit{Resistance Loss}}{\textit{Shock Loss}} = \frac{4a^2}{(a-1)^3} S_{f1} m \qquad 5.12$$

The energy model validity condition $Nv > 1$ then translates to

$$n > \sqrt{\frac{1}{(a+1)}\left(\frac{a-1}{a}\right)^3} K_f R_1^{1/6} \qquad 5.13$$

where

$$K_f = \sqrt{\frac{B}{2gmP}} M \qquad \approx 0.09$$

K_f has the dimension $\mathrm{m}^{-1/6}$, and all these factors within K_f are known to be approximately constant. Therefore K_f can be treated as a constant, but best rounded off to a precision of only one significant figure. The suggested value of 0.09 corresponds with g having the value 9.81 ms^{-2}, M being 1.00 $\mathrm{m}^{1/3}\mathrm{s}^{-1}$ by definition, m taken as 6.0, and B/P chosen from typical rectangular channel values to have the necessary rounding value of 0.955. If better precision is supported by accurate physical measurements in a particular case, the full formula for K_f should be applied. This provides analytical proof of the observation by Chow that an increase in Manning n can eliminate a hydraulic jump and the corresponding change from ordered parallel flow to disordered flow. Therefore smooth transitions between supercritical and subcritical flow conditions can be arranged above a specific threshold of bed roughness. This finding should apply as much to numerical models and laboratory models as to Chow's quoted applications at full scale.

5.4.5 | Sample results

To illustrate likely values for the threshold ($N_V = 1$) Manning n obtained from the validity condition Eq. (5.13), Table 5.1 presents results (based on $K_f = 0.09$) for variation of $R_1 (= A_1/P)$ and a (or the Froude Number Fr_1).

Table 5.1 | Minimum values of Manning n to dissipate a stationary hydraulic jump

Fr_1	1.369	1.732	2.449	3.162	3.873
a $R_1 (m)$	**1.5**	**2.0**	**3.0**	**4.0**	**5.0**
0.037	0.0064	0.0106	0.0141	0.0151	0.0152
0.125	0.0078	0.0130	0.0173	0.0185	0.0186
1.0	0.0110	0.0184	0.0245	0.0261	0.0263
8.0	0.0156	0.0260	0.0346	0.0369	0.0372
27.0	0.0191	0.0319	0.0424	0.0452	0.0456

In this context, Fr_1 is defined - see Barnett (2022) - by the properties of a stationary hydraulic jump as

$$Fr_1 = \sqrt{\frac{a}{2}(a+1)} \tag{5.14}$$

Note the lack of need to continue increasing the Manning n with Froude Number, as illustrated by comparing the columns for $a = 4$ and $a = 5$. In fact, Eq. (5.12) predicts that the required Manning n actually *reduces* at any higher Froude Numbers, as the Manning formula rapidly increases the friction with higher incoming velocities.

Reliance on the validity condition (5.13) is encouraged by a comparison with a lengthy illustrated discussion by Henderson (1966) in his textbook. He demonstrated in the laboratory that at a Froude Number of 1.55 and a flow depth comparable with the 0.037 m in Row 1, merely roughening the flume bed with sandpaper was enough to change the jump from a broken discontinuity to an undular form in which surplus energy is transmitted downstream but without any vector change in direction. With the original smooth bed of the glass flume unlikely to exceed 0.010 as a Manning n value, this 60 year-old experiment supports the predicted transition point.

With a hydraulic radius of only 37 mm at Section 5.1, Row 1 should apply to laboratory model and water supply scales, while the Row 2 hydraulic radius of 125 mm should illustrate typical results for stormwater modelling. With a Manning n for unfinished concrete commonly around 0.014, there should be little need to switch to vector modelling for Froude Numbers up to 2 at these scales.

At supercritical scales of 1 m for R_1 in Row 3, typical of civil engineering channels for culverts, irrigation and small hydro canals, use of concrete will require deliberate roughening with coarse aggregate or masonry to eliminate hydraulic jumps. Row 4 at depth scales of 8 m is associated with major hydro canals or large rivers, where the existing Manning n from natural channel sediment should be calibrated, as it may prove to be sufficiently rough. Finally, Row 5 covers depth scales of 27 m, which apply only to the largest shipping canals or approach channels to major ports. Normally, supercritical flow will be encountered in such channels only during major river floods or tsunami action, and even then for Froude Numbers up to 2 the natural sediment may be sufficiently rough.

Note there are incentives to roughen the channel in both infrastructure channels and their numerical models, but for different reasons. Wandering hydraulic jumps are generally to be avoided in infrastructure, as illustrated by the examples cited by Chow. In numerical modelling, the incentive is to continue using energy modelling at all scales because of the simplicity and relative solution accuracy of 3D scalar modelling compared with vector modelling. In short, 3D scalar modelling should be able to be used without concern about *stationary* flow discontinuities in most engineering infrastructure studies. Such hydraulic jumps are normally associated with flow near sudden changes of gradient from steep to mild slopes.

However, for moving hydraulic jumps such as those generated by tsunami or extreme upstream flood action, the lower depth Froude Number Fr_1 *relative to the jump* may be in the range covered by Table 5.1 without any significant associated bed resistance losses. For example, the water was almost static in front of the jump shown in Figure 5.9, and in such cases the Validity Ratio N_V from Eq. (5.12) will be well below 1.

This supports the experience of success with momentum vector (usually 2D) modelling by practitioners working with coastal and harbour problems. There sudden changes of channel gradient are usually drowned by boundary levels, so the important hydraulic jumps are generally those moving rapidly as bores or surge fronts. Also (for typical values of Manning n) bed resistance is less likely to suppress jump formation because depth scales are consistent with the lowest row in Table 5.1.

It has been unfortunate that this successful coastal modelling experience has led to an unthinking transfer of 2D momentum (vector) modelling into areas such as shallow overland flow, where the validity thresholds from the top rows of Table 5.1 predict that energy (scalar) modelling would have given results of superior accuracy.

5.5 | Long term simulation

5.5.1 | Context

Estimation of the long term statistical probability (or return period) of extreme events is contentious where stationarity of conditions governing those events obviously cannot be assumed, either throughout the "training period" of a model calibration or for extrapolation into future projections. Non-stationary hydraulic influences fall into three main categories:

(a) Climate change, which is projected to increase the frequency of severe floods as well as raising sea levels.

(b) Planned infrastructure changes related to economic development. Significant hydraulic examples have been flood management schemes, progressive urban intensification and the resulting expansion of stormwater drainage capacity, construction of new hydropower generating capacity, and irrigation scheme development.

(c) Planned infrastructure changes *in response to* climate change. The economics of existing development in category (b) will have to be re-evaluated. To cope with increasing electrification of transport, hydropower will need a new emphasis on pumped storage reservoirs to firm new large scale intermittent power generation from sunlight or wind. The raising of embankments to cope with increased flood levels along major waterways will create severe local flooding problems outside the banks (see Figure 5.10) along minor tributary waterways which are no longer able to rely on gravity drainage for the duration of the elevated main river levels.

Long term continuous simulation is attractive for hydraulic systems, as in principle this is able to retain the historical natural variation in upstream boundary input (usually weather related, especially

Figure 5.10 | Local flooding (background) outside embankments controlling a major river flood (foreground).

rainfall) and downstream boundary input (typically water levels under gravity outflow conditions) while incorporating a deterministic interpretation of various projections of climate and infrastructure changes.

The statistical probability of natural events then remains the same in the numerical model as in the original system, but their severity of outcome may be aggravated or mitigated by the projected scenarios. Hence their ranking relative to other events may change, with important planning consequences.

Future infrastructure developments cannot strictly be treated by deterministic methods, but it is standard practice to reduce the number of alternatives to a few projections, each of which can be seen as deterministic. This procedure has been followed, for example, by the IPCC in simplifying their sea level rise projections to a few scenarios, each presented with a commentary on the assumptions made.

Given the advantages of a capability to separate probabilistic and deterministic aspects of planning projections, the obvious question arises “Why is long term simulation not more widely used?” The answer is the considerable remaining practical difficulty of aspects of long term simulation technology. This chapter explores solutions to some of the problems.

5.5.2 | Solution reliability

The term “solution reliability” is introduced, meaning the ability of a computational algorithm to survive all possible failure mechanisms, alone or in combination, and to complete any solution assignment, in all but exceptional circumstances.

For long term simulation, conditions must be changing with time, usually in some nonlinear way, which immediately introduces the need for a time stepping solution as discussed in Section 5.1.3. This must be linear in structure if it is using matrix solution analysis. Where flow problems are quasi-linear, meaning changes in the variables will also cause changes in the coefficients multiplying the variables, a generally acceptable approach is to treat the coefficients as constant to calculate a locally linear solution over a single time step. The process is then repeated, updating the linear coefficients every time step. The difficulty with this procedure is that, while it may demonstrably work under a wide range of trial conditions, this can never guarantee that some tiny loopholes in the solution domain cannot exist, through which in exceptional cases the coefficients may change at an unstable rate, causing solution failure.

Strictly, routine linearization is valid only if the variation per time step is an order of magnitude smaller than the dependent variable (e.g. flow, cross-section area). However, in hydraulic problems step changes of any size are theoretically possible, so simply refining the time step will not always produce the desired conditions. At the same time, there is pressure to maintain time steps as large as possible to speed up the computations. Considerable subtlety is therefore required in algorithmic design if a very large range of potential combinations of factors are to be managed without failure. In the 1990s, a failure rate was achieved of the order of one in a million applications of the same algorithmic logic at a computational point (a spatial grid point at one time step), and this was adequate for ordinary simulation problems.

However for long term simulations, such a failure rate is quite unsustainable, as this would require a modeller to intervene and diagnose a problem hundreds or even thousands of times to complete a single run! For example, Figure 5.11 plots a flow solution (Barnett (2010)) over 26 years in the Kleine Emme River in Switzerland. This model incorporated 570 cross-sections over a reach of approximately 23 km, so at 10 minute time steps this involved $570 \times 26 \times 365 \times 24 \times 6 = 0.78$ Billion computational points.

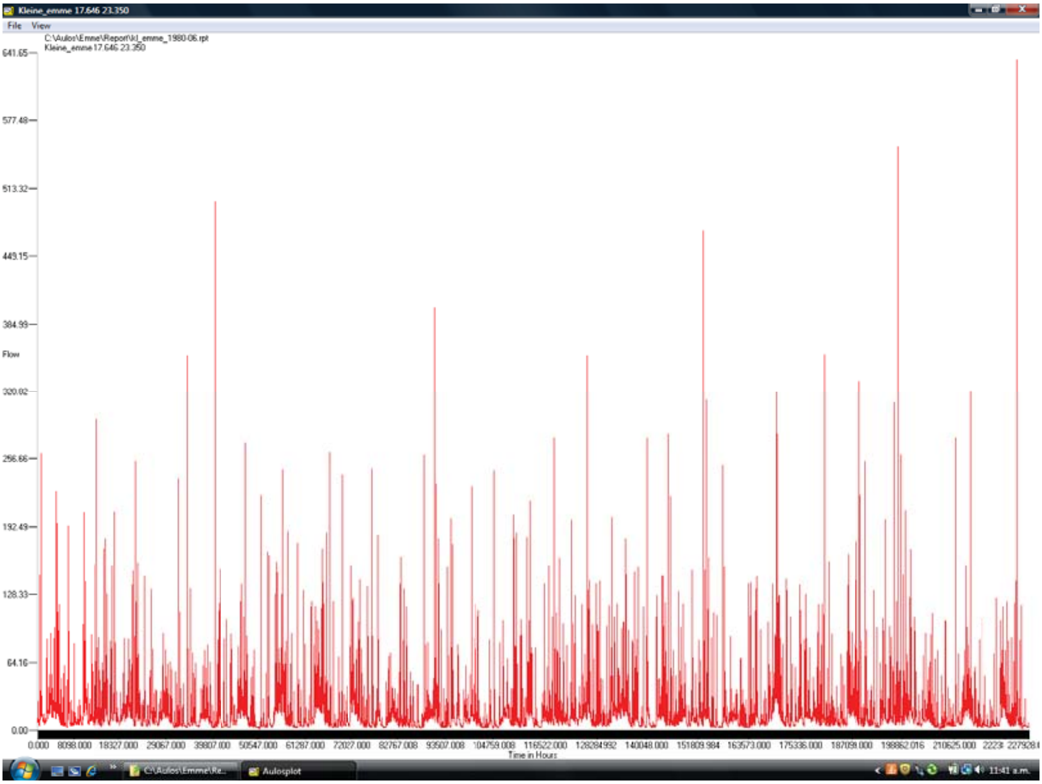

Figure 5.11 | Discharge hydrograph computed for a model of 570 cross-sections over 26 years.

Using the 3D scalar *AULOS* technology described here, fault diagnosis was required for only one point in the simulation, meaning a failure rate of approximately once per Billion computation points was achieved. On this basis, the solution reliability can be rated as acceptable for simulations of this kind. In the Kleine Emme example, upstream boundary inflow variation was extreme, with a maximum/minimum discharge ratio being of the order of 1000:1, but the full simulation was still found to be feasible at practical time steps.

5.5.3 | Data analysis constraints

Until recent years, long term simulation has been limited by hardware computing constraints. For multi-year runs, computation times can become prohibitively long, especially when a range of alternative deterministic scenarios is to be modelled over the full period. In a modern modelling practice, individual scenario runs should be kept under 1 hour on standard desktop computing equipment for assessment of a useful range of scenarios to be feasible, so a computation speed of around 1 model year/minute is desirable.

This is now becoming practical, as the 26 year model run discussed above took about 45 minutes on a modest 3GHz laptop, and many models will be smaller than 570 cross-sections. Also run times can be further reduced by the application of variable time steps, so that uneventful periods can be simulated using time steps of hours rather than minutes.

Long term simulations produce very large result files – the Kleine Emme example saved results only every hour, but even so the file grew to over 1 GByte, with 227,928 hourly results. Windows utilities will cut and paste files of this size, but use of standard spreadsheets for plotting is not yet possible with hundreds of thousands of rows. The earlier Windows Excel had a limit of 65,536 rows, while the extended 2007 Excel accepted larger time series, but seemed unable to produce plots from more than 32,000 rows.

A freeview package ©HYDRA Software Ltd (2023) is available to preview the full range of results, and was used to prepare Figure 5.11. The Golden Software®Grapher^{TM} package was also tested, and successfully produced plots of the full time series.

5.6 | Conclusions

Five practical aspects of the choice between scalar mass-energy analysis and vector mass-momentum analysis all favour energy analysis for flow depths less than 10m:

1. Computation based on the 3D scalar mass-energy couple requires the solution of only two simultaneous equations, a far less computationally demanding task than solving the four simultaneous equations produced by the 3D vector mass-momentum couple.
2. Further simplification is available with mass-energy in channels with irregular non-prismatic fixed beds, such as that shown in Figure 5.1. Since no work is done by forces normal to a fixed bed, the effect of normal forces on energy balances need not be considered, while shear effects can be accounted for by well-tried semi-empirical methods such as the Chézy and Manning formulae.
3. Both the Chézy and Manning description of shear resistance depend on measurement of the wetted perimeter. This poses no problem with the scalar mass-energy couple, but accurate *vector* treatments of the components of this measurement are yet to be invented.
4. Occurrences of truly discontinuous flows are too rare to base a general modelling strategy around them. Even where hydraulic jumps occur, their appearance in a numerical solution should be a flag for analysts to isolate them for consideration of their importance. Only if the model objectives require high accuracy in the height and movement of such jumps should momentum-based techniques be introduced locally.
5. In hydropower design, *energy* is the water property of main interest.

Therefore re-examination is justified of attempts since 1980 to adopt mass-momentum analysis (as generally applied in the drowned landscapes of coastal waters) to replace mass-energy analysis as the primary approach to channel hydraulics. Relativistic arguments suggest that the two approaches are complementary, and that hydraulic modelling would be greatly weakened if the regular application of *both* energy and momentum conservation principles was abandoned.

5.7 | Acknowledgements

Permission to publish photographs and graphic images is acknowledged as follows:

Figure 5.1, 5.2, 5.3, 5.4, 5.6, 5.7, 5.8, 5.9, 5.11: HYDRA Software Ltd

Figure 5.5: Lincoln University (D. J. Painter, S. L. Watkins)

Figure 5.10: Marlborough District Council

Figure 5.11: The Kleine Emme model was a joint study with Hunziker, Zarn & Partner AG, Aarau, Switzerland

CHAPTER 6

Japanese practice on tsunami mitigation

Anawat Suppasri, Kwanchai Pakoksung and Fumihiko Imamura
International Research Institute of Disaster Science, Tohoku University, Japan.
E-mail: *suppasri@irides.tohoku.ac.jp, pakoksung@irides.tohoku.ac.jp, imamura@irides.tohoku.ac.jp*

6.1 | Introduction

This chapter summarizes an engineering perspective on tsunami mitigation activities in Japan. Section 6.2 introduces historical tsunamis in Japan and several countermeasures such as seawalls, breakwaters and floodgates developed in each town and village after these tsunamis. Section 6.3 reviews several technical improvements as lessons of the 2011 Great East Japan Earthquake and Tsunami. These mainly focus on conceptual design with respect to 1) the height and strength of coastal defense structures, 2) a combination of structural and non-structural measures through land use management and 3) technical and communicational improvements of the tsunami warning system. Section 6.4 provides a perspective on the sea level rise impacts in Japan on tsunami hazard characteristics based on tsunami simulation case studies using various scenarios of sea level rise.

6.2 | Development of tsunami countermeasures in Japan

Japan is often hit by immense tsunamis, especially along the Sanriku coast of the Tohoku region (see Figure 6.1). The first recorded historical tsunami is the Jogan tsunami which occurred in 869. Then followed the Keicho-Sanriku tsunami in 1611, the Meiji-Sanriku tsunami in 1896, the Showa-Sanriku tsunami in 1933, the far-field tsunami from Chile in 1960, and (largest of all) the Great East Japan (or Tohoku) tsunami in 2011.

The 1896 tsunami caused nearly 22,000 casualties with more than 38 m run-up height, while the 1933 tsunami caused about 3,000 casualties with tsunami runup heights of nearly 30 m (Yamashita, 2008). Since then, coastal towns and villages in this area have started contracting coastal structures to mitigate tsunami impacts. For example, in 1934, construction of double 10 m high seawalls started in the town of Taro. These walls were completed in 1958, two years before the 1960 Chile tsunami, and fully protected the town against a maximum tsunami inundation depth of 3.5 m. In the 1970s, the town constructed another double line of 10 m high seawalls to accommodate the increasing population.

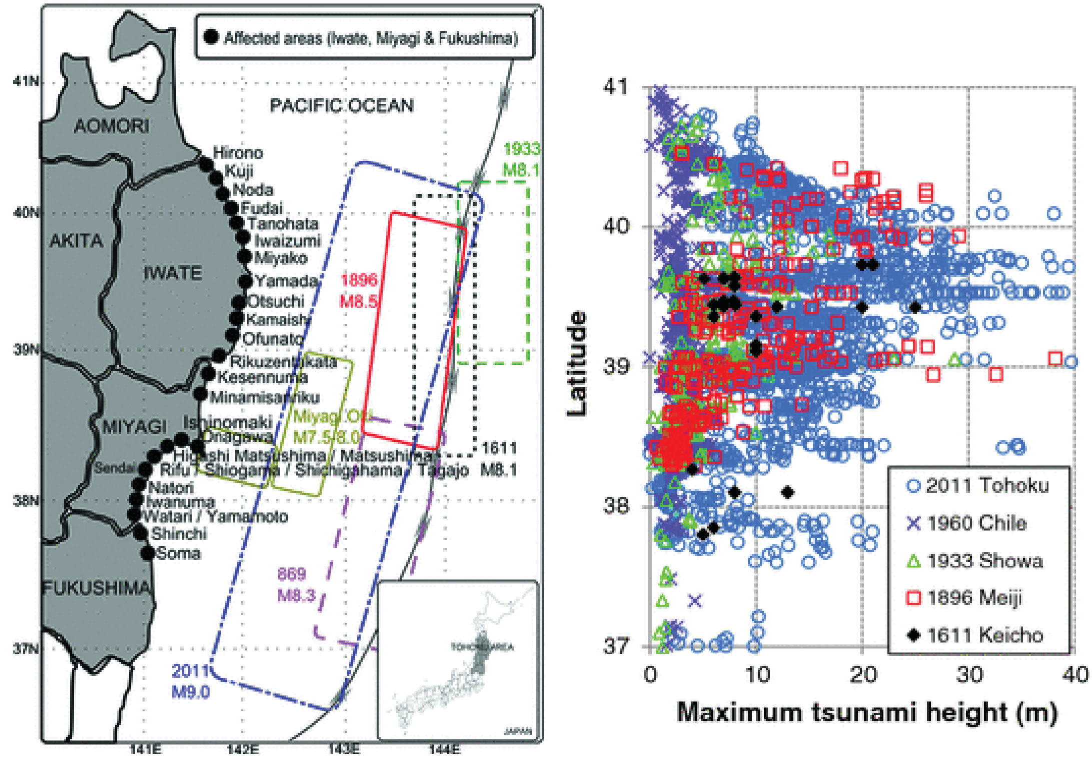

Figure 6.1 | Historical tsunamis in the Tohoku region. Left: Comparison of significant earthquake fault displacement areas. Right: Comparison of maximum recorded tsunami heights. (From Suppasri et al., 2013).

The total length of the seawalls was then about 2.4 km. The designs of both double lines of seawalls only took into consideration water inundation levels observed during the 1933 tsunami. However, the 2011 tsunami flowed over both double lines of seawalls, damaged most houses and destroyed the eastern part of the new seawall (Suppasri et al., 2012).

After the 1960 Chile tsunami, two breakwaters were constructed at the Bay entrance to Ofunato City. Located in the bay entrance where the water is 38 m deep, they had a 200 m wide opening and were 290 and 250 m long. Construction of the breakwaters was completed in 1967 and successfully protected the city from the local Tokachi-oki tsunami in 1968. Another large-scale breakwater scheme was built offshore of Kamaishi City. These tsunami breakwaters were 670 m and 900 m long and were constructed with a 300 m opening at the entrance into the bay with its base at a depth of 63 m, making them the deepest breakwaters in the world. Construction of the breakwaters was completed in 2009. Both of these tsunami breakwaters were heavily damaged by the 2011 tsunami event.

Nevertheless, the breakwaters helped to reduce the impact of the tsunami (in terms of both the tsunami height and arrival time) on the cities which they were designed to protect. This applied especially in the town of Kamaishi, where many houses still remained intact (Suppasri et al., 2012). For Kamaishi, two simulations were performed for cases with and without the presence of the breakwaters (PARI, 2011). Those results showed that the breakwaters reduced the runup height from 20.2 to 10.0 m and delayed the arrival time of the tsunami inundation by 8 min (from 28 to 36 min). Fudai village offers an example of a tsunami gate used to prevent tsunami intrusion from a river. In 1984, 15.5 m high tsunami gates were constructed close the river mouth. In the case of the 2011 tsunami, a 17 m high tsunami overflowed the gate but inundated only a few hundred meters past it. As such, most of Fudai village, including the evacuation shelters (primary and secondary schools) was not inundated (Token, 2011).

Many Japanese coastal defense structures partly mitigated or fully resisted the effects of the 1960 Chile tsunami, as well as those of other tsunamis which have occurred since then. Therefore, significant effort and attention was paid to such protective structural measures.

However, two local tsunamis that occurred in the Japan Sea initiated the introduction of non-structural measures such as early warning systems and land use planning. The 1983 Japan Sea tsunami arrived at the shore less than 10 minutes after the occurrence of the earthquake and the 1993 Okushiri tsunami arrived less than 5 minutes after the earthquake occurred and, unfortunately, before the official warning system disseminated any actual tsunami alert (Suppasri et al., 2021). The Japan Meteorological Agency (JMA) subsequently improved their tsunami warning system such that the first warning message can now be issued 3 minutes after the moment of the earthquake occurrence.

In addition, given the fact that a tsunami may arrive less than 5 min after tsunami generation and since rapid evacuation seems impossible, land use planning is needed for such areas. ToniHongo village in Kamaishi City is an example where residences have been built on high ground. The village was struck by the 1896 tsunami and the 1933 tsunami. After the 1933 tsunami, the village was rebuilt on higher land with an elevation of at least 20 m. The village survived the 1960 Chilean tsunami. However, after this event, many houses were built in lower elevation areas to accommodate the increasing population Those lower houses were subsequently destroyed by the 2011 tsunami (Suppasri et al., 2012).

6.3 | Improvements of tsunami countermeasures after the 2011 Japan tsunami

6.3.1 | Conceptual design for height and strength of coastal defense structures

The cause of most seawall failures was overtopping followed by scouring of the unarmoured heel of the seawall during the Great East Japan Tsunami (Suppasri et al., 2012). This was in fact not the first known case of this phenomenon. In 1968, in the case of the minor Tokachi Earthquake tsunami, a small part of the seawall was scoured by strong overtopping flow. However, the lesson of this seawall was not noticed, as the other seawalls were of sufficient height, and engineers thought it was necessary only to build the seawalls to that sufficient height. After the 2011 tsunami, damaged seawalls are currently being reconstructed along the entire Pacific coast of Tohoku with an array of design improvements aimed at preventing, or at least delaying seawall failure. The design of seawalls that are tall enough to prevent overtopping by the maximum feasible tsunami is financially impractical and the effects of such tall structures, which would separate the fishing and tourism economies from the sea, are undesirable.

Therefore, the new generation of seawalls have been designed to prevent a tsunami with a return period of up to 100 years (a so-called “Level 1” tsunami) from overtopping. Tsunamis that are larger than this (“Level 2” tsunamis) are expected to cause overtopping (Koshimura and Shuto, 2015). However, the new generation of seawalls and walls under construction along the Tohoku coast has been designed to better withstand the forces induced by overtopping and thus either not fail at all or stand intact for longer than the previous generation of seawalls so as to provide the endangered populace more time to evacuate. New seawalls have three principal differences from their pre-tsunami counterparts (MLIT, 2013). Detailed explanations are described in Suppasri et al. (2016) but general ideas are as summarized below and in Figure 6.2 (upper).

(i) Strengthened heel construction: This is meant to prevent, or slow, failure due to scouring of the earth at the heel of the seawall followed by slumping of the land-side armour into the scour pit and subsequent scour of the seawall material itself. Heel strengthening consists of a combination of measures including a concrete gravity anchor for the land-side armour and reinforcing the land surface landward of the gravity anchor to make it resistant to scour.
(ii) Strengthened crest and landside slope armour: Some of the seawalls that failed in 2011 were observed to have failed due to the crest and landside slope armour lifting off in zones of low pressure from the overtopping flow. Heavier armour is expected to mitigate this damage mechanism. The crest armour in most cases is now monolithic to better resist uplift.

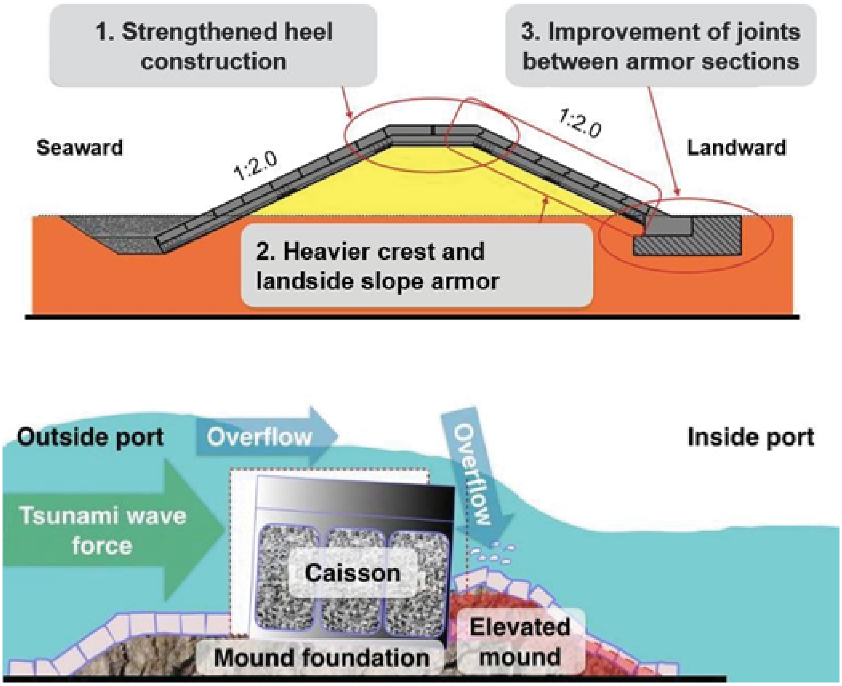

Figure 6.2 | Concept of new seawall and breakwater (From Suppasri et al., 2016).

(iii) Strengthened joints between armour sections: This entails either cast-in-place concrete slabs or precast interlocking armour blocks on each slope of the seawall and interlocking joints with the crest armour. Furthermore, the crest armour in most cases extends slightly down the seaward and landward slopes, effectively moving the joint with each slope to a less vulnerable position than the lip of the crest itself. In all cases, expansion joints between the concrete armour units are sealed to be watertight to prevent the scour of fill material during overtopping. Because overtopping and breaching in some sections is inevitable during a Level 2 tsunami, the new seawalls contain either sheet pile or concrete diaphragm walls at intervals of approximately 50 m. The purpose of these diaphragm walls is to interrupt the propagation of scour along the length of a seawall and thus limit damage to short sections.

Suppasri et al. (2016) also summarized new construction techniques for breakwaters after the 2011 tsunami which can be briefly explained as follows. The failure of the Kamaishi bay-mouth tsunami breakwater was estimated to have been due to scour of the rubble mound foundation when the strong overtopping jet impinged at the heel of the caisson along with rapid flow through the gaps between caissons. As shown in Figure 6.2 (lower), the Kamaishi breakwater is being rebuilt with a friction mat placed between caissons and the rubble mound, to reduce the likelihood of caisson sliding in the future. The failure of the Ofunato bay-mouth tsunami breakwater was also found to be due to caisson sliding but this can be mitigated by elevating the level of the rubble mound foundation on the harbor side of the breakwater. This elevated portion of the mound will act as a buttress to resist sliding of the caisson into the harbor when the water level on the seaward side is elevated during a tsunami. In addition, the harbor-side elevated rubble mound will be covered with concrete armour blocks to prevent scour during overtopping.

6.3.2 | Combination of structural and non-structural measures and land use management through multilayered mitigation system

Sendai City was one of the impact areas of the 2011 tsunami. Actually, the city unintentionally mitigated tsunami inundation by constructing the highway located approximately 4–5 km from the sea. The city then utilized this idea as a multi-layered mitigation system for such a coastal plain area. The conceptual plan is a combination of existing and new infrastructures such as coastal forest, seawall (reconstructed from 6.0 m to 7.2 m based on the Level 1 and Level 2 tsunami concept), land use zoning and elevated (6.0 m) existing road so that the tsunami flow depth is less than 2 m as shown in Figure 6.3 (Pakoksung et al., 2018). The planned view of the multi-layered system of Sendai City is based on a 7.2 m seawall reconstruction (originally approximately 6.0 m) and a 6.0 m elevated road. Several tsunami simulations based on different heights of the elevated road were performed to decide the most appropriate height so that the tsunami flow depth behind the elevated road is less than 2 m. This idea had been applied to the 2004 Indian Ocean tsunami affected area, in Banda Aceh, Indonesia. The so called the Banda Aceh Outer Ring Road is a planned elevated road parallel to the coast. This

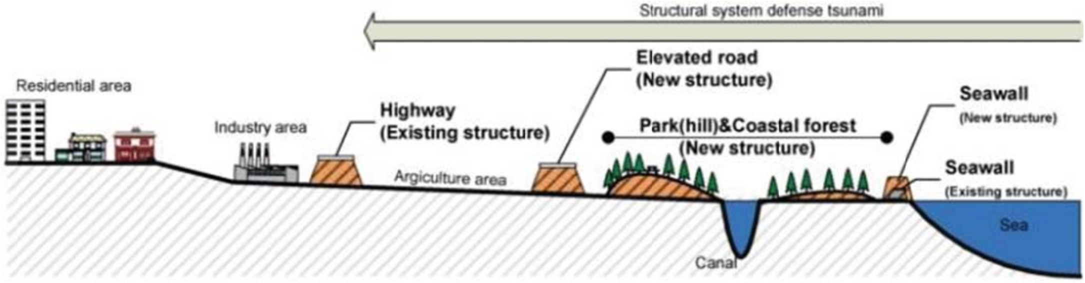

Figure 6.3 | Layout of multi-layered tsunami mitigation system in Sendai City (From Pakoksung et al., 2018).

road is planned not only to mitigate tsunami but also reduce traffic congestion during daily usage (Syamsidik et al., 2019).

6.3.3 | Technical and communicational improvements of tsunami warning system

Underestimation of the 2011 tsunami led to large improvements of JMA's tsunami warning system. There are two main improvements related to the tsunami warning system, 1) technical issues on real-time tsunami monitoring and simulation and 2) risk communication issues on conveying technical disaster related information to the public. At the time of the 2011 tsunami, a limited number of GPS wave stations were used. In addition to the previously installed sensors in the west of Japan (DONET), 150 new submarine tsunami sensors were installed by the Seafloor Observation Network for Earthquakes and Tsunamis along the Japan Trench (S-net) which is operated by the National Research Institute for Earth Science and Disaster Prevention (NIED) (Aoi et al., 2020) as shown in Figure 6.4.

Together with other newly installed sensors, JMA can observe tsunamis offshore in real time before they reach the coast and this information is useful for sending quick tsunami warnings, updates, and cancellations of these warnings. In addition, the JMA is also developing a new method (Tsunami Forecasting based on Inversion for Initial Sea-Surface Height, or tFISH) to predict coastal tsunamis by estimating their location and magnitude based on the waveform data observed offshore (Tsushima et al., 2014).

JMA also attempted to improve the understandability of their warnings. JMA released a modified version of the Tsunami Warning that emphasized immediate evacuation. The tsunami warnings/advisories/forecasts were reduced from eight to five classes to reduce such complexity of the warning level since very high tsunami warning accuracy is difficult for a very large earthquake (JMA, 2013a). Moreover, not only the quantitative estimated tsunami height but also the qualitative estimated tsunami height is reported (i.e. "Huge" for 5 m, 10 m, and over 10 m; "High" for 3 m; and "(N/A)" for 1 m). Since August 30, 2013, JMA has officially been using the "Emergency Warning System" to alert people of the extraordinary magnitude of natural disasters which is used for major tsunami warnings (JMA, 2013b). The Emergency Warning System is used to "alert people to the significant likelihood of catastrophes if phenomena are expected to be on a scale that will far exceed the warning criteria" (JMA, 2013b). If an Emergency Warning is issued, people should "evacuate immediately to a safer place such as high ground or a tall building designated as an evacuation center" (JMA, 2013b).

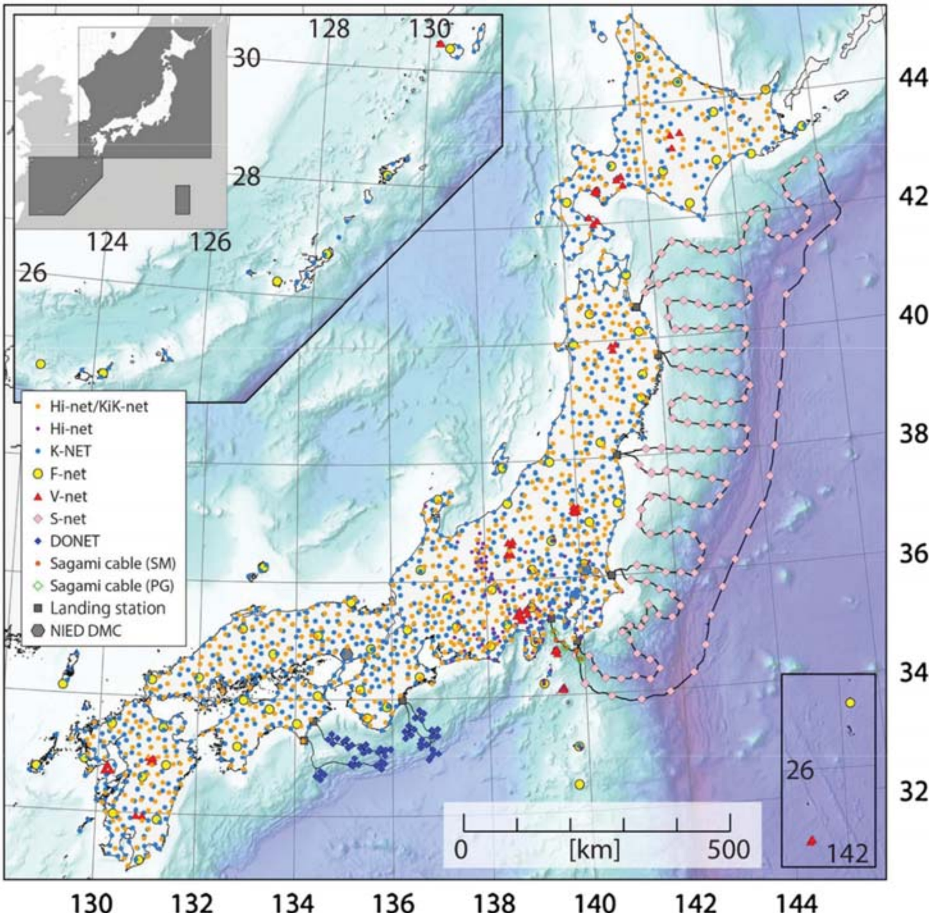

Figure 6.4 | S-net, DONET and other earthquake, tsunami and volcanic observation sensors operated by NIED (From Aoi et al., 2020).

6.4 | Future perspectives on sea level rise

Although several improvements have been made in response to lessons of the 2011 tsunami, including a new design concept for coastal defense structures, a new challenge is the impact of climate change (sea level rise) on tsunamis as well as the current coastal defense structures. Such an impact is more simply understandable than other types of hazards as rising sea level increases the initial water level of tsunami generation as well as flow depth and inundation distance (or area). There are some previous studies that sea level rise will increase both flow depth and inundation area in Banda Aceh, Indonesia (Tursina et al., 2021) and Tokyo, Japan (Nagai et al., 2020) as well as reduce the return period of the same size of tsunami in Macau (Li et al., 2018) and California (Dura et al., 2021).

This section demonstrates results from preliminary numerical analysis using potential large tsunamis caused by the local Nankai Trough earthquake in the west of Japan. Three cities along the Nankai Trough were selected as case studies for quantitative hazard assessment. The Cabinet Office of Japan published 11 earthquake fault models with different locations of large slips (Cabinet Office, 2012). Models no. 3 and 10 were used for tsunami simulations in Tokushima and Wakayama Prefectures and models no. 4 and 5 were used for tsunami simulations in Kochi Prefecture as large slips were located near these study areas.

A classical model for tsunami numerical analysis “TUNAMI-N2”was used to model tsunami propagation and inundation on land. The sea level rise scenario was selected based on the 2021 update of IPCC (2019) and values of 0.39 m and 0.71 m were used for the analysis.

Figure 6.5 shows examples of model results under high tide level in the study areas. The blue area shows tsunami inundation area at current sea level, while yellow and red show the inundation area for sea level rise of 0.39 m and 0.71 m respectively. It can be seen that tsunami flow depth and inundation extent increase as sea level rises. The largest increased inundation area is in Tokushima Prefecture which increases by 9% and 18% for sea level rise of 0.39 m and 0.71 m but corresponding increases are rather small for the study areas in Wakayama and Kochi Prefectures. Figure 6.5 also shows increasing inundation extents from study area cross sections.

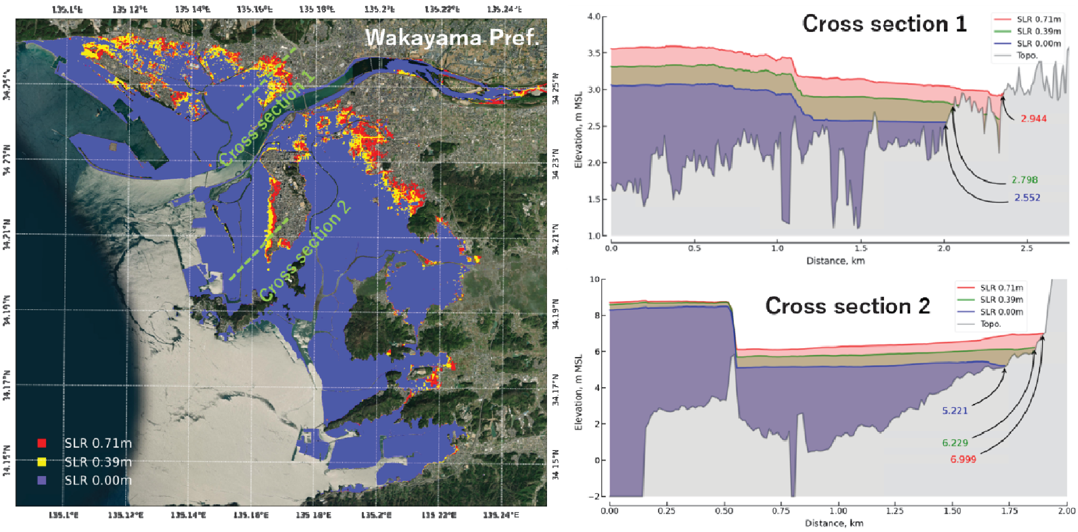

Figure 6.5 | Tsunami inundation map from the Nankai earthquake with the current sea level and sea level rise scenarios in study areas.

Tsunami inundation extends for all cases of sea level rise, by up to 500 m further inland. On the other hand, cross section 2 of tsunami inundation in Wakayama Prefecture shows that although the inundation extent does not largely increase, the amount of increased tsunami runup is 1.7 m which is double the sea level rise (0.71 m). Therefore, impacts of sea level rise are not negligible. Local topography conditions influence whether the tsunami inundation area or tsunami runup will be significantly increased.

6.5 | Conclusions

This chapter introduces Japanese practice on tsunami countermeasures based on historical tsunamis including the 2011 Great East Japan Earthquake and Tsunami. Structural measures such as seawalls and breakwaters have been widely constructed in Japan because of frequent tsunami occurrence. These structures helped to mitigate the 1960 Chilean tsunami and other local tsunamis after that. Nevertheless, such overconfidence in structural measures was recognized since the very early arrival of the local 1983 and 1993 tsunamis and the great 2011 tsunami. After the 2011 tsunami, a new design criterion for height of seawall has been proposed based on tsunami recurrence. Structures shall be high enough to prevent high frequency tsunami (Level 1) while allowing overflow for low frequency tsunami (Level 2). For the purpose of Level 2, construction techniques have been investigated to strengthen the structures, especially against damage on the rear side during overflow. Combinations of structural measures and land use planning have been implemented by making use of existing infrastructure. Results of tsunami simulation with different scenarios of infrastructure developments assisted the decision-making process. This idea has also been applied to a tsunami-prone area in Indonesia.

In addition, improvements on both technical issues on real-time tsunami monitoring and communication issues with encouraging tsunami evacuation have been made to optimize the new structural design and land use plan. Newly installed dense sensor networks increase accuracy of the warning, and the revised tsunami warning dissemination procedure supports the evacuation process. The future perspective of sea level rise impacts on tsunami was also discussed based on simulation results of large tsunami projected in the west of Japan. Preliminary results show that the maximum tsunami run-up can be double the sea level rise and that tsunami inundation extent increases as far as 500 m inland (an increase of almost 20% for inundation area) depending on the local topography. Therefore, policymakers should keep this in mind and require detailed studies of these issues for each location before actual implementation of the tsunami mitigation plan is finalized.

CHAPTER 7

Recent directions in coastal risk management

Alastair Barnett
HYDRA Software Ltd, New Zealand. E-mail: *barncon@xtra.co.nz*

Kwanchai Pakoksung and Anawat Suppasri
International Research Institute of Disaster Science, Tohoku University, Japan.
E-mail: *pakoksung@irides.tohoku.ac.jp, suppasri@irides.tohoku.ac.jp*

7.1 | Interaction between Sea Level Changes and Wave Height Probability

7.1.1 | Principles

In mid-ocean, wave heights and projected sea level rise are both small compared with the water depth, so wave height computations can be expected to behave linearly, that is, interaction between sea level changes and wave behaviour can be predicted by the principle of superposition. The effects of waves and sea level can be treated separately and the results combined by simply adding them together. For example, in deep water, navigation need not take account of tides, because although tides still affect surface levels, and waves respond to these, a floating ship responds in the same way, so *relative to the ship*, surface waves appear unaffected.

Tsunamis are closely related to tides (hence the reference to “tidal waves” in old textbooks), as both are gravity waves travelling at jet plane speed in mid-ocean, yet to a floating ship both are barely perceptible. This is partly because in deep water, gravity wave lengths are very long, and also because their corresponding wave heights are small, resulting in very flat slopes in both rising and falling stages. For example, Barnett (2022) quotes reports of direct tsunami height measurements for the 2004 Indian Ocean Tsunami ranging from 0.6 m in mid-ocean to 30 m on impact with cliffs. This is for the *same* wave, so any reported tsunami wave height measurement is usable only if accompanied by detailed location and local water depth information.

The same applies to tides, as a given high tide event may reach levels 1 m above Mean Sea Level (MSL) in one location, and over 5 m above MSL elsewhere. The Straits of Dover are well known for extreme tides, associated with the marked convergence of coastlines both through the English Channel to the west, and the North Sea to the north. This lateral tidal compression cannot be reproduced by the 2D

Table 7.1 | An example of published design extreme sea levels (metres to Hong Kong datum) Ng (1994, 2018).

Return Period (Years)	North Point Quarry Bay (1954-2017)	Tai Po Kau (1962-2017)	Tsim Bei Tsui (1974-2017)	Tai O (1985-2017)
2	2.73	2.91	3.07	2.87
5	2.94	3.20	3.31	3.16
10	3.09	3.45	3.51	3.36
20	3.24	3.73	3.74	3.57
50	3.45	4.19	4.09	3.84
100	3.63	4.60	4.40	4.06
200	3.81	5.10	4.77	4.28

modelling commonly used for tsunami wave propagation but will be reproduced by 3D modelling of the gravity waves as discussed in Chapter 2.

It follows that wave height probability distribution should strictly be discussed only with reference to data from a single recording station, preferably located at a coastal place adjacent to a channel. Therefore, a harbour entrance or river mouth would be most suitable for adoption as the downstream boundary shown in Figure 2.1. Table 7.1 above is quoted from Table 7.3 of the Fifth Edition (2018) of the Stormwater Drainage Manual (originally edited by Ng (1994)), as an illustration of the risk of applying design extreme sea level data from a recording station which does *not* represent the proposed development site.

The four recording stations report a range of almost 1 m between the 100-year return period design levels around the *same* harbour! This risk can be greatly reduced by calibrating a model (such as that shown in Figure 2.1) which successfully reproduces *all* reliable extreme sea levels. Interpolation or even extrapolation of the four records to other development sites in the harbour can then be approached with some confidence.

7.1.2 | A Worked Example

The basic principles are best demonstrated by reducing the required input data to a minimum. Suppose the design level of the underside of a road bridge deck is to be checked for the remaining bridge lifetime before wave action will probably attack the bridge. As pictured in Figure 7.1a, the chosen bridge connects two of the main population centres in Kiribati, crossing a channel between the ocean and the Tarawa lagoon.

Figure 7.1a | Example of analysis of the selection of design parameters for a coastal bridge at risk from sea level rise.

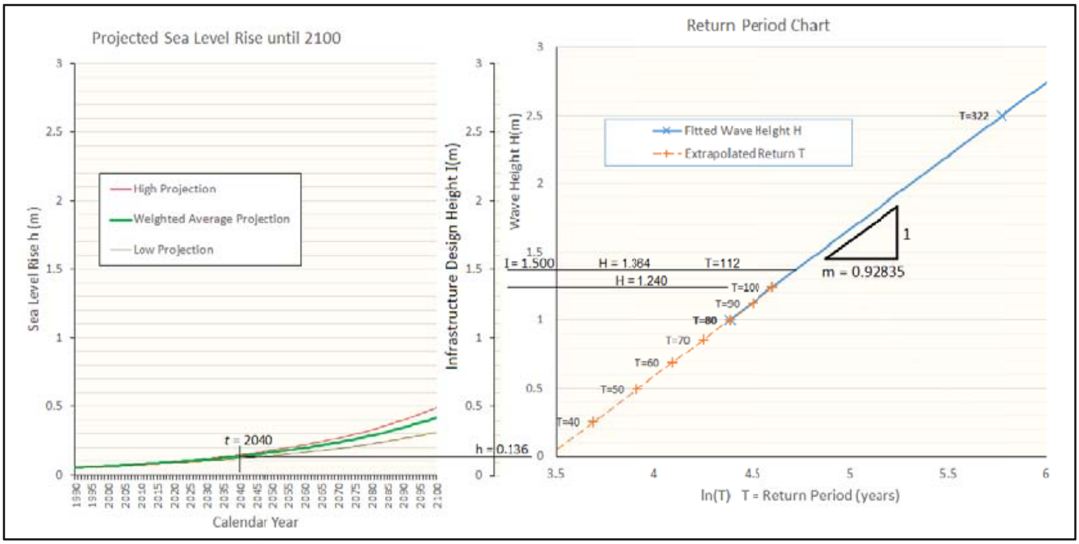

Figure 7.1b | Example of analysis of the selection of design parameters for a coastal bridge at risk from sea level rise (continued)

With a maximum land height of about 4 m, the Tarawa Atoll is a ring of motu (islets) where such vital infrastructure is at the highest risk worldwide from sea level rise. (*Disclaimer: The writer has no knowledge over the last twenty years of any investigations into the remaining lifetime of the chosen bridge. Therefore, the following discussion and results must be treated as purely hypothetical, developed using elementary data from outside Kiribati to illustrate the recommended principles.)*

The height of the bridge deck soffit (underside) above high tide may be gauged from the vehicles crossing the bridge in the photograph to be about 1.5 m, so for the purposes of this example that height will be assigned as the exact value of I, the infrastructure design height.

The working procedure starts from chart “Projected Sea Level Rise until 2100” on the left side of Figure 7.1b. The curves were produced from 2001 IPCC sea level rise projections, as reported by the New Zealand Ministry for the Environment (2004). The base data is presented in Table 7.2.

A semilog interpolation can fit a straight line between the two points on each of the two projections. This can be expressed mathematically as

$$\ln(h) - \ln(h_0) = k(t - t_0) \tag{7.1}$$

where h and h_0 are the projected high tide level rises at times t and t_0 respectively, and k is the gradient of the interpolated line. k is then found to be 0.0159 for the low projection, and 0.0200 for the high projection.

It appears that extrapolation using the same semilog analysis was also adopted in the IPCC projections, because the two derived lines cross in 1990 at a rise of 0.054 m. Note h_0 must be greater than zero at time t_0, because zero has no natural logarithm. Equation (7.1) can also be expressed as the exponential growth curve

$$h = h_0 e^{k(t-t_0)} \tag{7.2}$$

and this is the form chosen for plotting the projections in Figure 7.1b. As an example, the “weighted average curve” has then been plotted assuming a conservative weighting of 0.6 for the high projection and 0.4 for the low projection, and this is the curve used as the basis for the following sea level rise projections.

Turning to the “Return Period Chart” on the right of Figure 7.1b, this is constructed from the elementary base data given in Table 7.3.

Again, this data originates from the New Zealand Ministry for the Environment (2004), where the location “Tauranga” is one of several cities for which such data is listed. For present purposes the

Table 7.2 | Base data for fitting sea level rise projections in Figure 7.1b. Ministry for the Environment (2004).

Sea Level Rise (m)	**2050**	**2100**
Low projection	0.14	0.31
High Projection	0.18	0.49

Table 7.3 | Tsunami height H vs return period T for location “Tauranga”.

Tsunami height H (m)	1.0	2.5	5.0	10.0
Return period T (years)	80	322	3300	345,000

given tsunami H values might equally apply to other gravity waves. Again, a semilog model had been applied, as the data is found to lie along a line

$$\ln(T) - \ln(T_0) = m(H - H_0) \tag{7.3}$$

where T and T_0 are the return periods at wave heights H and H_0, respectively, and m is the inverse gradient of the interpolated line. As indicated in Figure 7.1b, the value 0.92835 was computed for m. It is clear immediately that the range of interest of wave return periods has now been set by the range of H being the same order of magnitude as I, the infrastructure design height, which is now set at 1.5 m.

Suppose the bridge was designed for an event of a return period of T years. This will be referred to as T_d, the "design return period", as this is often set by regulation authorities without reference to specific values of the infrastructure design height I. Then according to the Hong Kong Design Manual (Ng 1994, 2018) the probability (P) of the design capacity being exceeded *at least once* over its designed life (L_d) is given by

$$P = 1 - \left(1 - \frac{1}{T_d}\right)^{L_d} \tag{7.4}$$

This is the *stationary* case, where no account is taken of possible sea level rise. In the *non-stationary* case, the return period can no longer be taken as the constant T_d, because as time passes the sea level will rise, reducing the height H of wave required to reach the bridge soffit. The variation will follow the equation

$$H = I - h \tag{7.5}$$

For this reason, the Return Period Chart on the right of Figure 7.1b must be raised for each year which passes, so that by 2040, for example, the Return Period Chart must be raised by 0.136 m, the value of h for that year. Then the value of H corresponding with $I = 1.5$ is 1.364 m. Note that on this plot, T is *not* the design return period T_d, but the return period of the *event*, which through Table 7.3 is related to H. Since $H_0 = 1.5$ m, the corresponding $T_0 = 127.36$ years, and from Eq. (7.3) the T value corresponding with $H = 1.364$ m is 112.23 years.

Since this is close to 100 years, a common choice for design return period, it can be assumed that the authorities would expect 100 years to be the appropriate value of T_d. As shown in Figure 7.1b, this corresponds with a value $H = 1.240$ m. The year 2040 was chosen in Figure 7.1b, because if the bridge was designed in 1990 for a 100 year return period, then half of that return period will have elapsed by then, fifty years later.

The Return Period Chart plots Eq. (7.3) for the data in Table 7.3, which all fit on a straight line. If this is found not to apply with another similar tabulation provided for a project, some technique other than semilogarithmic modelling must have been used for constructing the table. However, a semilogarithmic chart can still be constructed as illustrated, simply by interpolating a straight line between the two points most relevant to the H value range of interest. In this example, the points at $H = 1.0$ and $H = 2.5$ derive straight from Table 7.3.

For spreadsheet tabulation, it is more convenient to manipulate Eq. (7.3) to give

$$\ln \frac{T}{T_0} = m\left(H - H_0\right) = -mh$$

which becomes

$$T = T_0 e^{-mh} \qquad 7.6$$

To investigate the difference between the stationary and non-stationary approaches, the value T_d in Eq. (7.4) must be replaced by T in the sense of the *event* as in Figure 7.1b. As shown by Eq. (7.6), this varies with h, the sea level rise.

Therefore for the non-stationary case, T_d from Eq. (7.4) has been replaced by T from Eq. (7.6), giving

$$P = 1 - \left(1 - \frac{1}{T}\right)^{L_d} \qquad 7.7$$

From Eq. (7.6), T will decrease as h increases, such that the value of the probability of exceedance P will increase faster than in the stationary case if the design lifetime L_d remains fixed. Alternatively, the lifetime L will decrease below L_d for the same given value of P. The second approach is more intuitively appealing, as only specialist actuaries can readily respond to news of a change in probability, whereas a change in *lifetime* is immediately understood by most people. The position is set out in Figure 7.2.

These plots compare the probabilities of exceedance of the peak level of a T-year event at the recording station according to various approaches. In all cases, the designed project life L_d was set equal to the design return period T_d, taken as 100 years.

The blue curve (Stationary $T = 100$ years) is the plot produced by Eq. (7.4). Note this curve predicts significantly lower probabilities of flooding than the other three curves, which are projections based on the non-stationary Eq. (7.7). The black lines (Compliance boundary) show that after 100 years (2090), Eq. (7.4) predicts a probability of flooding of 63.4%. This value turns out to be very close to all other cases where the designed project life is set equal to the design return period T_d, suggesting that this percentage could be defined as the threshold of unacceptable probability of failure. At the point where a projected curve crosses this line, the lifetime L of compliance with acceptable probability is then taken to end.

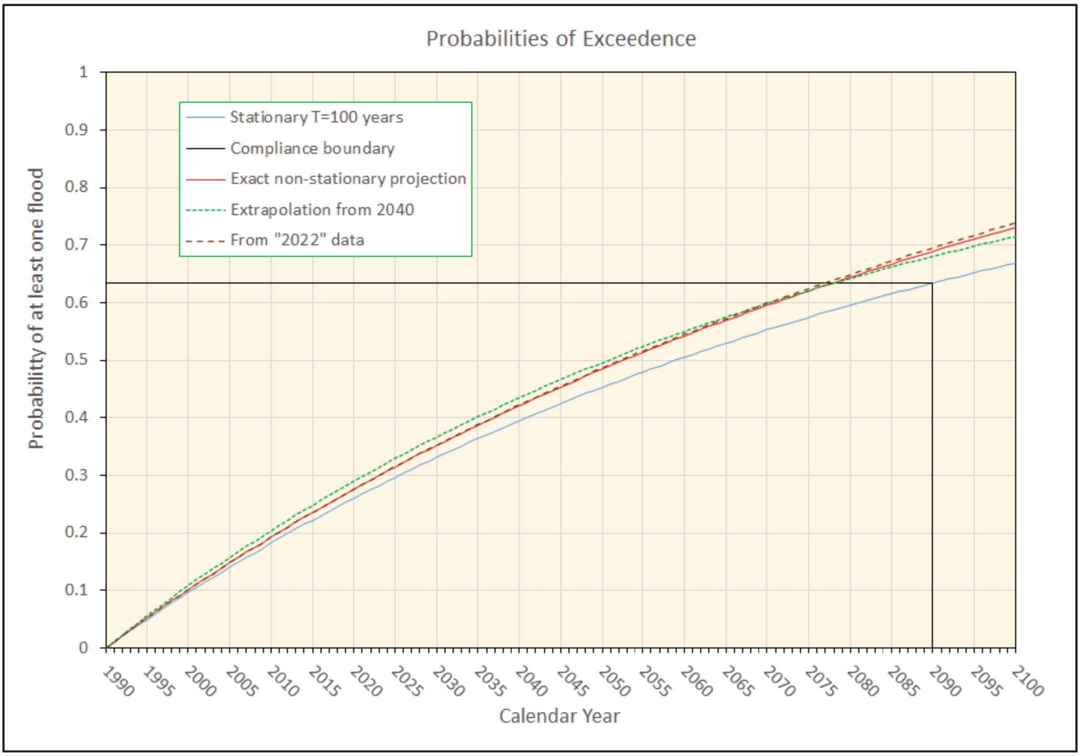

Figure 7.2 | Comparison of probabilities of at least one flood predicted by alternative models.

The red curve (Exact non-stationary projection) is the projection produced by calculating exact successive values of T according to Eq. (7.6). The non-compliance threshold then predicts a reduced project lifetime L ending in 2078 after only 88% of the design return period. The green square-dotted curve (Extrapolation from 2040) is found by running Eq. (7.7) with T fixed throughout using the 2040 value of $h = 0.136$ (see Figure 7.1b) corresponding with $T = 88.14$ years. Again, this curve predicts L ending in 2078, an almost exact match with the “exact” projection, but directly usable for adjustments based on data first coming available in 2040. (As in Chapter 4, “exact” here refers *only* to the numerical solution.)

Finally, the brown dashed curve (From “2022” data) offers a sensitivity analysis of errors between the predicted h and that measured at the recorder in 2022. No recorder was nominated in the IPCC projections of Table 7.2, so there is correspondingly no actual local 2022 measurement available. However, as an example, the “2022” value was taken as $h = 0.103$ m from the high projection in Table 7.2, compared with the original value $h = 0.097$ m.

7.1.3 | Discussion

This 6% difference assumed in h values in 2022 makes surprisingly little difference to the projected lifetime L, which drops by only 1 further year to 87 years, as shown in Figure 7.2. This encouraging insensitivity means that the measured 2022 value, with all the site-specific factors such as water temperature rise and tectonic effects (rising or sinking) included may predict a very similar reduction in the projected lifetime L to that predicted using models with only empirical accounting for such factors. The planning decision whether to specify a design life of fifty years or one hundred years will clearly have an influence comparable to the effects of sea level rise on flooding probabilities. These questions are all easier to address using comparisons of *lifetimes* rather than probabilities.

Further, compared with the designed project life $L_d = 100$ years, a 12-13% reduction in L will affect only the *end* of the design period, when the economic consequences to project finances are likely to be minor. This is not only because the success or failure of the project will have been clearly decided by then, but also because at that point the actual project design lifetime will increasingly depend more on the durability of the construction materials and building functionality than on flooding issues. In other words, few infrastructure projects last for their full design life before demolition and replacement by a design updated for changing demands often becomes an economic imperative.

That point is the time to review the case for raising design levels for any replacement building, or abandoning the site to increasingly probable flooding.

There is also a weakness in Eq. (7.3) with evaluation of H. Where high tide level changes can be computed accurately by averaging a very large population of data points when calibrating Eqs. (7.1) and (7.2), Eqs. (7.3) and (7.6) draw from a very small population, especially at the greater return periods. This raises the problem of consistent measurement of the wave height, especially when some waves may present as multi-peaked or strongly dependent on the state of the tide or wind. Barnett (2022) proposed that a scalar 2D continuous measurement of wave height should be integrated to give a deep-water measure of the potential energy in a passing wave. A theoretical link between total potential energy and the height of an idealized solitary wave could then be used to rank the observed potential energies in terms of their equivalent heights. Since potential energy is measured relative to the mean wave height during the passage of a wave, this should at least remove concurrent tidal effects from the height ranking.

7.2 | Japanese Case Studies

7.2.1 | Comparison of Two Ports in Japan

Table 7.4 is the extreme sea level in Japan collected from two example stations, Omaezaki in Shizuoka, and Mera in Chiba prefecture. These gauge stations are located in ports in Suruga Bay and Tokyo Bay, south of Tokyo in the middle of Japan (see Figure 7.3). The map was created with a QGIS software, version 3.16.15-Hanover (http://ww.qgis.org), the basemap was downloaded from QuickMapServices pluin (http://github.com/nextgis/quickmapservices).

The two recording stations report a difference of 0.7 m in extreme sea level height at 100-year return periods during 53 years of historical records. As with data from Table 7.1 for Hong Kong records, this illustrates the poor outcomes likely to result from simply adopting sea level records at a single point (the tide recording station) as being representative of an entire region, or even a single harbour. Instead, sea level projections at a proposed project site should be constructed by reproducible modelling of the regional water body (such as Tokyo Bay). Here “reproducible” obviously requires evidence that in calm conditions the model matches observed high tide levels at the recording stations *and* at the project site, and in extreme conditions the model still matches *both* gauging site sea levels at the return periods set out in Table 7.4.

7.2.2 | Projections of Sea Level Rise

As in the example based on Figure 7.1b, the working procedure starts from chart “Projected Sea Level Rise until 2100” on the left side of Figure 7.4 which was based on data collected from JMA (2022) and Garner et al. (2021). Observed data has been added from JMA (2022).

Table 7.4 | An example of extreme sea levels in Japan.

Return Period (Years)	**Mera gauge (1968–2021)**	**Omaezaki gauge (1968–2021)**
2	1.367	1.798
5	1.452	1.946
10	1.482	2.011
20	1.487	2.077
50	1.512	2.163
100	1.531	2.228
200	1.550	2.294

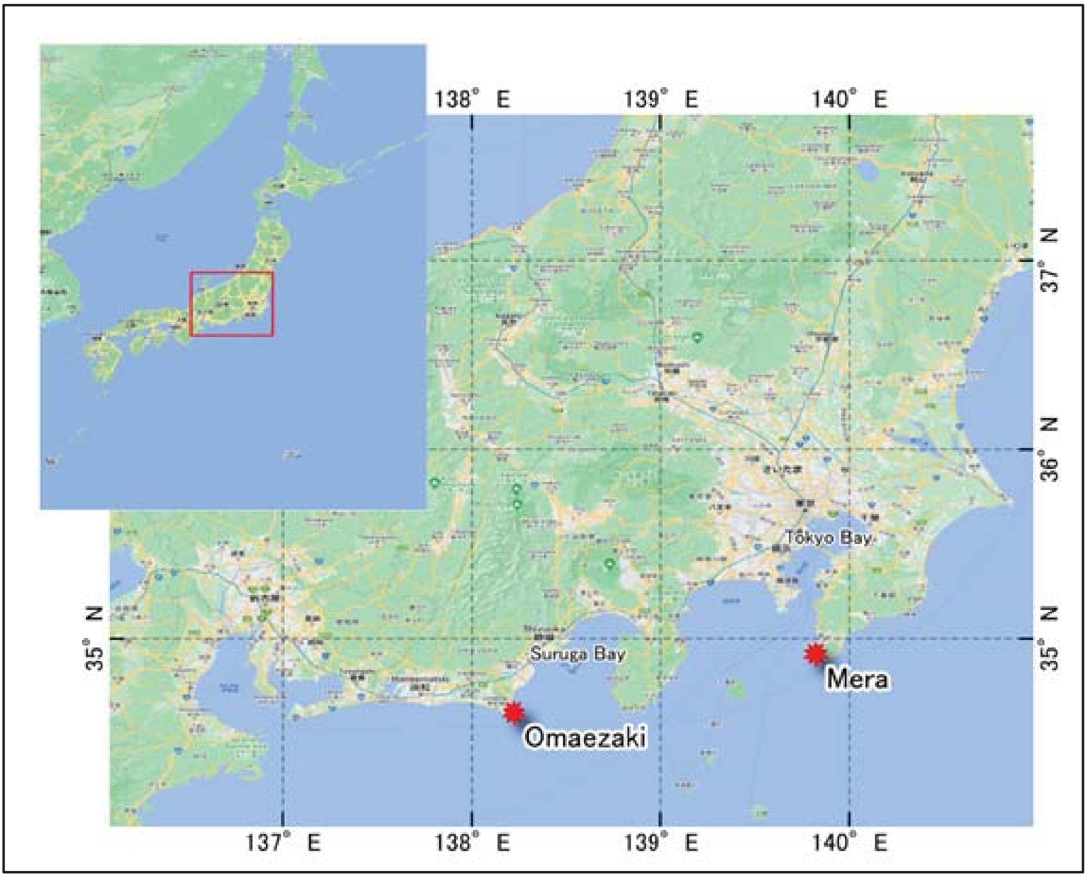

Figure 7.3 | Omaezaki and Mera port locations in Suruga Bay and Tokyo Bay, Japan.

The base data for the projected sea level rise is presented in Table 7.5. Unfortunately, the high projections made some twenty years ago for Table 7.2 now more closely resemble the *low* projections made recently for Table 7.5.

Table 7.5 | Base data for fitting sea level rise projections (see Figure 7.4).

Sea Level Rise (m)	2050	2100
High projection	0.45	1.01
Middle Projection	0.30	0.62
Low Projection	0.21	0.38

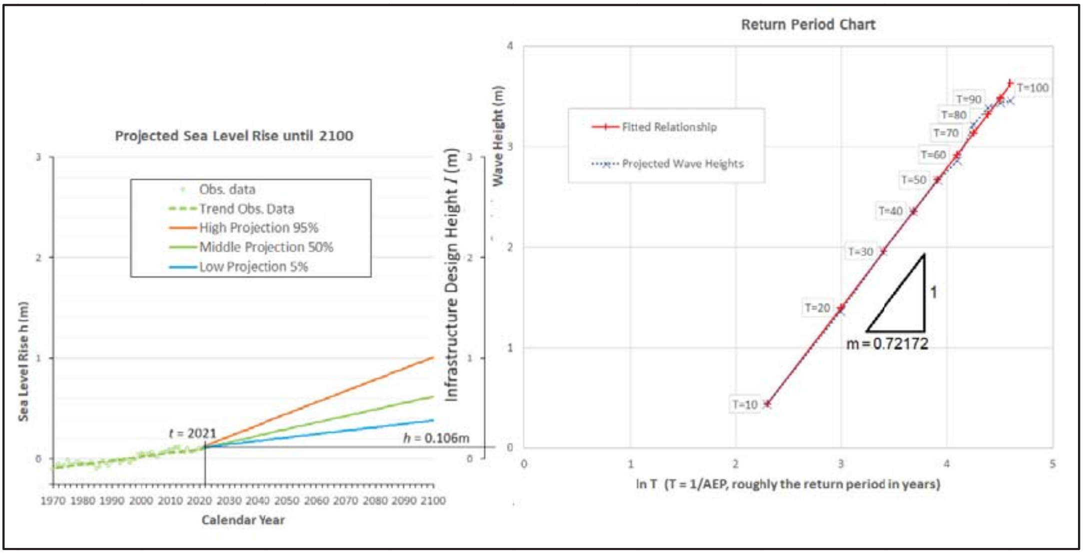

Figure 7.4 | Historical and projected sea level data until 2100, and tsunami wave height return period.

Further, in Figure 7.4 the sudden changes in gradient merely represent the transition (in 2022) from past measurements to future projections. Five years later, that transition point will have shifted to 2027, and *all three* of the high, middle and low future gradients would have to be modified accordingly.

If the consensus of scientific opinion represented by the projected sea level rises (presumably since 1990 – see Figure 7.4) as tabulated in Table 7.5 is to be treated with due respect, then the projections should include predicted future changes in gradient as provided by an exponential curve.

However, projecting an exponential curve backwards produces “exponential decay” towards a constant state, the “stationary conditions” widely assumed to have applied before 1990. It seems that sea level cannot be included as part of such stationary conditions, as the almost linear trend in the observed sea level at the Mera gauge (see “Trend Obs. Data” in Figure 7.4) continues back until modern records started in 1968.

This linear trend dates back well before 1968, as shown by records from Wellington Harbour in the Southern Hemisphere (New Zealand). Here continual sea level rise in the early twentieth century required establishment of a new sea level datum for Wellington City drainage infrastructure in 1953. This was originally 0.902 m against the Wellington Port datum, rising to 1.03 m by September 1989 (Barnett (1989)). In 2018, the 1953 datum was corrected to 0.929 m against the Wellington Port datum, and by 2021 the current mean sea level was given as 1.12 m, a rise of 0.191 m since 1953 (Greenberg

Table 7.6 | Projected tsunami height H vs return period T for location point A (refer Fukitani et al. (2021)).

Tsunami height H (m)	0.44	1.36	1.96	2.36	2.67	2.86	3.22	3.39	3.44	3.46
Return period T (years)	10	20	30	40	50	60	70	80	90	100

and McDonald (Draft 2021)). This gives an almost constant gradient of 0.00281 m/year for sea level rise from 1953 to 2021.

Turning to the "Return Period Chart" on the right of Figure 7.4, this is constructed from the elementary base data given in Table 7.6. The data originated from previous research by Fukitani et al. (2021). As with Figure 7.1b, the Return Period Chart must be (conceptually) raised for each year which passes. For example, in the year 2021 the chart must be raised by 0.106 m as shown, while by the year 2040, the chart must be raised by 0.19 m for the low projection.

These projected heights have been digitized from a plot in the reference paper. This presented projections of exceedance probability curves of the "tsunami inundation depth" based on all modes on modelling using Gaussian process regression. Since tsunami wave "heights" normally refer to the undisturbed level of the water surface (Barnett, 2022), whereas "depths" relate to the bed level of the channel, a correction must be applied to account for the depth of the bed below the undisturbed water level at Point A. From evidence presented in the reference paper, there is a probability of 1 (absolute certainty) that the inundation depth at Point A is exactly 10 m for a zero wave height, so the conversion from inundation depth to wave height must involve a simple subtraction of 10 m for all projections at Point A.

Therefore the figures for "tsunami height" at Point A in Table 7.6 were *all* derived by subtracting 10 m from the corresponding depths obtained at Point A from plots of tsunami inundation depth in the reference paper.

The Return Period Chart presents a semilogarithmic plot of the figures in Table 7.6, each identified as "Wave Height". At return periods from $T = 10$ years to $T = 70$ years, the model projections lie along a straight line, indicating that within this range (of main interest in infrastructure design) the linear "fitted relationship" with an inverse slope of $m = 0.07172$ simplifies the observed data to an exponential curve as expressed by Eq. (7.6). Above $T = 70$ years, errors are larger, but still distributed above and below the fitted line. Above $T = 100$ years, the reference paper suggests this pattern continues, but with decreasing relevance to infrastructure design as return periods exceed the reach of reliable historical observations for model validation.

7.2.3 | Sea Level as Global Marker of Terrestrial Water Balances

A schematic diagram of a conceptual global model is shown in Figure 7.5. Here the proportions of sea to land and of northern hemisphere land to southern hemisphere land are represented by shares of the circumference occupied. The Antarctic polar icecap is located at the South Pole, and the smaller Greenland icecap is seen near the North Pole. The Geoid is represented by the black circle, with the seas inside and the lands outside.

To avoid extraneous detail, the following simplifying assumptions are made:

- The total mass of water in liquid and solid forms on the surface of the earth is constant.
- The mass of water in gaseous form in the atmosphere is practically constant, in the sense that any changes have a negligible effect on the total water mass in liquid and solid forms.

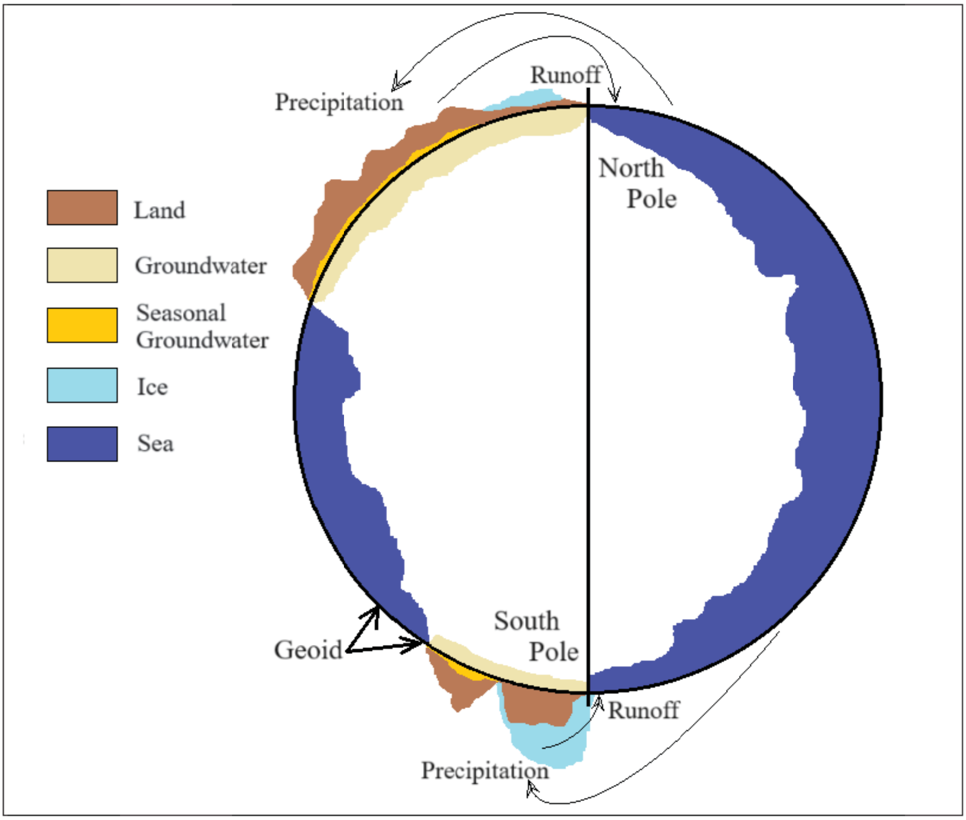

Figure 7.5 | Schematic model of global water balances.

- The total mass of groundwater inside the geoid (an approximation to a sphere based on global Mean Sea Level) depends only on the level of the geoid.
- The mass of groundwater outside the geoid may vary seasonally according to local balances between precipitation and runoff, but on a longer term basis depends only on the level of the geoid.

Flows from the inside to the outside of the Geoid are characterized as “Precipitation”, and those from the outside to the inside are shown as “Runoff”.

This simplifies the conceptual balance to an exchange of water mass between ice and the seas, as groundwater *inside* the Geoid makes little contribution to either precipitation or runoff. Where precipitation exceeds runoff over millennia, ice sheets build up to a great thickness and the sea level falls. On the other hand, warmer conditions initially prevent continuation of ice build-up, and eventually create runoff exceeding the precipitation. Sea level then rises, and the Geoid expands.

Therefore contraction of the ice sheets equals expansion of the seas, but with one important difference: measurement of land ice changes faces many local irregularities, while measurement of sea volume changes is a simple matter of recording the sea level rise, which according to hydrostatics should be the same if measured in any part of the world. Of course, exact hydrostatic conditions apply only in the laboratory, and some seas (in particular the Black Sea) have restricted connection to adjacent water bodies.

However, in the Pacific Ocean comparable mean level changes should be measurable at locations thousands of kilometres apart.

7.2.4 | Measuring Sea Level as a Global Marker of Terrestrial Water Balances

Returning to Figure 7.4, the Mera gauge is in a deepwater harbour on a peninsula of the Pacific coast (see Figure 7.3), so provides an excellent benchmark for measurements of sea level rise worldwide. The signal from the Mera Tide gauge is noisy, but a useful measure of change in gradient during the 1990s is provided by comparing the 22-year rise from 1968-1990 with those for the 22-year periods ending in 1991, 1992, 1993 and 1994. The mean rise over these five measurements is 0.057 m, a rate of 0.00259 m/year. This Northern Pacific rate is just below the mean gradient measured in Wellington in the Southern Pacific – see Section 7.2.2. In contrast, the 22 year Mera rise from 1995-2017 compared with the 22-year periods ending in 2018, 2019, 2020 and 2021 gives a mean rise of 0.093 m, a rate of 0.00423 m/year.

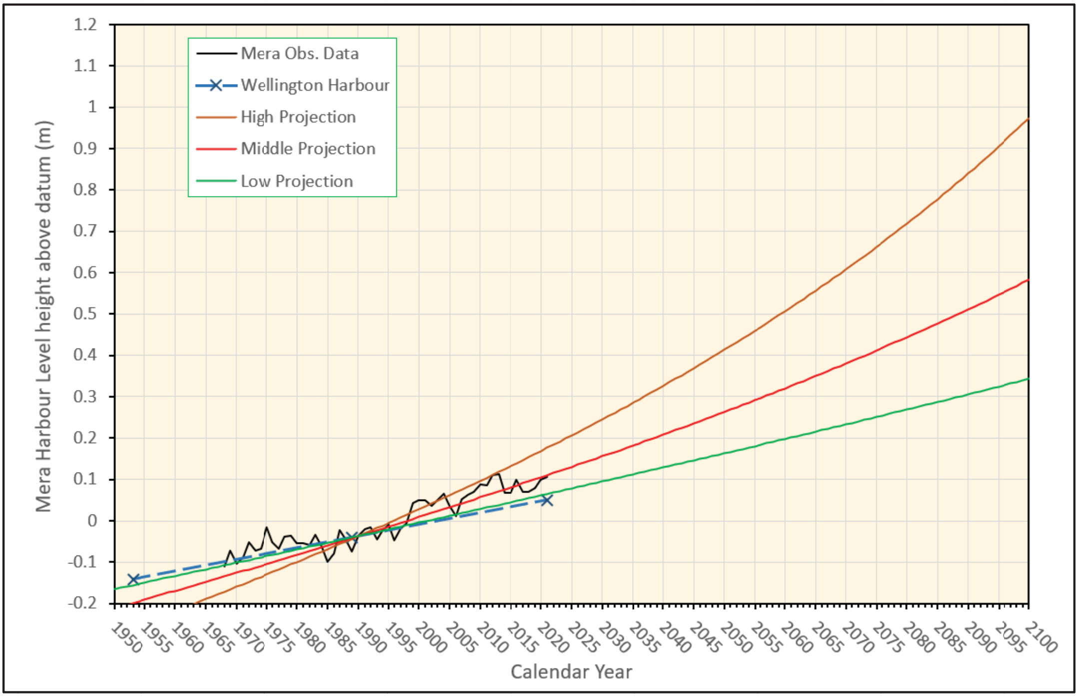

Figure 7.6 | Pacific Ocean sea level rise, with BSP model calibration at Mera Harbour.

As shown in Figure 7.6, this is clear evidence confirming that sea level is rising at comparable rates in the North and South Pacific, and it is tempting to go further and conclude that an increased rate of rise since 1990 in the North Pacific has yet to be replicated in the South Pacific. However the data in the Wellington record is far more sparse than that in the Mera record, so proper examination of such possibilities must await the recovery of New Zealand records of comparable quality. Tectonic movements of harbour datum benchmarks have also recently become available at both sites, but any extrapolation back to the twentieth century has yet to be proven.

Therefore, the most promising New Zealand benchmark sites through the twentieth century should be selected from the few deepwater harbours with a long record of consistent quality, in locations with little history of vertical tectonic movement.

The “BSP model calibration” in the Figure 7.6 caption refers to a solution developed and verified by the co-authors (Barnett, Suppasri and Pakoksung) to superimpose a projected exponential curve on a historical linear gradient.

The steady rise observed since at least 1950 suggests a conceptual model of ice melting from ever higher altitudes in the temperate zones. Steady retreat of lower altitude glaciers in most mountainous mid latitude areas has been widely reported, and indeed the writer has been able to observe this firsthand since an initial visit in 1954 to the New Zealand Franz Josef glacier, which then reached close to sea level. Any potential exponential growth of such glacier runoff is not evident in the sea level rise records, and this is consistent with the ever-decreasing area available for ice accumulation as successive altitude contours are exceeded. This general attenuation is obvious by consulting any atlas and provides a convincing explanation as to why exponential runoff growth has not been a feature of the twentieth century.

However, we have no reason to expect the same stabilizing effect if air temperatures around polar ice sheets start to exceed freezing point for extended periods, as indications of exponential growth in sea level rise are starting to be indicated by the records. The BSP model calibration fits the green linear-exponential curve well for almost linear sea level rise until late in the twentieth century. However some significant ice fields appear to have succumbed since then, although the Pacific Ocean is also subject to long oscillations such as well-known El Nino/La Nina forcing. This would partly explain the pattern of oscillations until the late 1990s, after which a different pattern begins developing, taking the path along the red (middle) line rated as the most probable by JMA (2022) and Garner et al. (2021).

This monograph proposes that adaptation from the familiar green line to this red line may still be economically feasible if action is taken in good time to control emissions as agreed in the Paris Accord. The design of such managed retreat is the theme of this text. However, if there is failure to fund such measures, any initial capital cost saving on emission reduction will be overwhelmed by costly losses of control of flooding as we creep past the red line towards economic chaos.

7.2.5 | Design Adaptation for Managed Retreat

Application of the BSP model calibration to the problem outlined in Figure 7.4 is demonstrated in Figure 7.7.

The left side of this Figure is now a version of Figure 7.6, with projections truncated to 2080 on the basis that interest for the next ten years is concentrated within the design building lifetime of infrastructure now under active consideration. The right side (Return Period Chart) is still based on Table 7.6 as for Figure 7.4.

Figure 7.8 presents a number of projections. The two blue curves show the cumulative probability of exceedance according to Eq. (7.7), with the full line beginning in 1990 and the dashed line in 2022.

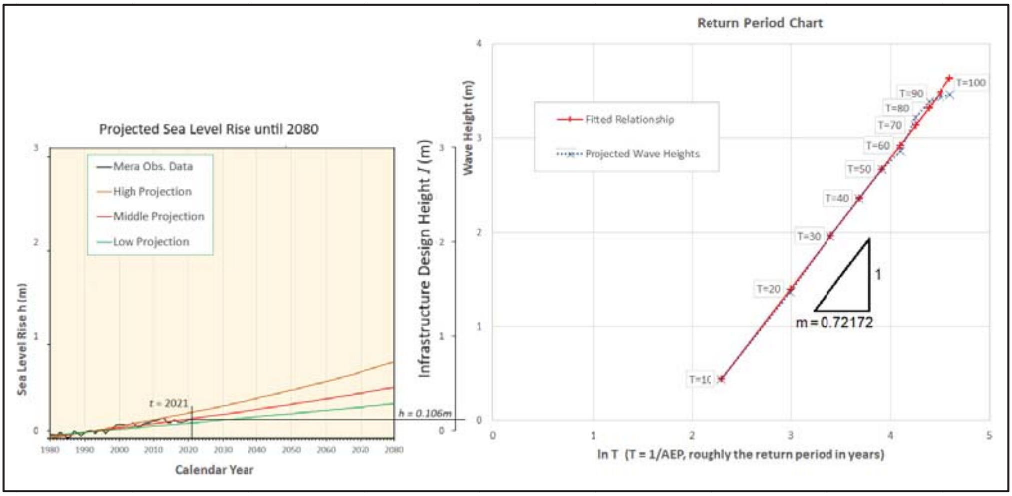

Figure 7.7 | Historical and projected sea level data until 2080, and tsunami wave height return period.

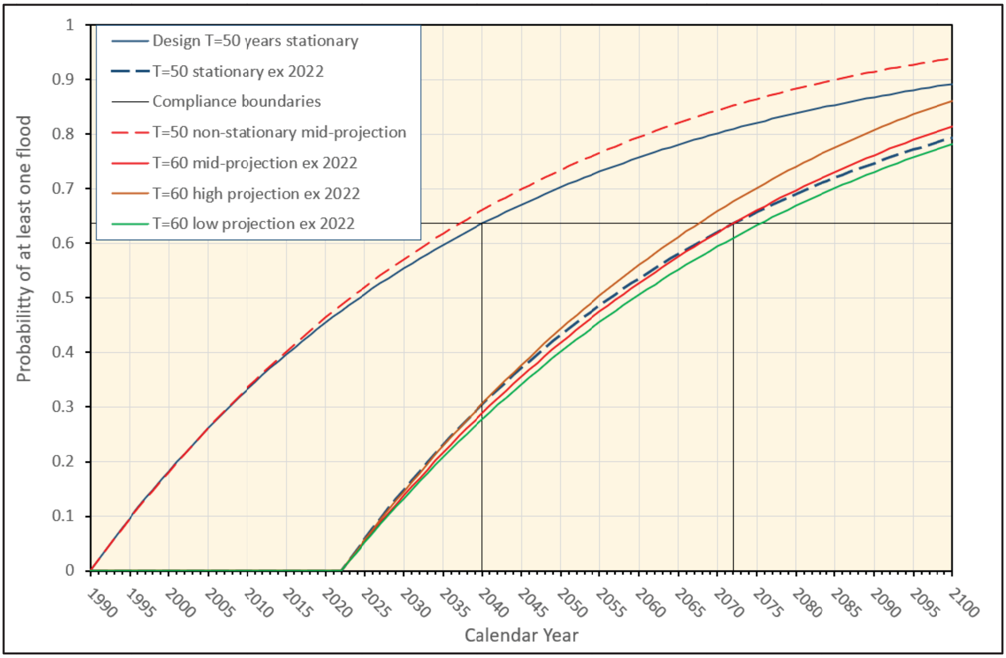

Figure 7.8 | Flood probability projections. All projections for T = 60 ex 2022 are non-stationary.

For T_d and L_d both equal to 50, the probability of exceedance at least once is 63.6%, and that is the compliance boundary marked (black lines) at the end of fifty years for the two stationary curves.

The two red curves have a similar relationship, with the dashed line beginning in 1990 and the full line in 2022. Both describe non-stationary projections of the "middle projection" values presented in Table 7.5. However the 2022 (full) curve is no longer a simple reproduction of the stationary 1990 (dashed) curve shifted 32 years to the right, because non-stationary effects now start from a higher annual exceedance probability in 2022, making the whole curve steeper than that starting in 1990.

This means that the curve starting in 1990 crosses the 63.6% probability compliance limit in 2037, giving a projected compliant lifetime of 47 years for the design, a decrease of three years in the design lifetime. In contrast, the curve starting in 2022 requires the design lifetime to be extended *ten* years to 60 years to match the design lifetime performance based on stationary data in 1990. Assuming that insurance premiums are based on design for a serviceable lifetime $L_d = 50$ years starting from 1990, most insurance companies are likely to increase premiums if they see failure to increase by ten years the design life starting from 2022. This increase is of course in terms of return periods (strictly reciprocal AEP values) derived from long term records based mainly on the assumed "stationary" (pre-1990) era.

If the flood risk is to be restored to "stationary" levels by returning the projected compliant lifetime to 50 years, insurance premiums should then return to pre-1990 levels (after allowing for intervening inflation). This could be achieved in 2022 by increasing *both* the design period T_d and the design lifetime L_d to *60 years* based on stationary pre-1990 assumptions. There is an alternative of taking into account recent (post-1990) events in setting new stationary values, but this would have an effect *only* if an event with an AEP less than 2% (T greater than 50 years) has been recorded near the development site since 1990. To avoid such random outcomes, it would seem simpler to extend existing records by subtracting the relevant measured post-1990 sea level rises to bring long term records back to a 1990 "stationary" datum.

A final important discussion concerns the range of predictions between the low and high projections in Table 7.5, which were based on the latest (2022) IPCC modelling results. In Figure 7.8, the non-stationary middle projection (red line) with $T = 60$ reached the 63.6% probability compliance limit in fifty years (2072). In comparison, the high projection (brown line) reached the compliance limit in 2068 and the low projection (green line) in 2076. (Note stability problems with the BSP calibration of the low projection required a small adjustment of the 2050 level from 0.21 m to 0.20 m. The 2100 level was unchanged at 0.38 m).

Concerns about higher high scenarios of sea level rise may then be set in comparison with the scale of an error between designing for a one in 46 year tsunami event and a one in 54 year tsunami event in order to recover a one in 50 year design event in pre-1990 terms. In this context of imprecision in the definition of an extreme wave event, it should be enough to work solely with the middle projection of sea level rise, neglecting the high and low projections.

CHAPTER 8

Can we trust model results?

Alastair Barnett

HYDRA Software Ltd, New Zealand. E-mail: *barncon@xtra.co.nz*

8.1 | Validation from first principles

8.1.1 | The concept of validation

The concept of validation is best introduced by an easily replicated laboratory experiment. “Validation” usually means demonstrating that a conceptual model conforms to the physical laws of nature. The first requirement for this is a physical prototype involving full scale flows of actual water for detailed comparison. With a laboratory pump capable of delivering steady discharges of up to 160 litres/s through the flume (see also Figure 5.5, Chapter 5), a simple prototype at scales commonly found in stormwater drainage systems is pictured in Figure 8.1.

The foreground represents a ponding area in a secondary flow path, drained in the background by a prismatic triangular channel of internal angle 100° and constant bed slope 0.003 with length 15 m.

Figure 8.1 | Transition from pool to channel in a triangular flume. See Barnett, Painter and Watkins (2004).

The ponding area joins the upstream end of the channel through a transition 2 m long, with horizontal invert and with the cross-section at the upstream end triangular with 1:3 side slopes. This demonstration prototype has great simplicity of definition, with only three cross-sections of three points each required to define the full 3D channel geometry to any desired longitudinal resolution using warped polygon interpolation rules from previous section to next section as shown in Figure 5.2 (see Chapter 5).

8.1.2 | Calibration

Calibration relies on accurate measurements within the flow circuit, shown schematically in Figure 8.2. The laboratory (see Barnett, Painter and Watkins (2004)) was equipped with an electromagnetic flow meter, but any group wishing to replicate the experiment for teaching purposes can obtain equally accurate steady flow measurements using a traditional calibrated discharge pit, a depth gauge, and a stopwatch. This will give flow accuracies to within 1%, and as discussed in the reference, measurement of surface level *h* can be achieved to a similar accuracy using care to take and compare repeat measurements.

Calibration of the resistance of the flume lining then requires a combination of these measurements. The material chosen was of uniform roughness defined by the Manning *n*. In a uniform channel, this value can be estimated from the Manning formula for uniform flow

$$n = \frac{MAR^{2/3}S^{1/2}}{Q}$$

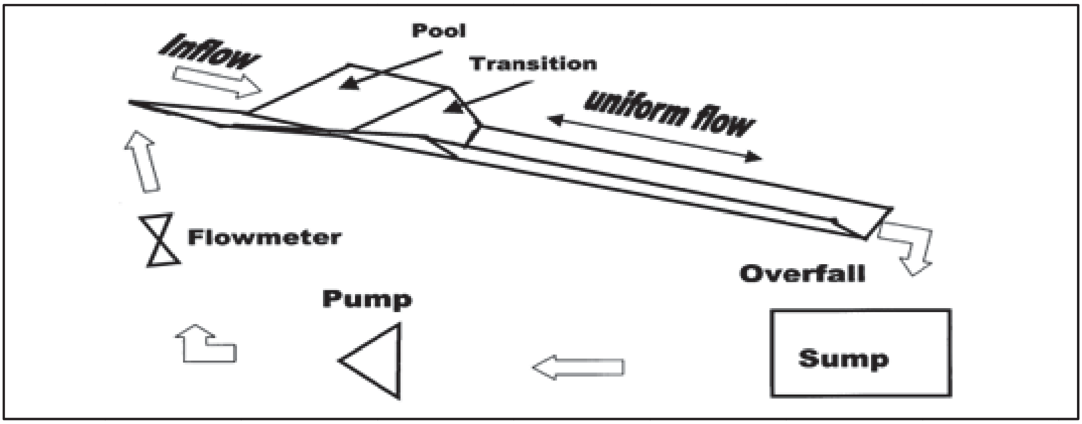

Figure 8.2 | Laboratory flow circuit. See Barnett, Painter and Watkins (2004).

Here all variables have been defined previously (see Chapter 5) in Eq. (5.1), except for S, which is the slope of the uniform part of the channel. In practice it can be difficult to set and maintain an ideal uniform slope over the full length of the physical channel, as deflection of the flume structure will vary with the weight of water currently in the flume, which changes from experiment to experiment. This particularly affects channels of nearly flat slope such as in this case.

A procedure was developed based on adjusting the bed slope to the required 3mm/m under a static water level pond created by closing the downstream channel end. This facilitated precise bed slope calibration, but under non-uniform loading slowly increasing from upstream to downstream.

Minor local deflections were then still observable under uniform loading corresponding with steady flow, but this experiment was specifically designed to minimize the importance of wall shear stresses in relation to wall normal stresses associated with changes in channel width. Therefore the primary requirement was to measure width variations through the channel transition and to determine the steady Q and h at each end of the transition by direct measurement. For the secondary establishment of Manning n downstream of the transition, the small variations in the bed slope would create local M1 and M2 curves (see Section 2.5, Chapter 2), but numerical modelling showed that these would have little effect on the levels through the transition as long as the downstream flow depths remained close to uniform.

For the flooring vinyl used in the original experiment, the Manning n calibrated to 0.011. If similar material is used in a replicated experiment, a similar result should be expected, but if a significant difference is found, a new Manning n calibration should supersede the original value in numerical modelling comparisons.

8.1.3 | Verification

Verification normally means confirming a calibration by obtaining a very similar result using an independent second calibration. Once the Manning n has been calibrated, all necessary information is available to find the discharge if the boundary value of the level h is provided for the pond upstream, because the downstream boundary is available from the relationship developed between Q and h in the uniform channel. The easiest way to apply this relationship is to define the downstream boundary level as a first guess at the uniform depth, when a longitudinal M1 or M2 profile will provide the correct uniform depth upstream for the computed flow solution.

In short, the verification problem can be summarized as in Figure 8.3.

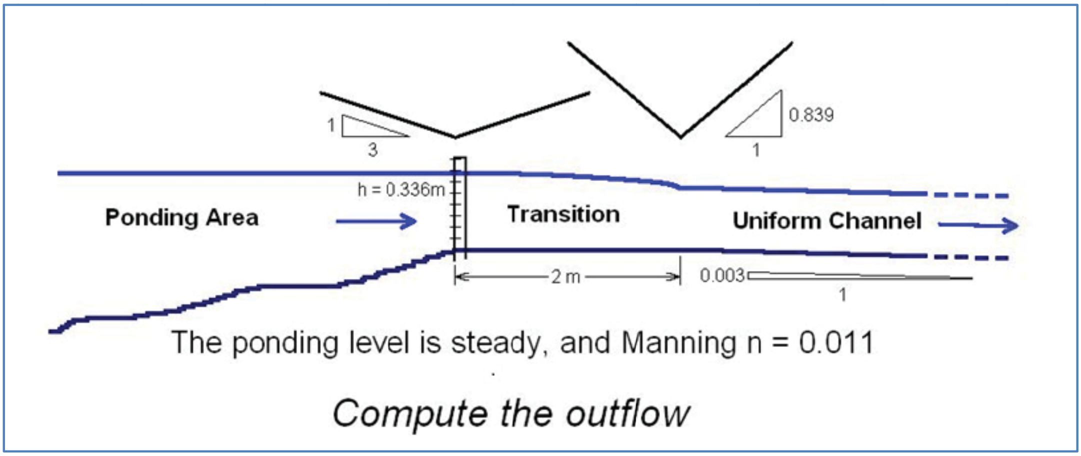

Figure 8.3 | The verification problem for modelling the pool/channel prototype.

Cunge, Holly and Verwey (1980) derived the momentum differential equation along the vector x component (longitudinal) axis as

$$\frac{\partial Q}{\partial t} + \frac{\partial}{\partial x}\left(\frac{Q^2}{A}\right) + gA\frac{\partial y}{\partial x} + gAS_f = 0$$

Their terminology was the same as that used in this document, except their y has here been defined as h, following the textbook practice of Henderson (1966). Making this change, dropping the unsteady (first) term and integrating from Section 8.1 to Section 8.2 gives the *steady* momentum integral equation

$$\frac{Q_2^2}{A_2} - \frac{Q_1^2}{A_1} + g\int_{x_1}^{x_2} A\frac{\partial h}{\partial x}dx + g\int_{x_1}^{x_2} AS_f dx = 0 \qquad 8.1$$

As discussed by Cunge et al., the differential form of this equation requires an assumption that flow variables A, Q etc. must be continuous (that is, differentiable). No such requirement applies to the integral form (8.1), and since this paper is discussing flow discontinuities that form will be used here. The first two terms result directly from integration of a variable which appears in divergent form. However the two remaining integrals cannot be expressed so simply because they are not in divergent form except when A is constant.

A first approximation is to simplify the integrations in Eq. (8.1) by finding A_m, the mean area through the reach between Sections 8.1 and 8.2, and to substitute this constant value for A throughout. The resulting simplified momentum equation is

$$h_1 + \frac{Q^2}{gA_mA_1} = h_2 + \frac{Q^2}{gA_mA_2} + \int_{x_1}^{x_2} S_f dx \qquad 8.2$$

The differential energy equation (see Henderson (1966)) is already in divergent form, so on integration it becomes

$$h_1 + \frac{Q^2}{2gA_1^2} = h_2 + \frac{Q^2}{2gA_2^2} + \int_{s_1}^{s_2} S_f ds + K_c \frac{Q^2}{2gA_2^2} \qquad 8.3$$

Here the streamwise *s* longitudinal axis is a scalar, which may be curvilinear in three Cartesian dimensions as in Eq. (2.8) (Chapter 2). As this paper is dealing with flows through channel contractions, it is conventional to add the last term to express energy losses associated directly with contractions in addition to those arising from wall shear. K_c is an empirical contraction loss coefficient, with a median value of 0.06 (see Chow (1959)) in tapered contractions, as in this problem. When the flow is uniform in a prismatic channel, both equations (8.2) and (8.3) give the same results, but such conditions are actually rare in open channels, either because of non-uniform longitudinal profile development in a prismatic channel or because the channel is non-prismatic, as illustrated in Figure 8.1.

In Barnett, Painter and Watkins (2004), results from the simplified momentum Eq. (8.2) were compared with the corresponding results from the energy Eq. (8.3) when modelling flows in the strongly non-prismatic pool/channel prototype. Figure 8.4 compares the momentum and energy model results obtained for a pond level of 0.336 m using cross-section spacing of 2 m, 1 m and 0.1 m as indicated by markers on the key legend. Finally, the full line indicates the energy result with 0.1m spacing plus "Eddy" corresponding with the value of $K_c = 0.03$ calibrated to match the measured flow of exactly 100 l/s. This value is within the guidelines provided by Chow (1959).

Clearly the simplified momentum model fails at larger section spacings, overpredicting flows by up to 17%, although the error decreases to only 2% at the fine grid spacing of only 0.1m. This is an illustration of the property of *convergence* in numerical solutions, where valid models should all converge to the same answer with sufficiently fine grid spacing. However grid spacing has no equivalent in the prototype, so the ability of the momentum model to produce serious errors for unsuspecting modellers means that verification has succeeded for the energy analysis but *failed* for the momentum analysis.

This is why experienced numerical modellers will *always* check the sensitivity of answers to grid refinement, and not trust model results until the answers with successive refinement will converge acceptably.

An alternative view of the difference between verification and validation is shown by Figure 8.5.

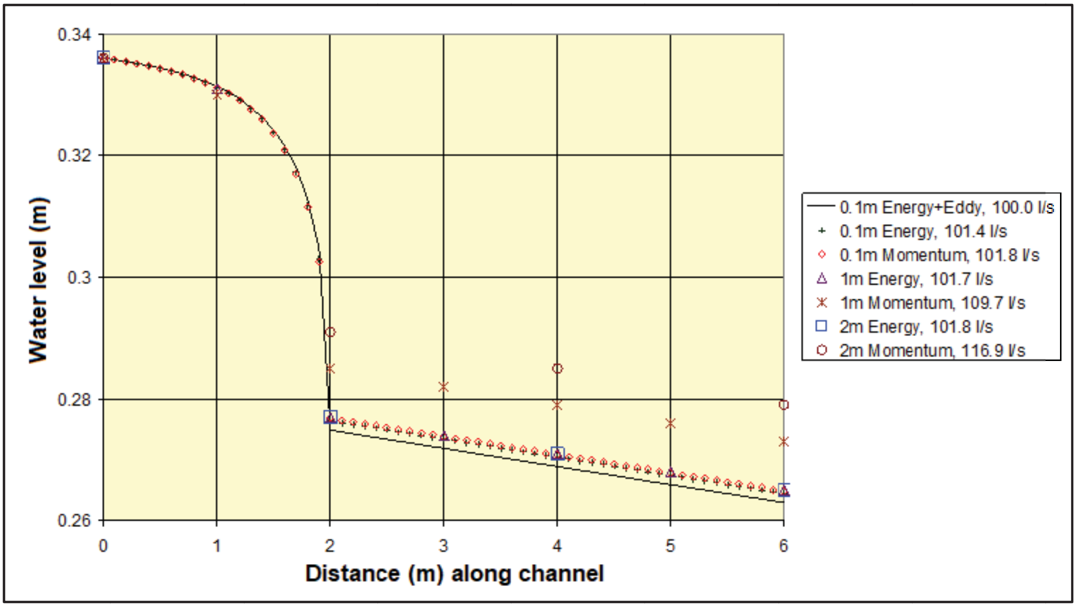

Figure 8.4 | Comparison of longitudinal water level profiles using energy and momentum models.

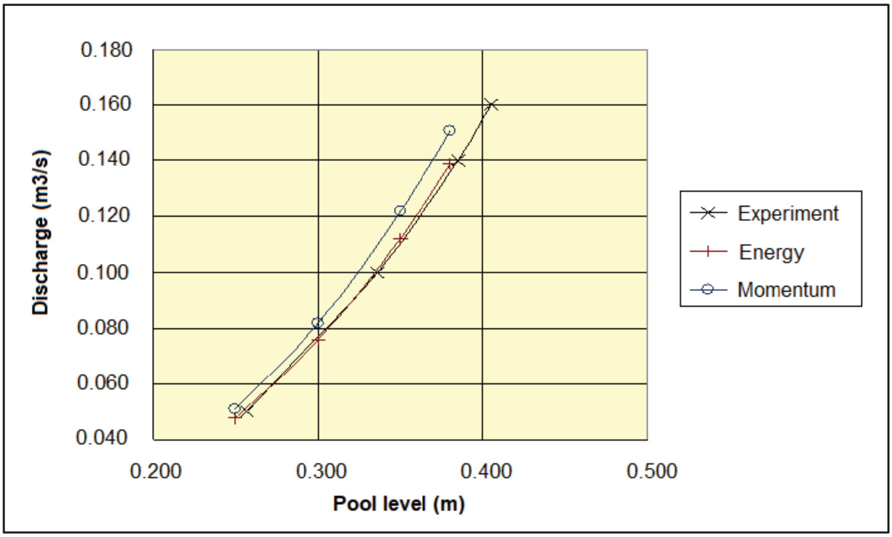

Figure 8.5 | Comparison of a series of model discharges with experimental results.

This plot compares results for a cross-section spacing of 1.0 m, a typical practical minimum value for flood modelling software packages in commercial production. Problems with the simplified momentum solution are by no means restricted to the previously selected case of 100 litres/s, as the flow overestimate is approaching 10% throughout the range tested. This is the reason for the “False pump” reference in the title of the 2004 paper, as predicted flow through the channel is consistently increased with no physical basis.

Had *only* convergent results been compared, a cross-sectional spacing of 0.1 m would have been required. The corresponding discrepancies between predicted and measured flows would have been reduced below 1 litre/s (1%), the rated accuracy of the flow meter. At that point the agreement between momentum and energy solutions would have been close enough for validation of *both* to be approved.

As can be seen from the legend in Figure 8.4, the energy solution (with $K_c = 0$) for a pool level of 0.336 m was almost independent of the section spacing, changing by only 0.4% through a twenty times size increase from 0.1 m to 2 m. Such solutions are called “robust” as they are barely affected in either accuracy or stability by the non-physical section spacing.

8.1.4 | Practical validation for model users

Table 8.1 summarises the results of the validation study.

The second row tabulates the results for the energy solution found for a given range of upstream pond levels, and the third row provides the corresponding discharges as measured in the laboratory. This material should enable users to set up models (both computational and physical) in their own laboratory to test the validity of their current choice of modelling packages for analysis of open stormwater drainage channels.

The essentials of the test model are summarized in Figure 8.3, and the data provided there should be easy to transfer to any alternative office modelling system chosen by the user for comparison.

Replication of the model Q results as quoted in the second row of Table 8.1 should hardly take longer if the freeware *AULOS* Version 5 executables (compiled from source code ©HYDRA Software Ltd)

Table 8.1 | Energy model solution (section spacing = 1 m, $K_c = 0.03$) compared with experimental results.

Pond Level (m)	0.256	0.307	0.336	0.360	0.384	0.395	0.405
Model Q (m^3/s)	0.050	0.080	0.100	0.119	0.141	0.152	0.161
Measured Q (m^3/s)	0.050	0.080	0.100	0.120	0.140	0.150	0.160

are downloaded from http://www.auloshydraulics.com/software-download after which preloaded pool/channel prototype data files are activated by pressing the *AULOS* RUN button.

Finally, replication of the laboratory measurements in the third row of Table 8.1 would require construction of the pictured flume to the same specifications. With the guidance provided, this should require only competent laboratory model building skills, and is suggested as a project for a Masters course student.

8.2 | Validation from large scale field data

8.2.1 | Large urban streams

The necessary documentation for test validation of modelling of the Opanuku Stream in Auckland, New Zealand, has been available for some years from the IAHR Web site. See the Resources Library of TC on Flood Risk Management in https://www.iahr.org/index/detail/160.

From that site, the paper Opanuku_Stream_Benchmark_Validation.pdf is available to IAHR members for download. For convenience, this is reproduced in Appendix A.

8.2.2 | Long term simulation

See Chapter 5, Section 5.5. As in Section 8.1.4 above, the 26 year model runs of the Kleine Emme river in Switzerland can be replicated at a rate of approximately 1 minute computing time per year if the freeware *AULOS* Version 5 executables are downloaded from http://www.auloshydraulics.com/software-download (source code ©HYDRA Software Ltd) and preloaded river model data files are activated by pressing the RUN button.

8.3 | Acknowledgements

Permission to publish photographs and graphic images is acknowledged as follows:

Figure 8.1, 8.2: Lincoln University (D. J. Painter, S. L. Watkins)

APPENDIX A

Opanuku Stream Benchmark Validation

A.1 | Introduction

The model accuracy benchmark published by the Flood Risk Management Committee of the IAHR in https://www.iahr.org/index/detail/160 had requirements stated for Validation.

Also the following statement was included in the instructions: “Note this benchmark has been validated by a published demonstration of compliance using the Chézy formula as the base resistance model. Hydrological computations used a simple kinematic wave rainfall/runoff model.”

The specified successful validation was performed on the *AULOS* Package developed by HYDRA Software Ltd, and this document now presents an updated collation of the various literature covering that validation over the last ten years.

A.2 | The Opanuku Stream Model

The benchmark dataset derived from one of the most intensively monitored river reaches in the urban territory of the Auckland Council, New Zealand. At the upstream section, the Border Road bridge, the water level is monitored continuously by a recorder. At the downstream section, the Vintage Reserve footbridge, the water level is also monitored continuously. In addition, the discharge has been gauged there repeatedly over almost 20 years under a range of conditions, including steady flow and rising and falling flood flows.

The model files listed in Appendix A specify cross-sections from distance 3.429 km at the Border Road bridge to 4.798 km at the Vintage Reserve footbridge, and thereafter a short distance downstream to the last measured section at distance 4.839 km. As a precaution, a further extension downstream from distance 4.839 km to 5.100 km was extrapolated to ensure that backwater effects of any downstream boundary error would not intrude into the study reach upstream of the Vintage Reserve footbridge. Although no surveyed cross-section data was available in this extrapolation zone, Lidar information was considered sufficient to support the lesser accuracy required for extrapolation of the channel bed.

Figure A.1 indicates the layout of the *AULOS* cross-sections. Note the background aerial photograph has been blanked out below the 10 m contour, providing clear space for superimposing a plot of channel depth contours at various stages of the flood. An initial low flow stage is shown.

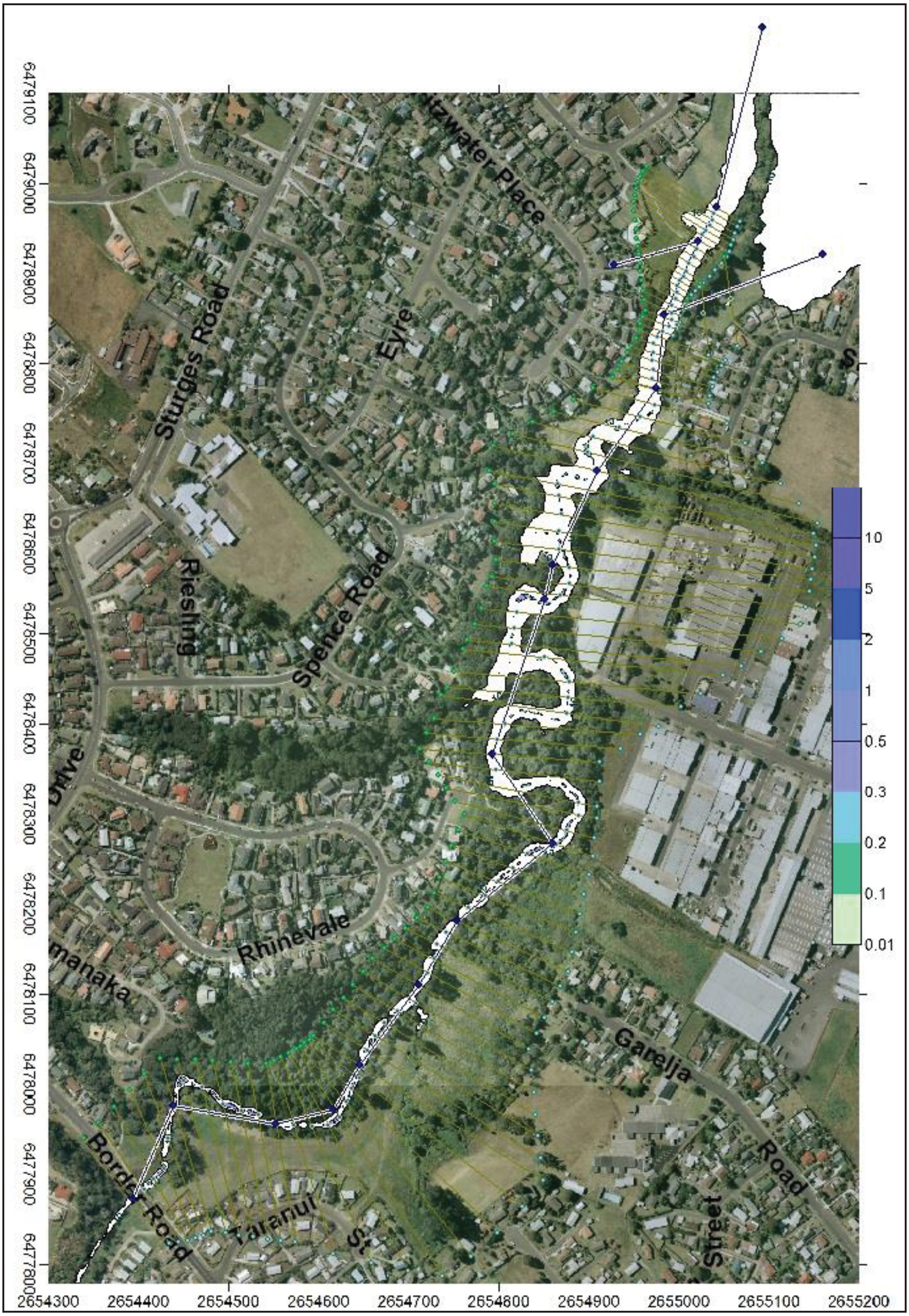

Figure A.1 | AULOS Model Cross-Sections along the Test Reach.

The schematised channel axis is shown in dark blue, with nodes shown as diamond shapes, also dark blue. Most of the nodes simply signal the position of the surveyed cross-sections as supplied with the benchmark dataset. Outside the low flow channel, sections were extracted from the Lidar terrain model using the *AULOS* editor. The cross-section survey was preferred for the low flow channel, as Lidar readings have problems where water was covering the bed during the Lidar measurements. As seen in Figure A.1, the initial low flow channel appears as a series of disconnected pools because for this plot the channel bed terrain surface was derived from Lidar, picking up the water surface rather than the underlying channel thalweg at the time of survey.

To improve accuracy of the scalar 3D numerical volume integration where significant longitudinal curvature of the water surface profile might be anticipated at times, low flow sections were interpolated where necessary using AULOS hydraulic interpolation routines.

Use of the standard channel chainages (distances) supplied with the benchmark could not be continued, as these apparently relate to measurements along the low flow channel, which takes several sharp turns within a more gradually curved floodplain. For modelling purposes, the distance between cross-sections must be measured perpendicular to the cross-sections if accurate volume balances are to be maintained. This distance is significantly less than the surveyed chainage differences where the low flow channel is oblique to the cross-sections, which required to be set up to represent the floodplain to cover high flow events as well as low flows.

As a result, it was necessary to modify the river chainages in the lower half of the pictured area, where the low flow channel was not approximately straight. The standard and revised chainages are given in Table A.1.

Downstream from chainage 4.624 km the chainages are as in the original benchmark dataset. Note this reduces the length of the reach from Border Road to Vintage Reserve (chainage 4.798 km) by 315m to 1.369 km, and the slope between ends accordingly increases.

An overland flow branch leaves the right of the main channel from the node at chainage 4.706 km where there is a low point on the right bank. However after some model experimentation, minimal flow was found over this low point during the highest floods in the period of record, and as no significant overflows had been noticed in the field either, this branch was disabled.

More important was the short stub tributary joining the node at chainage 4.798 km (Vintage Reserve) from the left of the channel. This insertion was required to allow the level boundary condition to be

Table A.1 | Standard chainages *vs* Revised model chainages

Standard Chainage (km)	**Revised chainage (km)**
3.114	3.429
3.233	3.529
3.375	3.645
3.446	3.711
3.503	3.776
3.615	3.886
3.699	3.968
3.841	4.081
4.033	4.174
4.318	4.356
4.357	4.395
4.506	4.511
4.624	4.624

applied at the position of the downstream level recorder. Under the rules applying to external boundary nodes, specification of the level here meant that the discharge hydrograph through this nominal tributary had to be computed as part of the model solution.

A.3 | Accuracy Benchmark Compliance

To establish compliance with the published IAHR Flood Risk Management Committee accuracy benchmark, applicants were required to provide for at least one of the two specified floods (2006 and 2008) the following plotted evidence of successful model results:

1. A match within measurement accuracy between modelled and observed level hydrographs at the upstream and downstream ends of the test reach.
2. A match within measurement accuracy between the model stage/discharge curve at the downstream cross-section and the observed gauging points there. Note the model discharge hydrograph must finally be derived by calibration of the resistance model.
3. A match within hydrological modelling accuracy between the model lateral channel inflow and the runoff hydrograph derived by rainfall/runoff modelling from observed rainfall records. (Note the “lateral channel inflow” is that deduced as the residual hydrograph obtained throughout the flood by adding downstream discharge to rate of change in reach volume, then subtracting the upstream inflow. This upstream inflow is the discharge through the upstream section, again derived from the calibrated resistance model).

This evidence is provided for the *AULOS* validation in both the 2006 and 2008 floods in the following sections.

A.3.1 | Modelled and Observed Level Hydrographs Upstream and Downstream

The match between modelled (x and + markers) and observed (continuous lines) is plotted for the 2006 flood in Figure A.2 and for the 2008 flood in Figure A.3. The upstream (Border Road) results are plotted in red and the downstream (Vintage Reserve) results in blue.

For both floods the upstream results are indistinguishable, simply because the observed level hydrographs were applied directly as the model upstream boundary condition. No attempt at applying an upstream flow hydrograph can be expected to result in a comparable match.

However small departures of the order of a few millimetres can be seen at the downstream boundary, where the model + markers fall below the continuous line, particularly at the beginning of the rising

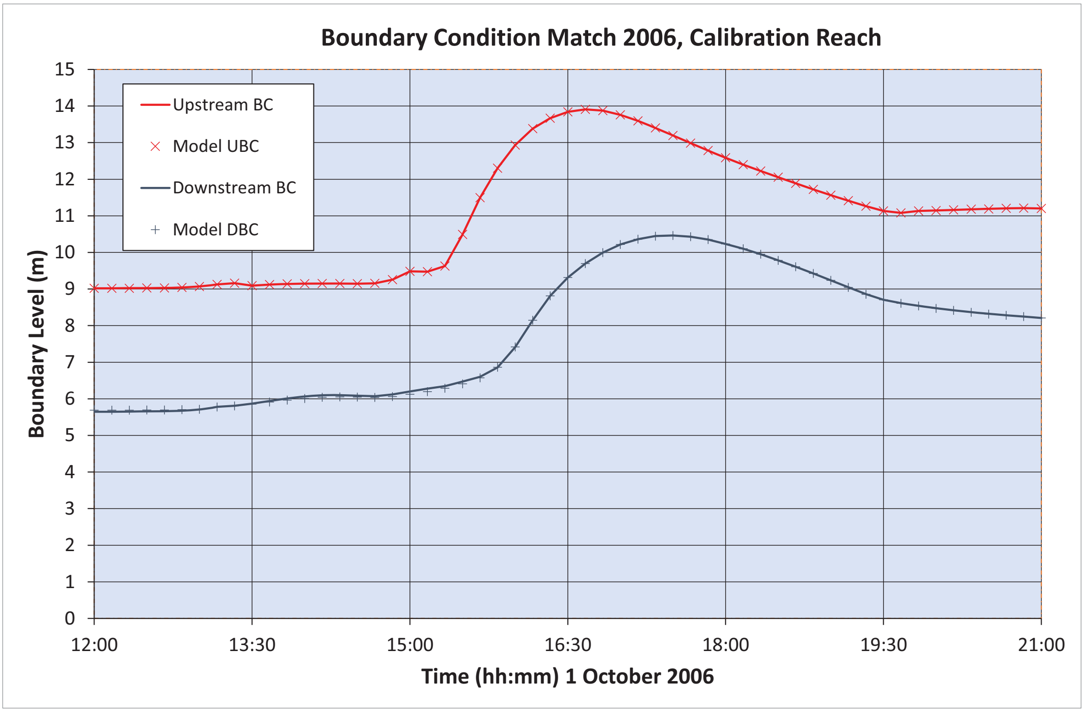

Figure A.2 | Boundary Condition Match for Recorded and Modelled 2006 Flood Level Hydrographs.

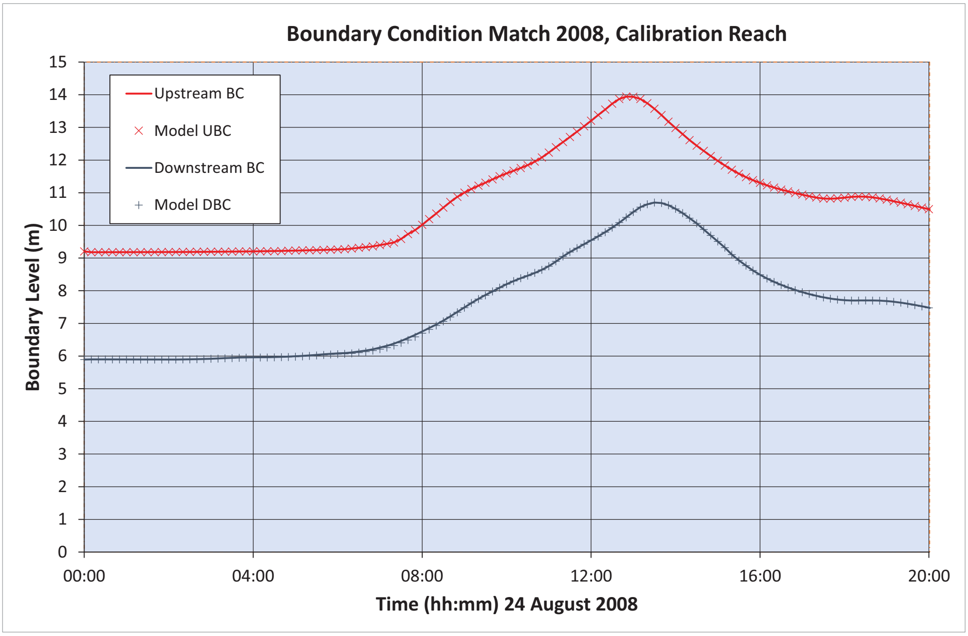

Figure A.3 | Boundary Condition Match for Recorded and Modelled 2008 Flood Level Hydrographs.

flood waves. This is because the observed boundary level hydrograph was applied at the open end of the stub tributary while the model results are plotted on the main channel where the inflow from the stub tributary joins the main flow. The small head loss along this tributary flow could be further reduced by enlarging the cross-section of the nominal tributary, but the match is already considered good enough to satisfy the first compliance criterion.

A.3.2 | Match between Model Stage/Discharge Curve and Observed Gauging Points

The model stage/discharge results are plotted against the observed gauging points in Figure A.4. The gauging points are identified by a range of markers according to date of observation, as indicated in the legend, while the model stage/discharge results are plotted as curves: a continuous green line for the 2006 flood results (Run Opa06Y) and a dotted brown line for the 2008 results (Run Opa08Y).

Note the rising limbs of the floods plot below the falling limbs, giving a loop rating in accordance with standard hydraulic theory, and also consistent with the gauged evidence in which the gaugings on a rising limb (marked with a red + sign) fall generally below and to the right of those measured during steady or falling flows. Only a single rising limb gauging was recorded for floods above the 9 m level,

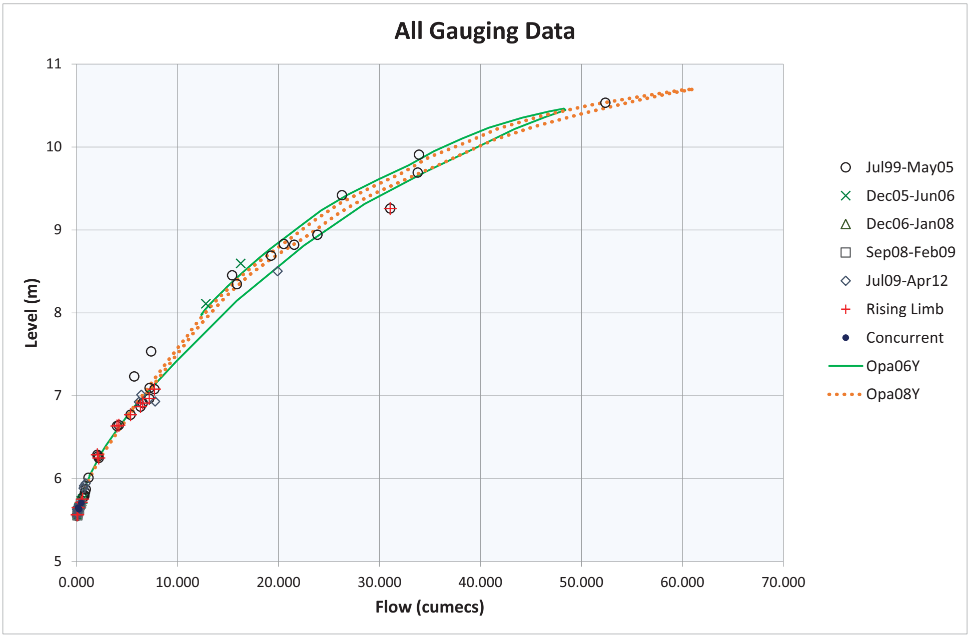

Figure A.4 | Match between Model Stage/Discharge Curves and Observed Gaugings.

and this is below and to the right of all the other results at these higher levels. However it is possible that this gauging coincided with an extremely rapidly rising flood, making the corresponding loop wider than for the 2006 and 2008 floods.

The falling limb curve for the 2006 flood lies slightly above and to the left of that for the 2008 flood. This is caused by the use of a base Manning $n = 0.045$ for the model 2006 flood, while that calibrated for the model 2008 flood was $n = 0.040$. This difference is discussed further in the next section.

A.3.3 | Match between Model Lateral Channel Inflow and Rainfall/Runoff Calculations

The match between the lateral channel inflows deduced by hydraulic and hydrological methods is plotted in Figure A.5 (2006 flood) and Figure A.6 (2008 flood).

The two inflow hydrographs are strictly comparable only to a first order, that is where the total lateral inflows are always significantly smaller than the main stream flow. This is because the hydraulic method computes the difference between flows *arriving* at the gauging station originating from flows entering the upstream end, and flows *leaving* the gauging station which must comply with the observed rating curves. In contrast, rainfall/runoff models estimate inflow hydrographs arriving at

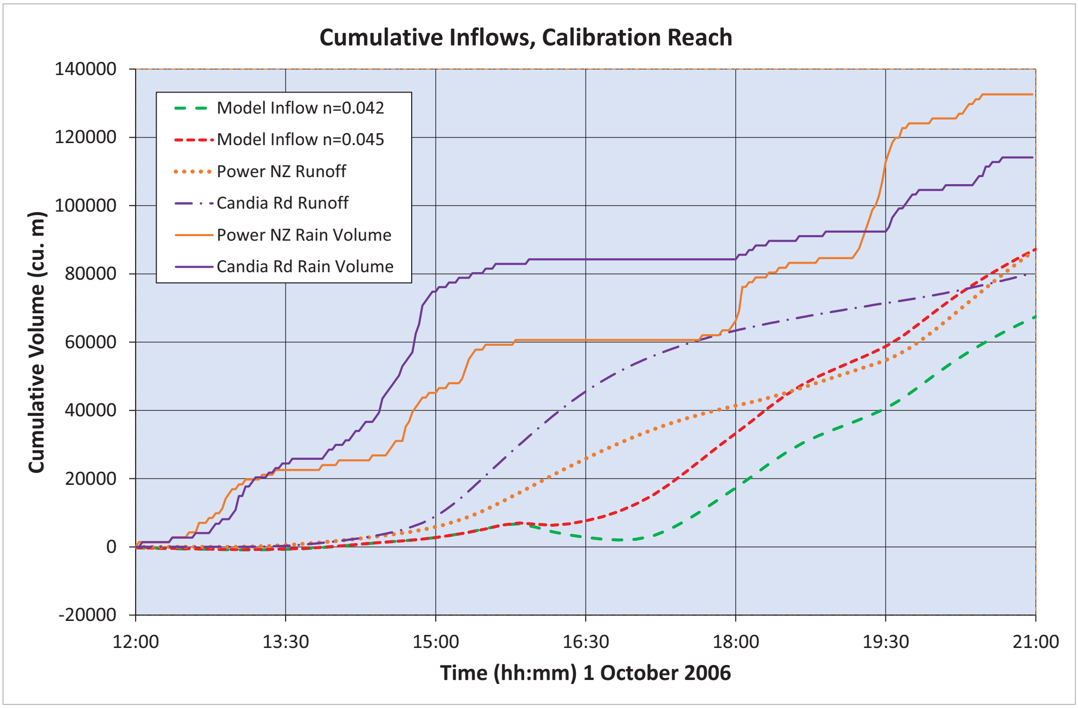

Figure A.5 | Match between Model Lateral Flows and Rainfall/Runoff Calculations: 2006 Flood.

the banks on both sides of the river along the full length of the study reach. Depending on the level of detail attempted, the contributing catchment may be divided into several subcatchments, each of which contributes flows arriving at different places at different times.

Summation of these flows then becomes difficult, because each will have a different transit time from the point of discharge at the river bank to the gauging station where the hydraulic method counts the inflow.

For these reasons the comparison of hydrographs is best made on the basis of cumulative inflow hydrographs as plotted in Figures A.5 and A.6. The cumulative rain volumes, plotted as continuous lines, then indicate the total precipitation on the 271 ha catchment based on the rain gauges at the Power NZ and Candia Road sites identified in the published benchmark documentation. These should provide an upper limit to the expected runoff, together with an indication of the uncertainty associated with the selection of rain gauge records.

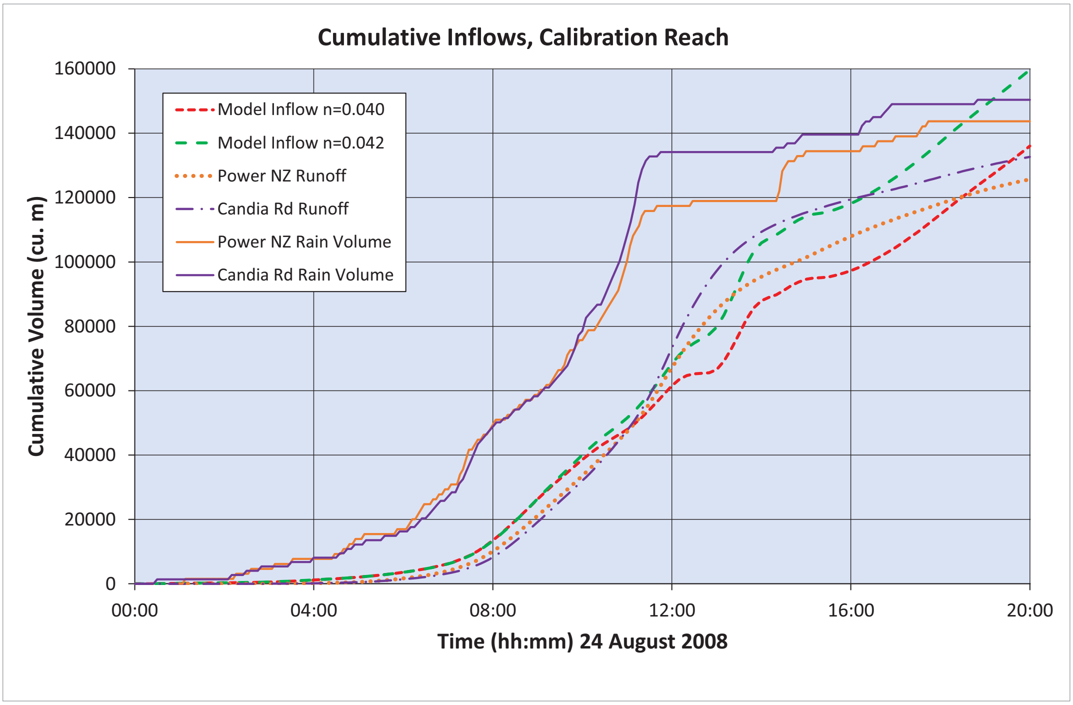

Figure A.6 | Match between Model Lateral Flows and Rainfall/Runoff Calculations: 2008 Flood.

The corresponding rainfall/runoff estimates are plotted as a brown dotted line for the Power NZ site and as a purple chain dotted line for the Candia Road site.

These were computed using the HYCEMOS-U hydrological package, which uses kinematic wave analysis based on a single catchment open book model, incorporating two sloping planes contributing to a central sloping channel. The best fits (shown plotted) were obtained with one plane contributing a fast response and the other contributing a slow response into a relatively short nominal channel.

Two hydraulic model results are shown in each plot, corresponding with a base Manning $n = 0.042$ and $n = 0.045$ in Figure A.5 and with a base Manning $n = 0.040$ and $n = 0.042$ in Figure A.6. In both Figures the curves for $n = 0.042$ are plotted with long green dashes, while the curves for the other Manning n values are plotted with short red dashes. It turns out that the hydraulic inflow predictions are highly sensitive to the choice of base Manning n, as a variation of only 1% in this roughness parameter will produce a significant difference to the lateral inflows produced by the model.

As a result, the best fit for the 2006 flood gave a Manning $n = 0.045$ for the 2006 flood and a Manning $n = 0.040$ for the 2008 flood. A seasonal explanation for this difference can be suggested, as illustrated in Figure A.7.

This photograph was taken on 30 August 2007, less than a year after the 2006 flood and almost exactly a year before the 2008 flood. Vegetation obviously contributes strongly to the resistance to flow as soon as levels exceed the low flow channel, but at the end of winter regrowth has barely commenced. If this corresponds to a Manning $n = 0.040$ as fitted, then it is not difficult to accept that a Manning $n = 0.045$ could be expected after a further month of spring growth.

Therefore a match between model lateral channel inflows and runoff hydrographs derived by rainfall/runoff modelling has been established within hydrological modelling accuracy, taking into account the differences in location of the assumed inflow points.

Figure A.7 | View of Opanuku Stream Upstream from Vintage Reserve Footbridge.

A.3.4 | Note on Downstream Boundary Conditions

The actual model downstream boundary is at the top of Figure A.1, as the model must be continued downstream of the Vintage Reserve gauging station to allow the difference between flows arriving at the gauging station and leaving the gauging station to be computed. As shown in Figure A.4, a good fit was obtained by computing the backwater from a drawdown to an overfall at Chainage 5.000km, near the downstream boundary at Chainage 5.100 km. This overfall effectively disconnected the downstream boundary from the rest of the model, as any arbitrary downstream level can be specified without changing the solution, as long as that level is not high enough to cause drowning of the overfall.

Accordingly an arbitrary downstream boundary level was specified as a constant 4.000 m at Chainage 5.100 km. This is similar to the common laboratory model practice of establishing an overfall into a discharge pit downstream of the area of interest. Considerable variations in discharge pit level then have no effect on model results.

A.4 | Summary

Three compliance criteria were stated for validation of the published IAHR Flood Risk Management Committee accuracy benchmark. All three criteria have been met for both the 2006 and 2008 floods by the *AULOS* hydraulic modelling package developed by HYDRA Software Ltd.

B. Computer Files

Files provided for download as Validation for Accuracy Benchmark A_2 (October 2016):

File Type	Name	Format	Contents
Document	Accuracy Validation A_2	pdf	Report on the validation by *AULOS,* plus working model file structures.
Zipped Folder	Benchmark	zip	
	Hycemos	Subdirectory	ASCII Text files containing input to and output from the HYCEMOS-U rainfall/runoff modelling package.
	Report	Subdirectory	*AULOS* Report (.rpt) files, in particular Opa06Y.rpt for the 2006 flood and Opa08Y.rpt for the 2008 flood. Also miscellaneous ASCII Text auxiliary files used for the preparation of the validation Excel files (see below).
	Validation	Subdirectory	Files used for the preparation of the validation report figures. GaugingValidation.xls provides all the workings for preparation of Figure 4. Opamap.jpg is the basis of Figure 1. ResidualValidation.xls provides all the workings for preparation of Figures 2, 3, 5 and 6.
	AULOS key files	.aky (ASCII Text)	Key (aky) files contain all information necessary to run a model. In particular Opa06Y.aky will run the 2006 flood and Opa08Y.aky will run the 2008 flood.
	AULOS brn files	.brn (ASCII Text)	Branch-Reach-Node (brn) files contain all model data, which may be inspected and edited. In particular, Opa06Y.brn contains the 2006 flood model and Opa08Y.brn contains the 2008 flood model.
	AULOS arw file	.arw (ASCII Text)	AULOS Raw data files stores the raw cross-section database managed by the brn editor. OpanukuW.arw holds several versions of the sections.
	AULOS boundary files	.txt	Boundary Condition databases for the 2006 and 2008 floods.

Bibliography

1 | Abbott, M. B. (1979). Computational Hydraulics. Pitman, 326 pp.

2 | Aoi, S., Asano, Y., Kunugi, T. et al. (2020). MOWLAS: NIED observation network for earthquake, tsunami and volcano. Earth Planets Space 72, 126.

3 | Ball, J. E. (2014). Flood estimation under changing climates, 2014 IAHR-APD Congress, Hanoi, Vietnam.

4 | Ball, J. E., Kerr, A., Rocha, G. C., and Islam, A. (2016). A Review of Stream Gauge Records for Design Flood Estimation, Proceedings 37th Hydrology and Water Resources Symposium, Engineers Australia, Queenstown, NZ.

5 | Ball, J. E., Babister M., Nathan R., Weeks W., Weinmann E., Retallick M., and Testoni I. (2019). Australian Rainfall and Runoff: A Guide to Flood Estimation, Geoscience Australia, Commonwealth of Australia, Canberra, Australia, ISBN 978-192529-7072

6 | Barnett, A. G. (1974). On the stability of centred Implicit difference schemes, Proceedings of the Fifth Australasian Conference on Hydraulics and Fluid Mechanics, Christchurch, II, 537–543.

7 | Barnett, A. G. (1989). Prediction of seiching and tsunamis in Wellington harbour, Consulting report for the Museum of New Zealand/Te Papa Tongarewa by Barnett Consultants Ltd, 109pp.

8 | Barnett, A. G. (2002). Resistance Computation in Compound Channels. Proc. NZWWA 2002 Modelling Conference, Auckland, 143–151.

9 | Barnett A. G. (2010). Computational feasibility of long term continuous simulation Proc. 17th IAHR-APD Congress, Auckland.

10 | Barnett A. G. (2012). Comparison of solution robustness and convergence in coarse grid models, 10th International Conference on Hydroinformatics, Hamburg (on CD).

11 | Barnett, A. G. (2014a). Improved solution reliability through generalized finite integral methods. Journal of Hydroinformatics No. 16(3), 600–616.

12 | Barnett, A. G. (2014b). Corrigendum. Journal of Hydroinformatics No. 16(6), 1464.

13 | Barnett A. G. (2015). 3D Unsteady flow analysis: A return to classical hydraulics. E-Proceedings of the 36th IAHR World Congress, The Hague.

14 | Barnett, A. G. (2017). Dimensionality in direct solutions of real (3D) unsteady flow problems. Proc. 13th Hydraulics in Water Engineering Conference, Sydney.

15 | Barnett, A. G. (2022). Tsunami Flood Risk Management, Civil Engineering for Disaster Risk Reduction, Springer, 101–113.

16 | Barnett, A. G. (2022) Analytical criteria for choosing between vector and scalar 3D flow modelling. E-Proceedings of the 39th IAHR World Congress, Granada.

17 | Barnett, A. G. and MacMurray, H. L (1998). Two comparisons of CELL Integral and finite difference solutions Hydroinformatics 98, Copenhagen, 1, 17–24.

18 | Barnett, A. G., Painter, D. J. and Watkins, S. L. (2004) False pumps in St Venant solutions. Proc. Hydroinformatics 2004, Singapore, 1, 142–149, World Scientific.

19 | Barnett, A. G. and Shamseldin, A. Y. (2008) Resistance computation in overbank flows. 16th IAHR-APD Conference, Nanjing, V, 1829–1834.

20 | Batchelor, G. K. (1967). An Introduction to Fluid Dynamics. Cambridge University Press, 615 pp.

21 | Blom, G. (1958). *Statistical Estimates and Transformed Beta-Variables*, Wiley, New York.

22 | Bresse, J. A.Ch. (1860). *Cours de mécanique appliquée,* 2e partie, Mallet-Bachelier, Paris.

23 | Cabinet Office, Government of Japan (2012). A committee on the great Nankai Trough earthquake model. Available at: https://www. bousai. go. jp/jishin/nankai/model/ (Accessed 1 April 2020) (in Japanese).

24 | Cater, J. E. and Williams, J. J.R. (2008). Large eddy simulation of a long asymmetric compound open channel. Journal of Hydraulic Research, No. 46(4), 445–453.

25 | Chow, V. T. (1959). Open Channel Hydraulics. McGraw Hill, 680pp.

26 | Chow, Ven Te, Maidment, D. R. and Mays, L. W. (1988). *Applied Hydrology*, McGraw-Hill Book Co., ISBN 0-07-010810-2.

27 | Cunge, J. A., Holly, F. M. and Verwey, A. (1980). Practical Aspects of Computational River Hydraulics. Pitman, 420pp.

28 | Cunnane, C. (1978). Unbiased plotting positions - a review, *Journal of Hydrology*, 37:205–222.

29 | De St Venant. (1871). Théorie du mouvement non-permanent des eaux, avec application aux crues des rivières et à l'introduction des marées dans leur lit. (In French). Acad. Sci. Comptes Rendus, 73, 148-154, 237–240.

30 | Dura, T., Garner, A. J., Weiss, R., Kopp, R. E., Engelhart, S., Witter, R. C., Briggs, R. W., Mueller, C. S., Nelson, A. R. and Horton, B. P. (2021). Changing impacts of Alaska-Aleutian subduction zone tsunamis in California under future sea-level rise, Nature Communications, 12, 7119.

31 | England, J. F., Jr., Cohn, T. A., Faber, B. A., Stedinger, J. R., Thomas, W. O., Jr., Veilleux, A. G., Kiang, J. E. and Mason, R. R., Jr. (2018). *Guidelines for determining flood flow frequency—Bulletin 17C* (ver. 1.1, May 2019): U. S. Geological Survey Techniques and Methods, book 4, chap. B5, https://doi. org/10.3133/tm4B5.

32 | Erskine, W. D. and Warner, R. F. (1988). *Geomorphic effects of alternating flood and drought dominated regimes on a NSW coastal river*, in Fluvial Geomorphology of Australia, edited by RF Warner, pp. 223-244, Academic Press, Sydney.

33 | Fukitani, Y,, Moriguchi, S., Tarada, K. and Otake, Y. (2021). Time-Dependent Probabilistic Tsunami Inundation Assessment Using Mode Decomposition to Assess Uncertainty for an Earthquake Scenario, JGR Oceans, 126(7).

34 | Garcia-Navarro, P. and Burguete, J. (2006). Numerical methods for the shallow water equations: 1D approach. River Basin Modelling for Flood Risk Mitigation (D. W. Knight and A. Y. Shamseldin, eds). Taylor and Francis, 607 pp.

35 | Garner, G. G., T. Hermans, R. E. Kopp, A. B. A. Slangen, T. L. Edwards, A. Levermann, S. Nowikci, M. D. Palmer, C. Smith, B. Fox-Kemper, H. T. Hewitt, C. Xiao, G. A∂̃algeirsdoìttir, S. S. Drijfhout, T. L. Edwards, N. R. Golledge, M. Hemer, R. E. Kopp, G. Krinner, A. Mix, D. Notz, S. Nowicki, I. S. Nurhati, L. Ruiz, J-B. Salleìe, Y. Yu, L. Hua, T. Palmer, B. Pearson (2021). IPCC AR6 Sea-Level Rise Projections. Version 20210809. PO. DAAC, CA, USA. (https://podaac. jpl. nasa. gov/announcements/2021-08-09-Sea-level-projections-from-the-IPCC-6th-Assessment-Report).

36 | Gelman, A., Carlin, J. B., Stern, H. S. and Rubin, D. B. (1995). *Bayesian data analysis*, Chapman and Hall, p: 526.

37 | Goldstein, S. (1938). Modern Developments in Fluid Dynamics. Dover (2 Volumes), 702 pp.

38 | Greenberg, E. and MacDonald, A. (2021). Regional Standard for Water Services. Wellington Water, Draft Version 3.0.

39 | Henderson, F. M. (1966). Open Channel Flow. MacMillan, 522 pp.

40 | Hosking, J. R.M. (1990) L-moments: Analysis and estimation of distributions using linear combinations of order statistics, *Journal of Royal Statistics Society*, Series B, 52(2):105–124.

41 | HYDRA Software Ltd (2023) www. auloshydraulics. com.

42 | IPCC (2019). Summary for Policymakers. In: IPCC Special Report on the Ocean and Cryosphere in a Changing Climate [H.-O. Pörtner, D. C. Roberts, V. Masson-Delmotte, P. Zhai, M. Tignor, E. Poloczanska, K. Mintenbeck, A. Alegriìa, M. Nicolai, A. Okem, J. Petzold, B. Rama, N. M. Weyer (eds.)]. in press. Available at: https://www. ipcc. ch/srocc/chapter/summary-for-policymakers/ (Accessed 1 April 2020).

43 | Ippen, A. T. (1966). (Ed.) Estuary and Coastline Hydrodynamics. McGraw-Hill. 744 pp.

44 | JMA (2022). https://www. data. jma. go. jp/gmd/kaiyou/db/tide/sea_lev_var/index_history. php.

45 | Japan Meteorological Agency (JMA) (2013a). Lessons learned from the tsunami disaster caused by the 2011 Great East Japan Earthquake and improvements in JMA's tsunami warning system, Tokyo: JMA. (in Japanese).

46 | Japan Meteorological Agency (JMA) (2013b). Emergency warning system. Available at: http://www. jma. go. jp/jma/en/EmergencyWarning/ewindex. html (Accessed 15 September 2013) (in Japanese).

47 | Koshimura, S. and Shuto, N. (2015). Response to the 2011 Great East Japan Earthquake and Tsunami disaster, Philosophical Transactions of the Royal Society A, 373, 20140373.

48 | Kuczera, G. and Franks, S. (2019). *At-Site Flood Frequency Analysis*, in Australian Rainfall and Runoff: A Guide to Flood Estimation, Ball, JE, Babister M, Nathan R, Weeks W, Weinmann E, Retallick M, and Testoni I, Editors, Geoscience Australia, Commonwealth of Australia, Canberra, Australia, ISBN 978-192529-7072.

49 | Landau, L. D. and Lifshitz, E. M. (1959). Fluid Mechanics, Pergamon, 536 pp.

50 | Langbein, W. B. (1949). Annual floods and the partial-duration flood series, *Transactions, American Geophysical Union*, 30(6), 879–881.

51 | Lee, P. M. (1989). *Bayesian statistics: An introduction*, Oxford University Press (NY).

52 | L. Li, A. D. Switzer, Y. Wang, C.-H. Chan, Q. Qiu, R. Weiss (2018). A modest 0.5-m rise in sea level will double the tsunami hazard in Macau, Science Advances, 4, 1–11.

53 | Macara, G., Wooley J.-M., Zammit C., Pearce P., Stuart S., Wadwha S., Sood A. and Collins D. (2019). *Climate Change Projections for the Otago Region* Prepared for Otago Regional Council, NIWA Client Report No 2019281WN, NIWA Project ORC20102.

54 | Ministry for the Environment (2004). Coastal Hazards and Climate Change. New Zealand Climate Change Office, 145 pp.

55 | Ministry of Land, Infrastructure, Transportation and Tourism (MLIT) (2013). Guidelines for breakwaters designed to survive tsunami, 40 pages Available at: http://www. mlit. go. jp/common/001012142.pdf (Accessed 21 September 2015) (in Japanese).

56 | Milne-Thomson. (1968). Theoretical Hydrodynamics. MacMillan. 743 pp.

57 | Nagai, R., Takabatake, T., Esteban, M., Ishii, H. and Shibayama, T. (2020). Tsunami risk hazard in Tokyo Bay: The challenge of future sea level rise, International Journal of Disaster Risk Reduction, 45, 101321.

58 | Nezu, I. (1994). Compound open-channel turbulence and its role in river environment. Keynote Address, 9th Congress of the APD-IAHR, Singapore, 24 pp.

59 | Ng, Y. Y. (editor, First Edition, 1994). Stormwater Drainage Manual, Planning, Design and Management Fifth Edition, January 2018, Drainage Services Department, Government of the Hong Kong Special Administrative Region, 193 pp. (last accessed 20 November 2022) https://www. dsd. gov. hk/EN/Files/Technical_Manual/technical_manuals/Stormwater_Drainage_Manual_Eurocodes. pdf

60 | Pakoksung, K., Suppasri, A. and Imamura, F. (2018). Systematic evaluation of multilayered infrastructure systems for tsunami disaster mitigation in Sendai City, Geosciences, 8 (5), 173.

61 | Port and Airport Research Institute (PARI) (2011) Great East Japan Earthquake http://www. pari. go. jp/en/eq2011/. (in Japanese).

62 | Rouse, H. and Ince, S. (1963). History of Hydraulics. Dover, 269 pp.

63 | Samuels, P. G. (2006) Risk and uncertainty in flood management. River Basin Modelling for Flood Risk Mitigation (D. W. Knight and A. Y. Shamseldin, eds). Taylor and Francis, 607 pp.

64 | Stedinger, J. R., Vogel, R. M. and Foufoula-Georgiou, E. (1993). *Frequency analysis of extreme events*, in Handbook of Hydrology, Maidment, D. R. (ed.), McGraw-Hill, NY.

65 | Suppasri, A., Koshimura, S., Imai, K., Mas, E., Gokon, H., Muhari, A. and Imamura, F. (2012). Damage characteristic and field survey of the 2011 Great East Japan tsunami in Miyagi prefecture, Coastal Engineering Journal, 54(1), 1250005.

66 | Suppasri, A., Shuto, N., Imamura, F., Koshimura, S., Mas, E. and Yalciner, A. C. (2013). Lessons learned from the 2011 Great East Japan tsunami: Performance of tsunami countermeasures, coastal buildings and tsunami evacuation in Japan, Pure and Applied Geophysics, 170(6–8), 993–1018.

67 | Suppasri, A., Latcharote, P., Bricker, J. D., Leelawat, N., Hayashi, A., Yamashita, K., Makinoshima, F., Roeber, V. and Imamura, F. (2016). Improvement of tsunami countermeasures based on lessons from the 2011 Great East Japan Earthquake and Tsunami -Situation after five years-, Coastal Engineering Journal, 58 (4), 1640011.

68 | Suppasri, A., Maly, L., Kitamura, M., Syamsidik, Pescaroli, G., Alexander, D. and Imamura, F. (2021). Cascading disasters triggered by tsunami hazards: A perspective for critical infrastructure resilience and disaster risk reduction, International Journal of Disaster Risk Reduction, 66, 102597.

69 | Syamsidik, Tursina, Suppasri, A., Musa Al'ala, Mumtaz Luthfi and Comfort, L. K. (2019). Assessing the tsunami mitigation effectiveness of the planned Banda Aceh Outer Ring Road (BORR), Indonesia, Natural Hazards and Earth System Sciences, 19, 299–312.

70 | TOKEN C. E. E. Consultants co., ltd. (2011). Technology topics http://www. tokencon. co. jp/technology/topics/akg7b200000024ca. html. (in Japanese).

71 | Tsushima, H., Hino, R., Ohta, Y. Iinuma, I. and Miura, S. (2014). tFISH/RAPiD: Rapid improvement of nearfield tsunami forecasting based on offshore tsunami data by incorporating onshore GNSS data. Geophysical Research Letters, 41, 3390–3397.

72 | Tursina, Syamsidik, Kato, S., Afifuddin, M. (2021). Coupling sea-level rise with tsunamis: Projected adverse impact of future tsunamis on Banda Aceh city, Indonesia, International Journal of Disaster Risk Reduction, 55, 102084.

73 | Wang, Q. J. (1997). LH moments for statistical analysis of extreme events, *Water Resources Research*, 33(12):2841–2848.

74 | Westra, S., Leonard, M. and Zheng, F. (2019). *Interaction of Coastal and Catchment Flooding*, in Australian Rainfall and Runoff: A Guide to Flood Estimation, Ball, JE, Babister M, Nathan R, Weeks W, Weinmann E, Retallick M, and Testoni I, Editors, Geoscience Australia, Commonwealth of Australia, Canberra, Australia, ISBN 978-192529-7072.

75 | Whitham, G. B. (1955). The effects of hydraulic resistance on the dam-break problem, Proc. Royal Society A, 227, No. 1170, 399–407.

76 | World Meteorological Organisation (2010). *Manual on Stream Gauging*, WMO Report No. 1044, Geneva, Switzerland.

77 | Wormleaton, P. R. and Merrett D. J. (1990). An improved method of calculation for steady uniform flow in prismatic main channel/flood plain sections. *J. Hyd. Res.* 28(2), 157–174.

78 | Yamashita, F. (2008). Tsunami and disaster prevention-Sanriku tsunami, Kokon-Shoin publishing, 158 p, ISBN-13: 978-4772241175 (in Japanese).

List of symbols

Where possible, the following list of symbols is consistent with the usage followed by Henderson in his 1966 textbook “Open Channel Flow”. Readers are referred to the introduction to that seminal work for a discussion of the conventions he used. Henderson adopted the term “cusecs” in preference over the alternative “cfs” for “cubic feet per second”, mainly because it was easier to say, and for the same reason “cumecs” has been adopted here instead of “cubic metres per second”, or even worse “metres to the power three seconds to the power minus one.”

Because the subject matter differs in some areas from that covered by Henderson, occasional variations from the Henderson standard have been necessary. For example, the “prime” (dash) superscript is used here to denote the predicted parameter value at the end of a time period (see Fig. 2.1). As well as being listed here, these exceptions are identified in the text where they are introduced.

A cross-sectional area of flow, Eq. (2.4).

A_1, A_2 area of cross-section upstream, downstream of jump. Eq. (5.7), Eq. (5.11). At upstream, downstream sections Eq. (8.1).

A_i area of the ith subsection in Eq. (5.3).

A_j area of the jth subsection in Eq. (5.5).

A_m mean area through a reach. Eq. (8.2).

a area ratio in Eq. (5.7).

a, b, c standard coefficients of quadratic. Eq. (4.2).

B surface width. Chapter 2, Section 2.3.1.

b transverse surface width measurement from one side of channel. Eq. (5.9).

D diameter of tube, Eq. (2.1).

E the scalar property in energy-momentum conservation. Chapter 2, Section 2.1.4. The energy above the channel bed in Chapter 5, Section 5.4.2.

e defined in Eq. (5.9) to represent variable height of the water surface above datum.

f functional relationship, Eq. (2.1).

Fr_1 Froude Number upstream of jump. Eq. (5.14).

g the acceleration of gravity. Eq. (2.8) and (2.9).

H energy head above datum. Eq. (5.8). Tsunami height in Eq. (7.3), (7.5).

H_0 original tsunami height in Eq. (7.3).

H_1 energy head upstream of jump. Eq. (5.7).

H_2 energy head downstream of jump. Eq. (5.7).

H_f difference in head between one end and the other of a channel reach. Eq. (2.7).

h static head difference between ends of tube. Eq. (2.1). Vertical distance of free surface water level above datum. See Figure 2.2(a). High tide level rise at time t in Eq. (7.1).

h_f difference in water level between one end and the other of a channel reach. Eq. (2.7).

h_0 high tide level rise at time t_0 in Eq. (7.1).

$h_1,\ h_2$ height of water free surface upstream, downstream of jump. Eq. (5.10). At upstream, downstream sections Eq. (8.2), Eq. (8.3).

$h_1,\ h_n$ height of water free surface above datum at sections 1 and n. See Fig. 2.1.

h' value of h associated with time t_2. Also applied to subscripted values. See Fig. 2.1.

I the inertial property in mass conservation: Chapter 2, Section 2.1.4. Working parameter in Eq. (2.15) and Eq. (2.16). Infrastructure design height: Chapter 7, Section 7.1.2. Used in Eq. (7.5).

i Counting parameter for summation Eq, (5.3),

i_d design rainfall intensity as at 1990 (stationary). Eq. (4.2).

i_t fitted rainfall intensity at year t. Eq. (4.2).

J summation limit in Eq. (5.5).

j counting parameter for summation. Eq. (5.5).

K conveyance. Eq. (2.7).

K_c empirical contraction loss coefficient, Eq. (8.3).

K_f simplifying coefficient, approximately constant. Eq. (5.13).

k relative change in discharge in Eq. (4.3). Gradient of semilog interpolation in Eq. (7.1).

$\mathbf{L}$ design life of a proposed Hong Kong project. Chapter 1.

L length of tube. Eq. (2.1). Scalar length of (possibly curvilinear) channel reach. Eq. (2.7). Hydraulic jump length Eq. (5.11).

L_b working parameter in Eq. (2.15).

L_d design life of project as at 1990 (stationary). Eq. (4.1), Eq. (7.4).

$\mathbf{M}$ the vector property in energy-momentum conservation. Chapter 2, Section 2.1.4.

M dimensioned constant in Manning formula, Eq. (2.13).

m hydraulic mean depth (discussion of Eq. (2.2)). gradient parameter for the semilog plot. Eq. (4.4). Coefficient of proportionality Eq. (5.11). Gradient parameter for the semilog plot. Eq. (7.3).

N working parameter in Eq. (2.15) and Eq. (2.16). Summation limit in Eq. (5.3).

N_v validity ratio resistance loss/shock loss. Eq. (5.12).

$\mathbf{n}$ vector normal to a closed control surface (positive outwards). Eq. (2.4).

n subscript for the downstream section. See Figure 2.1, Figure 5.3.

n the “Manning n” roughness of the wetted perimeter. Eq. (2.13), Eq. (5.2).

n_s a local standard value of the Manning n. Introduced for Eq. (5.4).

P wetted perimeter of cross-section. Eq. (2.2). Cumulative probability in Chapters 4 and 7. Eq. (4.1), (7.4).

P_i wetted perimeter of the ith subsection in Eq. (5.3).

P_j wetted perimeter of the jth subsection in Eq. (5.5).

P' wetted perimeter rescaled to incorporate roughness adjustments. Eq. (5.6).

Q discharge. Eq. (2.1).

$Q_1,\ Q_n$ discharge through sections 1 and n. See Fig. 2.1.

Q_2 discharge through section 2. Eq. (8.1).

Q_d design discharge as at 1990. Eq. (4.2).

Q_L lateral discharge See Fig. 2.1.

Q_t 1990 discharge from which Q_d would result from later intensity changes. Eq. (4.2).

Q' value of Q associated with time t_2. Also applied to subscripted values. See Fig. 2.1.

q discharge per metre width. Chapter 2, Section 2.3.1.

R spatial region of integration. Eq. (2.4). The hydraulic radius A/P in Eq. (5.2).

R_1 hydraulic radius upstream of jump. Table 5.4.5.

R_i hydraulic radius of the ith subsection in Eq. (5.3), (5.4), (5.5).

R_N hydraulic radius of the Nth subsection in Eq. (5.2).

Re Reynolds Number. Eq. (2.2).

r corrected ratio of a local value to a standard value of Manning n. Eq. (5.4).

r_i local ratio for the ith subsection to a standard value of Manning n. Eq. (5.4)

S slope.of uniform channel. See Figure 8.2.

S_0 datum slope for uniform flow. Figure 2.2(b). Datum slope of thalweg. See Eq. (2.15).

S_e energy slope. Eq. (2.8).

S_f friction slope. Eq. (2.9), Eq. (5.1).

S_{f1} friction slope upstream of jump. Eq. (5.11).

S_{fu} upstream friction slope. Eq. (2.14).

S_{fd} downstream friction slope. Eq. (2.14).

s streamwise axis for 1D flow, See Figure 2.2(b).

$s_1,\ s_2$ beginning and end of streamwise distance along a reach. Eq. (2.8).

$s_u,\ s_d$ upstream, downstream distances. Eq. (2.14).

T temperature, Chapter 2 only, Eq. (2.1).

T return period of the Hong Kong design event (Chapter 1).

T return period (Chapter 4 and Chapter 7). Eq. (4.5), Eq. (7.3). Non-stationary return period Eq. (7.6).

T_0 original return period in Eq. (7.3).

T_d design return period as at 1990 (stationary). Eq. (4.1), Eq. (7.4).

T_t fitted return period as at year t. Eq. (4.4).

t time, Eq. (2.4).

t_0 initial time in Eq. (7.1).

$t_1,\ t_2$ start, finish of analytical integration. See Fig. 2.1.

U the constant vector velocity of an inertial frame. Eq. (2.3).

u_m mean velocity over a section. See discussion of Eq. (2.2).

v water velocity vector. Eq. (2.4).

V mean velocity, discharge per metre width per metre depth. Chapter 2, Section 2.3.2.

$W_{u,}W_d$ upstream, downstream weights. Eq. (2.14).

X Parameter based on T, as defined in Chapter 1.

X longitudinal axis (horizontal). See Figure 2.2(a).

x horizontal rectilinear distance along a reach. Eq. (2.9), Eq. (8.1).

$x_1,\ x_2$ beginning and end of horizontal distance along a reach. Eq. (2.9).

y vertical depth of 2D flow. See Figure 2.2(a).

Z vertical axis. See Figure 2.2(a).

z vertical distance of channel bed above datum. See Figure 2.2(a).

α Coriolis coefficient. Chapter 5 Section 5.4.2.

ν kinematic viscosity. Eq. (2.2).

ρ mass density of water. Eq. (2.4).

This IAHR Water Monograph is tailored to the needs of hydraulic engineers working on practical flood risk assessment, as well as on related fields, e.g., hydraulic structures or open channel flows. It provides insights into topics related to riverine flooding and coastal risk management. By spanning a wide range of areas, the reader will get familiar with the basic hydraulic principles of floods, their magnitudes, and the non-stationary effects of climate change. This monograph guides the reader also through hydraulic model application by giving an overview of the reliability and robustness of models. Hence, it is also a valuable contribution for experts from fields other than engineering. The eight chapters are independent and contain extensive cited publications for further reading and reflect, as well, the wealth of experience and expertise of their authors.

Stefan Haun
Head of the Hydraulic Laboratory
University of Stuttgart

The new IAHR Water Monograph on Practical Aspects of Floods is a welcome addition to the River Engineering Literature. It is a wonderful digest of information on broad hydraulic principles and strategies for flood modeling with specific applications to coastal areas with tsunamis. The most interesting contributions include flood frequency in the age of non-stationarity, flooding near coastal areas, and several case-studies in Japan. The monograph is deliberately light on the rainfall-runoff relationship for watersheds and on the details of floodwave-propagation algorithms. Engineers and scientists will enjoy this concise and well-presented IAHR Water Monograph.

Pierre Julien
Emeritus Professor of Civil and Environmental Engineering
Colorado State University

ABOUT THE MAIN AUTHOR

Alastair Barnett is a civil engineer with over forty years of experience of computational studies of water flows in proposed or existing engineering projects in twenty countries. As well as undertaking numerical model studies in harbours, hydropower channels, and drainage networks, he has set up many field monitoring programmes for model calibration and verification. He has developed a series of software packages for hydraulic analysis.
Dr Barnett's New Zealand projects include design and commissioning of the 26km Tekapo power canal, control system integration for the eight-dam Waikato River power cascade, harbour development for major ports at Tauranga and Marsden Point, the Auckland CBD stormwater bypass under the Britomart station development, and coastal flooding management for the Te Papa national museum. Internationally he has led coastal infrastructure feasibility reviews for the World Bank, the Asian Development Bank and the European Investment Bank.

ISBN 978-90-834302-3-2
9 789083 430232

IAHR Global Secretariat
iahr@iahr.org

Madrid Office
Paseo Bajo Virgen del Puerto, 3
28005 Madrid, SPAIN
T +34 91 335 7908
F +34 91 335 7935

Beijing Office
A-1 Fuxing Road, Haidian District
100038 Beijing, CHINA
T +86 10 6878 1128
F +86 10 6878 1890

IAHR.org